1991

Three-dimensional Navier-Stokes calculations of a rotor/airframe interaction in forward flight

Laith Abdul Jabbar Zori
Iowa State University

Three–dimensional Navier–Stokes calculations of a rotor/airframe interaction in forward flight

by

Laith A. J. Zori

A Thesis Submitted to the

Graduate Faculty in Partial Fulfillment of the

Requirements for the Degree of

MASTER OF SCIENCE

Department: Aerospace Engineering and Engineering Mechanics
Major: Aerospace Engineering

Iowa State University
Ames, Iowa
1991

TABLE OF CONTENTS

LIST OF TABLES

LIST OF FIGURES

ACKNOWLEDGEMENTS

The author would like to express his deep gratitude and thanks to his major professor Dr. R. G. Rajagopalan, for his guidance and encouragement. Thanks are also due to Sanjay R. Mathur, his invaluable discussions and suggestions contributed immensely to the completion of this thesis. The author would also like to thank C. K. Lim, for his help through all stages of this work, and to K. Kalyanasundaram for proof reading this thesis. Most of all, the author would like to express his gratitude to his parents and family members for their moral support and encouragement.

Local computing support for this thesis was provided by the Iowa State University Computation Center as part of a block grant, and supercomputer time was provided by NASA Ames through a grant under the Numerical Aerodynamic Simulation program. Additional supercomputer time and partial financial support were provided by NASA Langley Research Center through the Subsonic Aerodynamics Branch under grant number: NAG1–1267.

NOMENCLATURE

A	angle defines the pitch orientation of the rotor in the global Cartesian system
a_∞	speed of sound
B	angle defines the lateral orientation of the rotor in the global Cartesian system
C_d	sectional drag coefficient
C_f	skin-friction coefficient
C_l	sectional lift coefficient
C_p	pressure coefficient
c	rotor blade chord
D	Drag force per unit span at a section
$\hat{e}_X, \hat{e}_Y, \hat{e}_Z$	unit vectors in the coordinate system X,Y, and Z, respectively
$\hat{e}_{\mathbf{R}}, \hat{e}_{\mathbf{\Phi}}, \hat{e}_{\mathbf{Z}}$	unit vectors in the coordinate system $\mathbf{R}$,$\mathbf{\Phi}$, and $\mathbf{Z}$, respectively
$\hat{e}_n, \hat{e}_\theta, \hat{e}_s$	unit vectors in the coordinate system n,θ, and s, respectively
$\hat{e}_r, \hat{e}_\theta, \hat{e}_z$	unit vectors in the coordinate

	system r,θ, and z, respectively
$\hat{e}_\xi, \hat{e}_\eta, \hat{e}_\zeta$	unit vectors in the coordinate
	system ξ,η, and ζ, respectively
$\vec{F}$	resultant aerodynamic force on the
	blade, in the (X,Y,Z) system
$\vec{f}$	resultant aerodynamic force on the
	blade, in the (n,θ,s) system
f_n, f_θ, f_s	components of force vector $\vec{f}$
L	Lift force per unit span at a section
M_0, M_1, M_2, M_3	transformation matrices
M'	local Mach number seen by a blade section
N	number of blades
n, θ, s	noninertial coordinate system attached to the blade
p	static pressure
p_{surf}	static pressure on the body surface
p_∞	freestream static pressure
q_∞	freestream dynamic pressure
R	radius of the rotor
R_f	radial distance from the hinge off-set
	to a point on the blade.
$\mathbf{R}, \mathbf{\Phi}, \mathbf{Z}$	cylindrical coordinate system attached to the
	computational domain, where $\mathbf{Z}$ is parallel to
	the freestream
$\vec{r}$	position vector of a point on the blade span

	in the (r,θ,z) system
r, θ, z	rotor based cylindrical–polar system
$S_{\mathbf{R}}, S_{\Phi}, S_{\mathbf{Z}}$	source terms in the momentum equation
s	generalized coordinate in the direction of the blade span
T	general independent variable
$\vec{V}$	absolute velocity of the flow with respect to the
	the computational coordinate system
$\vec{V}_{bl}$	linear velocity of the blade at a given radius
$\vec{V}_{rel}$	flow velocity relative to the blade,
	in the (n, θ, s) system
V_{∞}	freestream velocity
v''_n	component of velocity relative to the blade,
	in the n–direction, includes flapping contribution
V_R, V_{Φ}, V_Z	components of velocity in the cylindrical
	computational domain
v_n, v_θ, v_s	components of absolute velocity $\vec{V}$
	in the (n, θ, s) system
v'_n, v'_θ, v'_s	components of velocity relative to the blade,
	in the (n, θ, s) system
X,Y,Z	inertial Cartesian reference frame,
	where X is parallel to freestream

Greek Symbols

α	blade section angle of attack
$\alpha_{s_{lat}}$	rotor shaft lateral angle of attack, positive if banked to right
$\alpha_{s_{long}}$	rotor shaft longitudinal angle of attack, positive if tilted reward
$\alpha_{TPP_{lat}}$	tip-path plane lateral angle of attack
$\alpha_{TPP_{long}}$	tip-path plane longitudinal angle of attack
β	blade flap angle, positive if blade flaps up
δ	blade deflection out of the rotor plane
ξ,η,ζ	rotor based Cartesian coordinates, with ξ normal to the rotor tip path plane and points in the direction of the inflow
μ	fluid viscosity, also rotor advance ratio where $\mu = V_\infty \cos \alpha_{TPP_{long}} / \omega R$
ρ	fluid density
θ_r	blade collective pitch angle measured at root
$\Delta\theta$	angular distance traversed by a blade in passing through a control volume
ϕ	blade twist angle
ψ	azimuth angle
$\vec{\omega}$	rotational velocity of the rotor

CHAPTER 1. INTRODUCTION

Background

The flowfield of a helicopter is very complex, and provides a stimulus for the development of the most advanced computational techniques in the field of fluid dynamics. This complexity is attributed to the unique aerodynamic features that the rotary–wing exhibits and to the mutual aerodynamic interference of the many components that makeup the helicopter.

A helicopter rotor experiences a radial increase in blade speed, leading to a high concentration of bound circulation towards the tip of the blade. The high concentration of bound circulation results in a vortical wake for hover as seen in Figure 1.1. In forward flight the translatory motion of the rotor, coupled with the radial increase in blade speed, creates a complex spiral vortical wake geometry. Near the rotor, the wake causes a strong blade–vortex interaction. As the wake convects downstream it rolls up to form a system of vortices trailing behind the rotor disc, as shown in Figure 1.2. The modelling of this wake geometry poses a major challenge to any advanced rotor aerodynamic methodology. Furthermore, the blade rotation often causes the blades to operate in an unsteady, transonic and even supersonic conditions near the tip. Also, the higher relative flow velocity encountered by the rotor disc on its advancing side, compared to its retreating side, causes an asymmetric loading

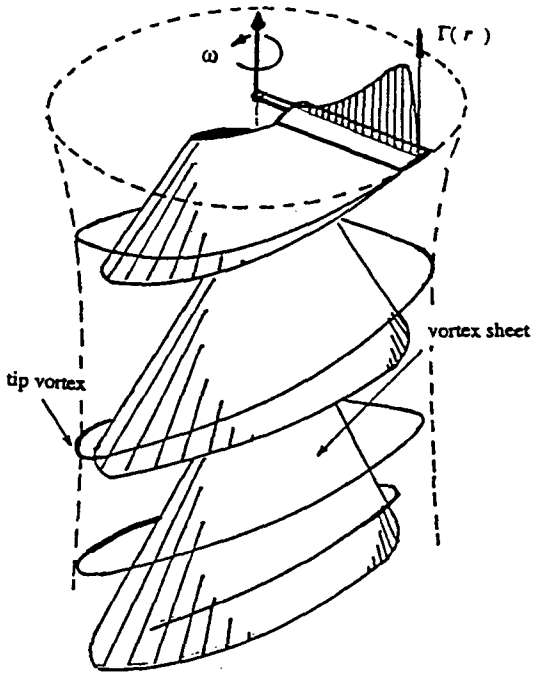

Figure 1.1: Spiral wake geometry

over the rotor disc (Figure 1.3). Cyclic–pitch controls are therefore introduced to redistribute the lift loads more equally over the rotor disc by reducing the angle of attack on the advancing side and increasing it on the retreating side. Helicopters also utilize flapping hinges and thus allow the blade to ride higher or lower during their rotation. On the advancing side the blade moves up - the relative wind moves downward - and the angle of attack is decreased. While on the retreating side, the blade moves down causing an increase in the angle of attack. In addition, the blades operate in the vortical wake of other blades causing a strong blade–wake interaction.

Since the helicopter consists of many components operating in close proximity to each other, complex mutual aerodynamic interference exists between each of the components. To name a few, there is the mutual aerodynamic interference between

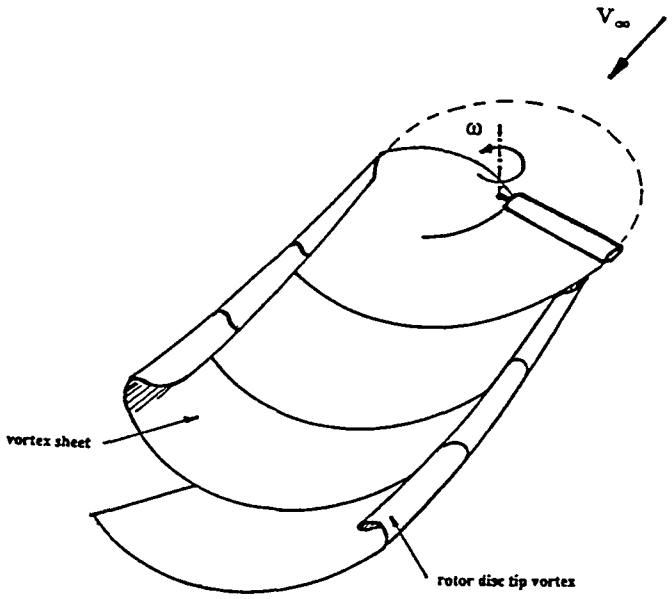

Figure 1.2: Tip vortex shedding

the main rotor and the airframe and between the main rotor and the tail rotor, as well as between the airframe and the tail rotor. The strength of the interaction depends on the relative position and proximity of the individual components, size, shape, type of the wake geometry, and the flight conditions. This highly coupled aerodynamic interaction plays a major role in determining the aerodynamic characteristics and performance of the helicopter. Furthermore, the presence of the airframe displaces the apparent free flow the rotor sees, thereby altering the local angle of attack over the rotor disc. Hence, when rotor performance is to be determined, rotor/airframe interaction must be accounted for.

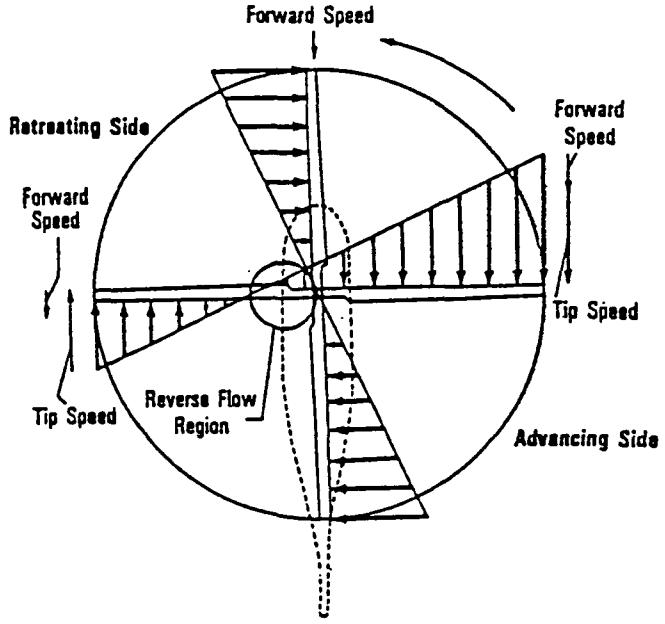

Figure 1.3: Velocity distribution on the rotor in forward flight

Previous Experimental Work

The bulk of the knowledge of helicopter aerodynamics and the measurement of its rotary–wing performance have been accumulated from a number of wind–tunnel and experimental investigations. These investigations targeted various aspects of helicopter aerodynamics and performance (for example: blade vortex interactions, breakup of the tip vortices, blade airloads and rotor–wake/airframe interactions).

Experimental investigations provide an insight and a sense for the most significant effects of interactional aerodynamics. However, obtaining results from experiments are not easy, and are sometimes prohibitively expensive. The work of Betzina et al. [1] has shown the difficulties encountered in determining the effect of airframe on rotor performance. In this work, a wind–tunnel test was conducted to determine

the mutual aerodynamic interaction of a rotor and body for variations in velocity, thrust, rotor/body position, and geometry. Wilby et al. [2] have reported the results of a wind–tunnel investigation of rotor and fuselage shapes representing modern helicopters. They concluded that the fuselage upwash has a significant influence on the blade and hub loads, and this influence must be taken into account while calculating the blade loads. An overview of interactional aerodynamic problems was discussed by Sheridan and Smith [3]. Their work offers a systematic description of the interaction analysis and a recommendation for future research.

Leishman et al. [4–5] in a wind–tunnel investigation tested a small scale rotor and an idealized, but realistic, helicopter body. The results reported indicate that the rotor wake perturbs the mean fuselage loads and the pressure distributions. At a low advance ratios the presence of the fuselage produces moderate increase in rotor thrust, and decrease in power, compared to isolated rotor performance. Brand and Liou et al. [6–12] used laser velocimetery to visualize the details of the rotor wake in forward flight in the presence of a hemispherical–cylinder as an airframe model. The mean and the unsteady pressures were measured on the airframe surface for various flight speeds. The periodic interactions observed on the airframe were attributed to blade passage, tip vortex impingement, and vortex sheet interference. These experimental investigations on simplified helicopter models are essential to our understanding of the aerodynamic interaction problem in addition to providing a much needed data base for the development and validation of analytical techniques.

Previous Analytical Work

Early methods for predicting rotary–wing performance using momentum theory and blade element theory provided an overall picture of the physics of the hovering flight, but did not give detailed information about the flowfield, nor were they able to predict any aerodynamic interactions with other components of the helicopter. It is the rotor–wake influence that plays the major role in helicopter aerodynamics, and the rotor–wake capture is the main challenge in advanced aerodynamic modelling.

The two traditional approaches in helicopter wake modelling are the prescribed wake method and the free–wake method. The common industrial approach for hover flight calculation incorporates a prescribed wake geometry model based on rotor–wake flow visualization. This method has been extended to solve rotor performance in forward flight by several researchers. Lorber and Egolf [13] developed an unsteady aerodynamic interaction code that combined a lifting-line/prescribed-rotor-wake analysis and a source panel fuselage analysis. Though they were able to compute the flow solution over different fuselage geometries for several advance ratios with qualitative success, there were a few inherent deficiencies in the method. The prescribed–wake methods are restricted by the availability of experimental data, such as flow visualization of wake/fuselage interactions. Also, when the rotor–wake/fuselage interference is strong this approach may not correctly model the wake filament break down and its viscous interaction with the fuselage.

A more sophisticated modelling of the wake is achieved by the free–wake method, which allows the wake structure to evolve iteratively by imposing the force free condition on the position of vortices. This method does not depend on experimental data and can be applied to a wide range of configurations and flight conditions. Mavris

et al. [14] successfully extended and coupled the lifting-line/free-wake rotor analysis and source/doublet fuselage analysis, to predict the unsteady aerodynamic interactions between a rotor and an airframe in low speed forward flight. The two methods mentioned above continue to form the industry standard. However, the assumption of potential flow adds restrictions and limitations on the location of vortices – only discrete embedded filaments are allowed. Therefore, many features of the flowfield, such as the size of the tip vortex core, can not be captured. New methods based on Euler equations provide a better modelling of vorticity transport, but the omission of viscosity permits no built–in mechanism for the creation and diffusion of the vortex laden wake, which is very important for rotor/airframe interactional study.

A useful aerodynamic theory must account for the effects of viscosity and must be able to capture the complex vortical flow surrounding the rotor and the airframe. The Navier–Stokes simulation is a step in the right direction if a complete solution of the rotor/airframe interaction is desired. However, the use of the Navier–Stokes methods have been limited primarily by the requirement of large computer memory and computational expense.

In principle, we should be able to completely solve the flowfield around the rotor/airframe by extending the grid from the surface of the blades and the airframe to the outer regions of the wake. However, this is not feasible due to the very high grid density required over a large portion of the domain. In future, with more computer memory becoming available, these methods may be reasonable to use, but for the present they are certainly not economical. These inadequacies restrict the Navier–Stokes simulations to be concentrated in the immediate vicinity of the rotor blade, forcing rotor/airframe viscous simulation beyond the present capabilities

[15–16]. The current method on the other hand, attempts to circumvent the above inadequacies by modelling the rotor in a viscous flowfield. An introduction to this modelling procedure follows.

Present Research

The treatment of the rotor is based on a procedure developed by Rajagopalan [17] in which the action of the rotor is modelled through the source terms of the momentum equations at the points through which the blades pass. The magnitude of the sources are determined from the rotor geometry, blade cross–sectional aerodynamic characteristics, and the local flow properties through implicit functional relations. In doing so, the details of the chordwise flow over the rotor blade are not resolved. On the other hand, the present method makes no assumptions about the wake structure, requires no body–fitted rotational grid for the rotor blades, and opens up the possibility of a complete helicopter flowfield computation. The viscous flowfield surrounding the rotor is presently without any compromise is modelled by the steady, laminar, incompressible, 3–D Navier–Stokes equations.

The current work is a part of an on going research in rotor flow computations at Iowa State University [18–21]. The aim of the present study is to develop a computational procedure that will:

1. Demonstrate the capabilities of the present approach in predicting rotor blade loads and performance for a wide range of advance ratios.

2. Predict the aerodynamic interactions between rotor and airframe in forward flights, as well as other more complex interactional problems, such as rotor–

airframe–tail interference.

3. Compute accurate viscous flow characteristics on the main body of the helicopter.

To test the applicability of the rotor modelling procedure for interactional aerodynamics a simplified problem of the main rotor/body flow is solved for in this investigation. In order to achieve the above mentioned objectives, a simplified geometry representing an idealized rotor/airframe is chosen. The results obtained from the current code are compared to experimental results as well as to other theoretical predictions. The idealized rotor/airframe model used in this study (shown in Figure 1.4) has been extensively investigated at Georgia Institute of Technology [6–12]. The details of the model configuration and dimensions are described in Chapter 4. An organizational sequence of the thesis is presented next.

In Chapter 2 the theoretical formulations and the SIMPLER algorithm are reviewed. In Chapter 3 the rotor modelling and the momentum sources due to the rotor influence are explained. The code validation and the results obtained for the rotor/airframe problem are presented and compared with experimental results in Chapter 4. Chapter 5 discusses the conclusions arrived through the course of this study. And finally, this thesis includes an Appendix that contains most of the theoretical derivations needed.

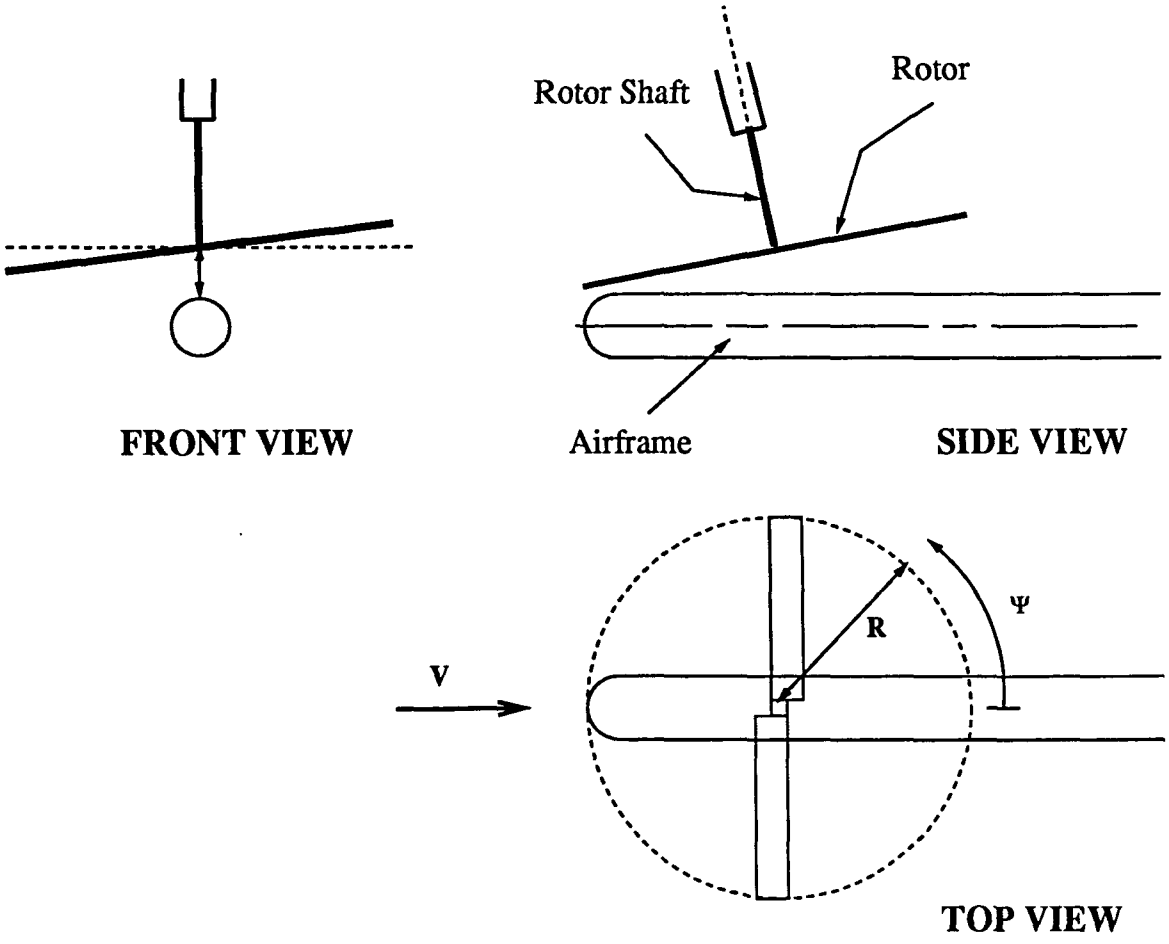

Figure 1.4: Georgia Tech. airframe/rotor model

CHAPTER 2. THEORETICAL FORMULATION AND SOLUTION PROCEDURE

The helicopter rotor is a propulsive device that adds energy into the flowfield, which is felt by the flow as a change in its vector momentum. Therefore, one can account for this change in momentum, while solving the governing fluid equations, by properly modelling the rotor influence at discrete points in the computational domain, through which the rotor blade passes. This leaves us with two tasks: the first is the development of implicit relations for the evaluation of rotor blade source terms; the second is solving the flowfield of the rotor. The procedure for the latter task is described in this chapter, while the rotor modelling will be presented in the next chapter.

Governing Equations

The flowfield of the rotor and body in the present analysis is modelled by the steady, laminar, incompressible Navier-Stokes equations in the cylindrical coordinate system ($\mathbf{R}$,$\mathbf{\Phi}$,$\mathbf{Z}$). The governing equations of the flow are as follows:

continuity equation:

$$\frac{1}{\mathbf{R}}\left[\frac{\partial}{\partial \mathbf{R}}\left(\mathbf{R}\,\rho V_R\right)+\frac{\partial}{\partial \mathbf{\Phi}}\left(\rho V_\Phi\right)+\frac{\partial}{\partial \mathbf{Z}}\left(\mathbf{R}\,\rho V_Z\right)\right]=0 \tag{2.1}$$

R momentum equation:

$$\begin{aligned}\frac{1}{\mathbf{R}}\left[\frac{\partial}{\partial \mathbf{R}}\left(\mathbf{R}\,\rho {V_R}^2-\mu\mathbf{R}\frac{\partial V_R}{\partial \mathbf{R}}\right)+\frac{\partial}{\partial \mathbf{\Phi}}\left(\rho V_\Phi V_R-\frac{\mu}{\mathbf{R}}\frac{\partial V_R}{\partial \mathbf{\Phi}}\right)\right.\\ \left.+\frac{\partial}{\partial \mathbf{Z}}\left(\mathbf{R}\,\rho V_Z V_R-\mu\mathbf{R}\frac{\partial V_R}{\partial \mathbf{Z}}\right)\right]=\\ -\frac{\partial p}{\partial \mathbf{R}}+\frac{\rho {V_\Phi}^2}{\mathbf{R}}-\frac{2\mu}{\mathbf{R}^2}\frac{\partial V_\Phi}{\partial \mathbf{\Phi}}-\frac{\mu V_R}{\mathbf{R}^2}+S_{\mathbf{R}}\end{aligned} \tag{2.2}$$

Φ momentum equation:

$$\begin{aligned}\frac{1}{\mathbf{R}}\left[\frac{\partial}{\partial \mathbf{R}}\left(\mathbf{R}\,\rho V_R V_\Phi-\mu\mathbf{R}\frac{\partial V_\Phi}{\partial \mathbf{R}}\right)+\frac{\partial}{\partial \mathbf{\Phi}}\left(\rho {V_\Phi}^2-\frac{\mu}{\mathbf{R}}\frac{\partial V_\Phi}{\partial \mathbf{\Phi}}\right)\right.\\ \left.+\frac{\partial}{\partial \mathbf{Z}}\left(\mathbf{R}\,\rho V_Z V_\Phi-\mu\mathbf{R}\frac{\partial V_\Phi}{\partial \mathbf{Z}}\right)\right]=\\ -\frac{1}{\mathbf{R}}\frac{\partial p}{\partial \mathbf{\Phi}}-\frac{\rho V_R V_\Phi}{\mathbf{R}}+\frac{2\mu}{\mathbf{R}^2}\frac{\partial V_R}{\partial \mathbf{\Phi}}-\frac{\mu V_\Phi}{\mathbf{R}^2}+S_{\mathbf{\Phi}}\end{aligned} \tag{2.3}$$

Z momentum equation:

$$\begin{aligned}\frac{1}{\mathbf{R}}\left[\frac{\partial}{\partial \mathbf{R}}\left(\mathbf{R}\,\rho V_R V_Z-\mu\mathbf{R}\frac{\partial V_Z}{\partial \mathbf{R}}\right)+\frac{\partial}{\partial \mathbf{\Phi}}\left(\rho V_\Phi V_Z-\frac{\mu}{\mathbf{R}}\frac{\partial V_Z}{\partial \mathbf{\Phi}}\right)\right.\\ \left.+\frac{\partial}{\partial \mathbf{Z}}\left(\mathbf{R}\,\rho {V_Z}^2-\mu\mathbf{R}\frac{\partial V_Z}{\partial \mathbf{Z}}\right)\right]=\\ -\frac{\partial p}{\partial \mathbf{Z}}+S_{\mathbf{Z}}\end{aligned} \tag{2.4}$$

where $S_{\mathbf{R}}$, $S_{\mathbf{\Phi}}$ and $S_{\mathbf{Z}}$ are the rotor source terms through which the rotor's influence is introduced into the surrounding flowfield. A detailed derivation of the above conservation form of the flowfield equations from the vector divergence form is presented in Appendix A.

Solution Procedure

Flow Solver

The conservation equations are solved using SIMPLER – a finite-volume approach developed by Patankar [22]. In this method the flowfield is determined by solving the primitive variables p, V_R, V_Φ, V_Z. This method was chosen for its desirable quality of yielding physically realistic solution even with the use of a coarse grid. The SIMPLER algorithm is very well documented in Reference [22] and hence, only highlights and important principles in this algorithm with special attention given to the integration and discretization of the cylindrical coordinate source terms are presented in the rest of this chapter.

The source terms, defined here as any term in the governing equation that can not be included in the diffusion or convection terms, e.g. pressure forces. Two other types of source terms are discussed in this thesis. The first type are those source terms that arise due to the use of the cylindrical coordinates. The next type are those that are introduced into the governing equations to account for the rotor blades influence on the flowfield.

Grid System

The number of grid points usually determine the size and the cost of the computations. Therefore, it is necessary to choose a coordinate system that will best achieve the desired solution at a low cost. The choice of the coordinate system in the present work is dictated by the geometry of the model we have intend to investigate. The cylindrical coordinate system is used to fit a large portion of the solid body

surface that represents the airframe model (Figure 1.4).

The calculation domain is divided into a number of non-overlapping control volumes, and the grid points are placed at the center of these control volumes. Scalar variables such as pressure, density and viscosity are associated with these grid points. The velocity components on the other hand, are calculated for points that lie on the faces of the control volumes (Figure 2.1). These displaced grids for the velocity components are called the staggered grids (Figure 2.2.a–2.2.c).

Discretization of the Generic Governing Equation

Our aim in this section is to write a discretized equation based on the generic governing equation for a general dependent variable T that can be convected and diffused. The formulation for discretizing the generic governing equation will be used as basis for discretizing the governing flowfield equations.

The computational domain is divided into several non-overlapping control volumes as shown in Figure 2.1; and the grid points associated with the scalar variables: density, viscosity, pressure and the dependent variable T are located at the center of the control volumes while the velocity components are located at the control volume faces.

The steady governing equation for a general variable T in the divergence form is given by

$$\left(\nabla \bullet \rho \vec{V}\, T\right) = \nabla \bullet (\mu \nabla T) + S \tag{2.5}$$

where ρ is the density, μ is the viscosity, $\vec{V}$ is the velocity vector and S is the source term. The term on the left hand side of the above equation represents the convection of T, while the first term on the right side represents the diffusion of T.

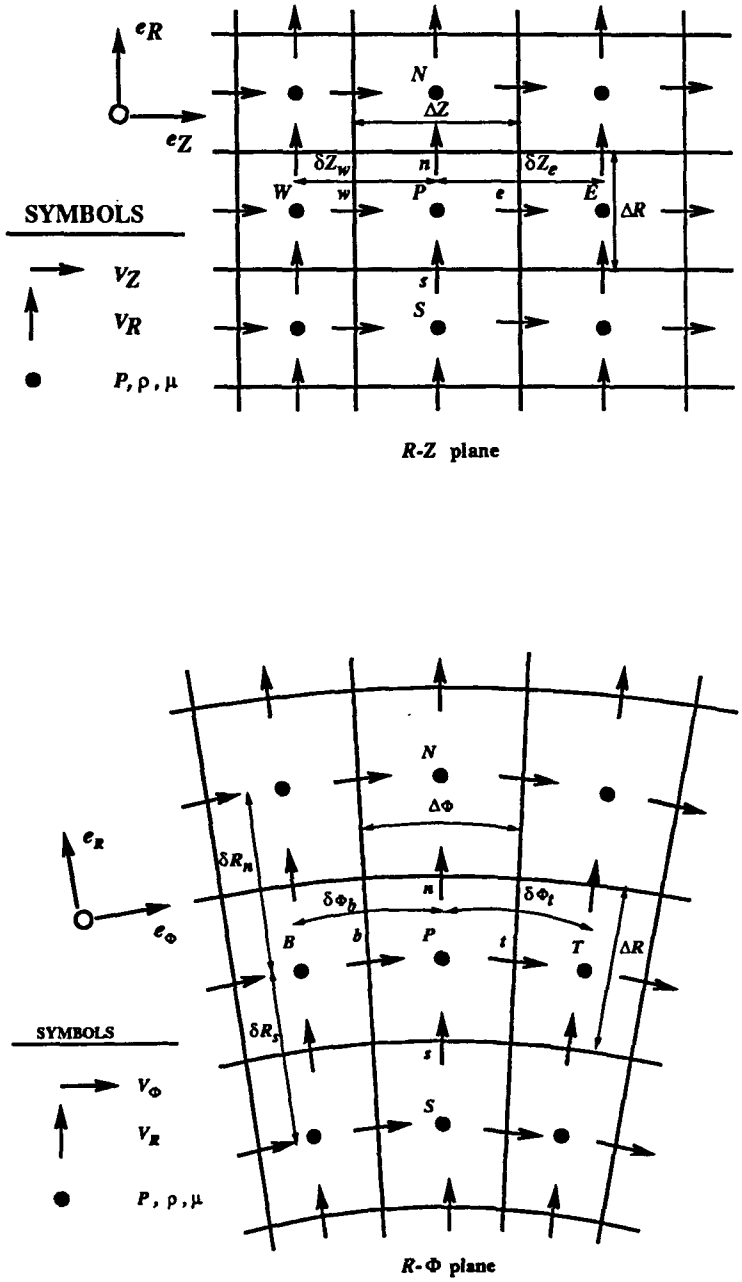

Figure 2.1: The staggered grid

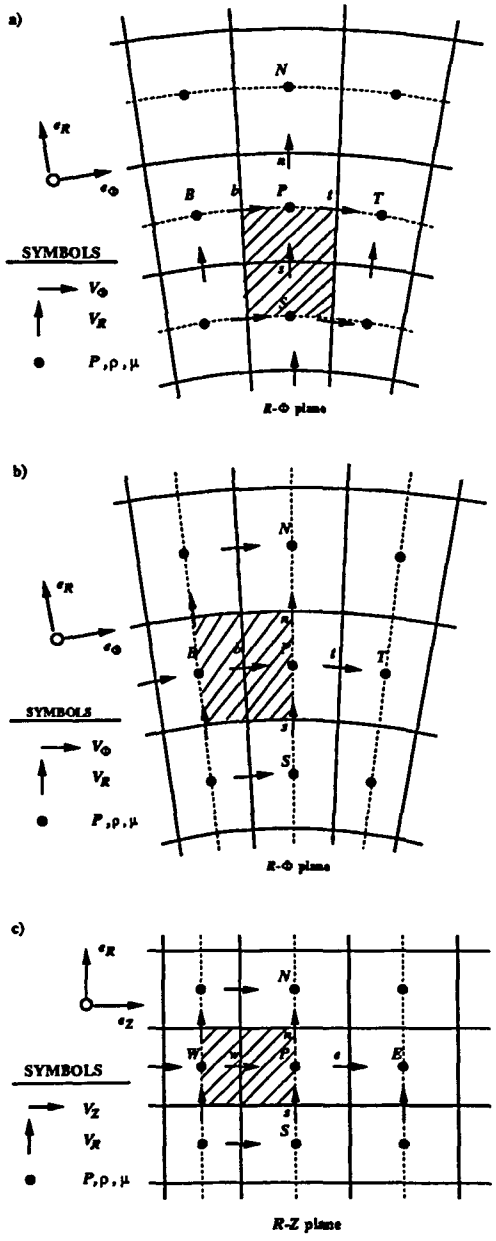

Figure 2.2: a. V_R grid cell b. V_Φ grid cell c. V_Z grid cell

Expanding Equation 2.5 using divergence and gradient operations in the cylindrical coordinate system and then regrouping terms, the following conservation form of the equation results:

$$\frac{1}{\mathbf{R}}\left[\frac{\partial}{\partial \mathbf{R}}\left(\mathbf{R}\,\rho V_R\,T-\mu\mathbf{R}\frac{\partial T}{\partial \mathbf{R}}\right)+\frac{\partial}{\partial \Phi}\left(\rho V_\Phi\,T-\frac{\mu}{\mathbf{R}}\frac{\partial T}{\partial \Phi}\right)\right.$$
$$\left.+\frac{\partial}{\partial \mathbf{Z}}\left(\mathbf{R}\,\rho V_Z\,T-\mu\mathbf{R}\frac{\partial T}{\partial \mathbf{Z}}\right)\right]=S \tag{2.6}$$

Integrating the above equation for any control volume, yields the following discretized equation:

$$\begin{aligned} a_P T_P &= a_E T_E + a_W T_W + a_N T_N + a_S T_S + a_T T_T + a_B T_B + b \\ &= \sum a_{nb} T_{nb} + b \end{aligned} \tag{2.7}$$

where E, W, N, S, T, and B refer to east, west, north, south, top, and bottom grid points respectively; nb refers to the points neighboring the point P. The discretization of Equation 2.6 and the corresponding notation follow Reference [22] closely, where more details can be found. The coefficients a_E, a_W, ... a_B, in Equation 2.7 contain the convection and the diffusion terms and are given by the following relations:

$$\begin{aligned} a_E &= D_e A(|P_e|) + [\![-F_e, 0]\!] \\ a_W &= D_w A(|P_w|) + [\![F_w, 0]\!] \\ a_N &= D_n A(|P_n|) + [\![-F_n, 0]\!] \\ a_S &= D_s A(|P_s|) + [\![F_s, 0]\!] \\ a_T &= D_t A(|P_t|) + [\![-F_t, 0]\!] \\ a_B &= D_b A(|P_b|) + [\![F_b, 0]\!] \\ a_P &= a_E + a_W + a_N + a_S + a_T + a_B - S\Delta V \end{aligned} \tag{2.8}$$

where P_e, P_w,... P_b are the Peclet numbers, which are the ratio of F (the flow rate across the surface of the control volume) and D (the diffusion across the surface of the control volume). The symbol $[\![\ ]\!]$ denotes the greater of the quantities within; b is the discretized source term, while $S\Delta V$ comes from the linearization of the source term.

The power-law scheme was selected for the function $A(|P|)$, which is given by

$$A(|P|) = [\![0, (1 - 0.1\,|P|)^5]\!] \tag{2.9}$$

The above function is a curve fit of the exact solution of the steady one-dimensional convection/diffusion problem of the general dependent variable T. The variation of T is dependent on the convection (F) and diffusion (D) given by:

$$\begin{aligned}
F_e &= (\rho V_Z)_e\,(\mathbf{R}\,\Delta\Phi\,\Delta\mathbf{R})_e & D_e &= \frac{\mu_e}{\delta \mathbf{Z}_e}(\mathbf{R}\,\Delta\Phi\,\Delta\mathbf{R})_e \\
F_w &= (\rho V_Z)_w\,(\mathbf{R}\,\Delta\Phi\,\Delta\mathbf{R})_w & D_w &= \frac{\mu_w}{\delta \mathbf{Z}_w}(\mathbf{R}\,\Delta\Phi\,\Delta\mathbf{R})_w \\
F_n &= (\rho V_R)_n\,(\mathbf{R}\,\Delta\Phi\,\Delta\mathbf{Z})_n & D_n &= \frac{\mu_n}{\delta \mathbf{R}_n}(\mathbf{R}\,\Delta\Phi\,\Delta\mathbf{Z})_n \\
F_s &= (\rho V_R)_s\,(\mathbf{R}\,\Delta\Phi\,\Delta\mathbf{Z})_s & D_s &= \frac{\mu_s}{\delta \mathbf{R}_s}(\mathbf{R}\,\Delta\Phi\,\Delta\mathbf{Z})_s \\
F_t &= (\rho V_\Phi)_t\,(\Delta\mathbf{R}\,\Delta\mathbf{Z})_t & D_t &= \frac{\mu_t}{\delta \Phi_t}(\Delta\mathbf{R}\,\Delta\mathbf{Z})_t \\
F_b &= (\rho V_\Phi)_b\,(\Delta\mathbf{R}\,\Delta\mathbf{Z})_b & D_b &= \frac{\mu_b}{\delta \Phi_b}(\Delta\mathbf{R}\,\Delta\mathbf{Z})_b
\end{aligned} \tag{2.10}$$

where the suffixes e, w, n, s, t and b refer to control volume interfaces, and $\delta\mathbf{R}$, $\delta\Phi$, $\delta\mathbf{Z}$ are the distances between grid points as illustrated in Figure 2.1. The value of diffusion pertaining to control volume interfaces are determined through the use of harmonic means, while the densities at the interfaces are computed by arithmetic means.

Momentum Equation

By employing the formulation for discretizing the general differential equation, the discretized **R**–momentum equation on a staggered grid shown in Figure 2.2.a can be written as:

$$a_n V_{Rn} = \sum a_{nb} V_{Rnb} + b_{\mathbf{R}} + (p_P - p_N) A_n \tag{2.11}$$

where the neighboring coefficients a_{nb} account for the combined convection–diffusion influence at the control volume faces, $b_{\mathbf{R}}$ represents the discretized source term, the term $p_P - p_N$ is the pressure gradient acting on the control volume, and A_n is the area on which the pressure acts. The coefficients of the momentum equation $(a_e, a_w, ...a_b)$ being functions of the velocity components, make the momentum equation non-linear. This non-linearity is handled by adopting an iterative strategy and by lagging the coefficients.

The **Φ**–momentum equation and the **Z**–momentum equation can also be discretized on the staggered grids shown in Figures 2.2.b and 2.2.c respectively to yield the following:

$$a_t V_{\Phi t} = \sum a_{nb} V_{\Phi nb} + b_{\Phi} + (p_P - p_T) A_t \tag{2.12}$$

$$a_e V_{Ze} = \sum a_{nb} V_{Znb} + b_{\mathbf{Z}} + (p_P - p_E) A_e \tag{2.13}$$

The discretized momentum equations can be solved iteratively if the pressure field is known. If a correct pressure field is employed the resulting velocity field will satisfy the continuity equation. However, the pressure field is unknown and an equation for pressure must be derived to solve for the pressure field.

Pressure Equation and Pressure–Correction Equation

Since the main driving force for the velocity from one cell to the next cell is the pressure difference between the two cells, an accurate solution of the pressure field is important. By manipulating the continuity equation and the momentum equation an equation for pressure is derived and discretized to yield a form similar to Equation 2.7,

$$a_P p_P = a_E p_E + a_W p_W + a_N p_N + a_S p_S + a_T p_T + a_B p_B + bp \qquad (2.14)$$

If a correct velocity field is used in the above equation the correct pressure field will result. However, for a guessed velocity field a pressure–correction equation is required to correct the velocity field obtained from solving the momentum equation. Once more, the pressure–correction equation is derived by manipulating the continuity and the momentum equations, and it is cast in a form similar to Equation 2.7. Thus, the purpose of the pressure–correction equation is to improve the pressure field such that the velocity field will be corrected every iteration and progressively get closer to satisfying the continuity equation.

Momentum Equation Source Terms

The right hand side of Equations 2.2– 2.4 are the source terms of the momentum equations. These source terms are of three types:

1. Source terms included in the momentum equations due to the pressure force acting on a control volume.

2. Source terms arising due to the use of cylindrical coordinate system.

3. Source terms introduced in the momentum equations due to the rotor's influence on the flowfield.

The integration, discretization and linearization of the first two types are described in Appendix A, while the development of the third type is presented in Chapter 3.

The important thing to note about the source terms is that they are often a function of a dependent variable (e.g. velocity) and are therefore non-linear. However, we can deal only with linear dependency since the discretized flow equations are solved by the technique of linear algebraic equations. Therefore, as shown in Appendix A source terms that are independent of velocity are integrated over the control volume and included in the source terms b_R, b_Φ or b_Z of the momentum equations (see Equations 2.11–2.13). On the other hand, source terms that are dependent on the velocity are linearized and integrated as explained in Reference [22].

Boundary Conditions

The differential equations (2.1–2.4) along with the specification of the boundary conditions give a complete mathematical description of the flowfield. The three components of velocity V_R, V_Φ and V_Z are set to the freestream value at the in-flow boundary and at the boundaries that are parallel to the freestream. The normal velocity component on the out-flow boundary, on the other hand, is determined from the conservation of mass, while the other components of velocity are determined by extrapolation. This treatment of the boundaries gives reasonable results if the boundaries are positioned far away from any recirculating regions.

At the end of each iteration, the primitive variables p, V_R, V_Φ and V_Z at the periodic boundary in the Φ–direction (Figure 2.3) are updated such that,

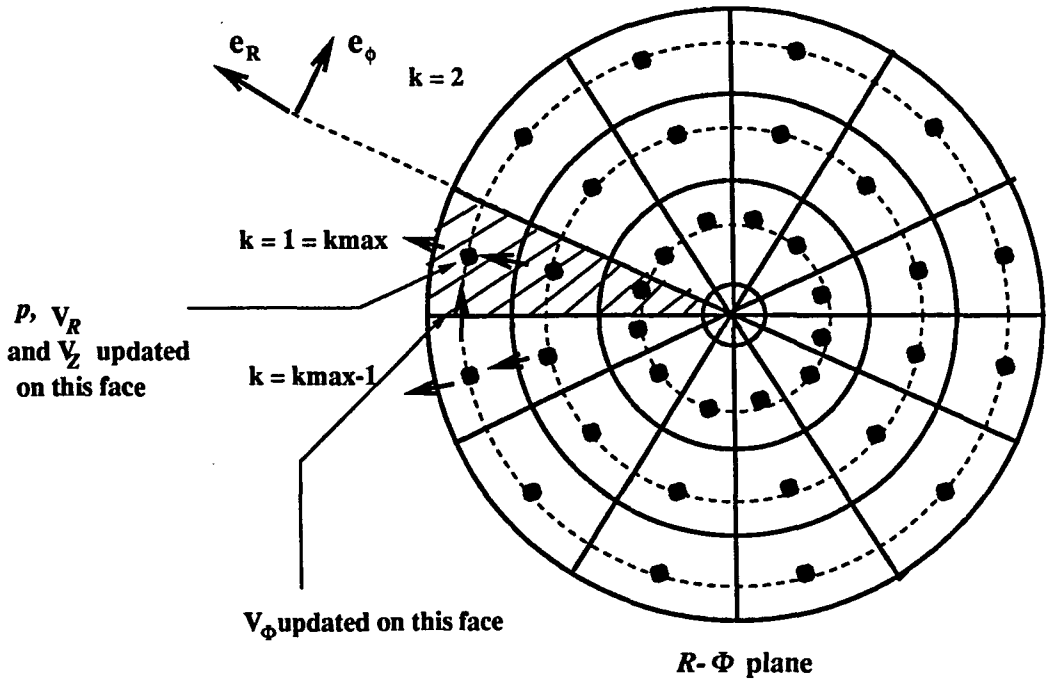

Figure 2.3: Periodic boundary in the cylindrical grid

$$p_{i,j,1} = p_{i,j,kmax}$$

$$V_{\mathrm{R}i,j,1} = V_{\mathrm{R}i,j,kmax}$$

$$V_{\Phi i,j,1} = V_{\Phi i,j,kmax}$$

$$V_{\mathrm{Z}i,j,1} = V_{\mathrm{Z}i,j,kmax}$$

Finally, the solid boundaries of the airframe model are treated by blocking-off the control volumes that lie within the solid region, wherein, the velocity components are set to zero and the viscosity are set to a very large value for these inactive zones. The difficulties arising from the curved nose of the airframe model are overcome by packing more grid points where necessary to resolve this region.

Solving the Discretized Equations

Since the governing equations are non-linear, an iterative procedure must be utilized to obtain the solution. In addition, the non-linear governing equations are cast into a linear form, so that the technique for solving algebraic linear equation can be used. The pressure equation, the three momentum equations and the pressure–correction equation are solved sequentially by using Successive Line Over-Relaxation method (SLOR). TriDiagonal–Matrix Algorithm (TDMA) is used in the non–periodic **R** and **Z** directions and a Cyclic TriDiagonal–Matrix Algorithm (CTDMA) is employed for the periodic **Φ**–direction.

The SLOR method proceeds by sweeping the three dimensional computational space, plane by plane, in all three directions **R**, **Φ** and **Z**. For each plane a sequence of row sweeps followed by a sequence of column sweeps are performed. The TDMA is used on the line and the column sweeps in the **R** and **Z** directions, while in the **Φ**–direction, where periodic boundary exists, the lines and the columns form loops (Figure 2.3) and thus the CTDMA is utilized.

Simpler Algorithm Summary

In SIMPLER algorithm we start by guessing the velocity field from which the coefficients for the momentum and the pressure equations are calculated. Next, the pressure equation is solved to obtain a pressure field that is substituted into the momentum equations to solve for the velocity field. In general, the velocity field will not satisfy the continuity equation. Therefore, the pressure–correction equation is solved, to correct the velocity field. This procedure continues until convergence is attained.

CHAPTER 3. ROTOR MODELLING

As the rotor blade spins it imparts a certain amount of momentum to the fluid. This change in momentum is related to sectional aerodynamic and geometric characteristics of the blade. Keeping with our objective of computationally inexpensive rotor modelling, the influence of the rotor on the flowfield is modeled as time averaged source terms embedded in the momentum equations. The source terms, unknown at the start of the iterations, evolve as part of the solution. This chapter describes in detail the coordinate systems used in defining the rotor geometry, the rotor discretization procedure, the calculation of the blade loads and the rotor source terms.

Coordinate Systems

Computational domain cylindrical system, (R,Φ,Z)

The flow field is solved in the cylindrical Computational domain ($\mathbf{R}$,$\mathbf{\Phi}$,$\mathbf{Z}$), with $\hat{e}_R$, $\hat{e}_\Phi$ and $\hat{e}_Z$ as the respective unit vectors. The $\mathbf{Z}$–axis is taken to be parallel to the free stream velocity $\mathbf{V}_\infty$. The absolute velocity at a given point in the computational domain has three components, namely, V_R, V_Φ and V_Z.

Global Cartesian Coordinate System, (X,Y,Z)

This coordinate system is used to define the position of the rotor and the body. The center of the rotor and the nose of the body are defined at the points (X_c,Y_c,Z_c), and (X_b,Y_b,Z_b), respectively (see Figure 3.1). The X axis of this system coincides with the **Z** axis of the cylindrical computational domain. The unit vectors of this Cartesian system, $\hat{e}_X$, $\hat{e}_Y$, $\hat{e}_Z$, are related to those in the cylindrical computational domain by the following matrix relation:

$$\begin{bmatrix} \hat{e}_X \\ \hat{e}_Y \\ \hat{e}_Z \end{bmatrix} = \begin{bmatrix} 0 & 0 & 1 \\ \cos\Phi & -\sin\Phi & 0 \\ \sin\Phi & \cos\Phi & 0 \end{bmatrix} \begin{bmatrix} \hat{e}_{\mathbf{R}} \\ \hat{e}_{\Phi} \\ \hat{e}_{\mathbf{Z}} \end{bmatrix}$$

$$= \mathbf{M_0} \begin{bmatrix} \hat{e}_{\mathbf{R}} \\ \hat{e}_{\Phi} \\ \hat{e}_{\mathbf{Z}} \end{bmatrix} \tag{3.1}$$

Furthermore, the coordinates of the cylindrical computational domain are defined in terms of the global Cartesian system by

$$\begin{aligned} \mathbf{R} &= \sqrt{Y^2 + Z^2} \\ \Phi &= \arctan(Z/Y) \\ \mathbf{Z} &= X \end{aligned} \tag{3.2}$$

The rotation of the rotor is defined in the global Cartesian coordinates such that the axis of rotation of the rotor is along its angular velocity vector $\vec{\omega}$, given by

$$\vec{\omega} = \omega_X \hat{e}_X + \omega_Y \hat{e}_Y + \omega_Z \hat{e}_Z \tag{3.3}$$

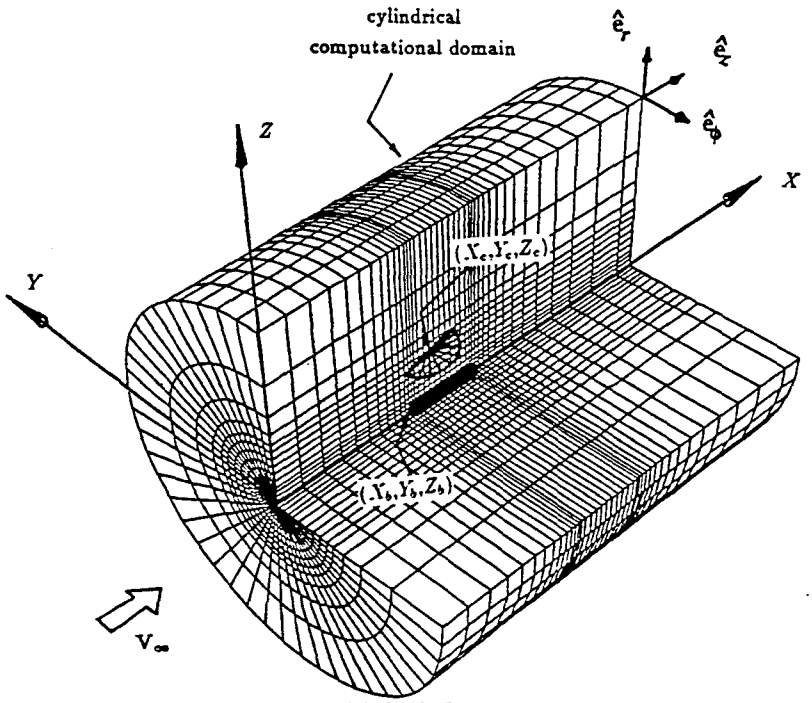

Figure 3.1: Global Cartesian coordinate system

Rotor Based Cartesian System (ξ,η,ζ)

This system is placed at the center of the rotor. The ξ coordinate is perpendicular to the rotor tip path plane and points in the inflow direction, while η and ζ axes lie in the plane of rotation. Using Euler angle rotations and a shift in the origin this system can be related to the global Cartesian system (Figure 3.2) by the following matrix equation:

$$\begin{bmatrix} \xi \\ \eta \\ \zeta \end{bmatrix} = \begin{bmatrix} \cos B & \sin A \sin B & -\cos A \sin B \\ 0 & \cos A & \sin A \\ \sin B & -\sin A \cos B & \cos A \cos B \end{bmatrix} \begin{bmatrix} X - X_c \\ Y - Y_c \\ Z - Z_c \end{bmatrix}$$

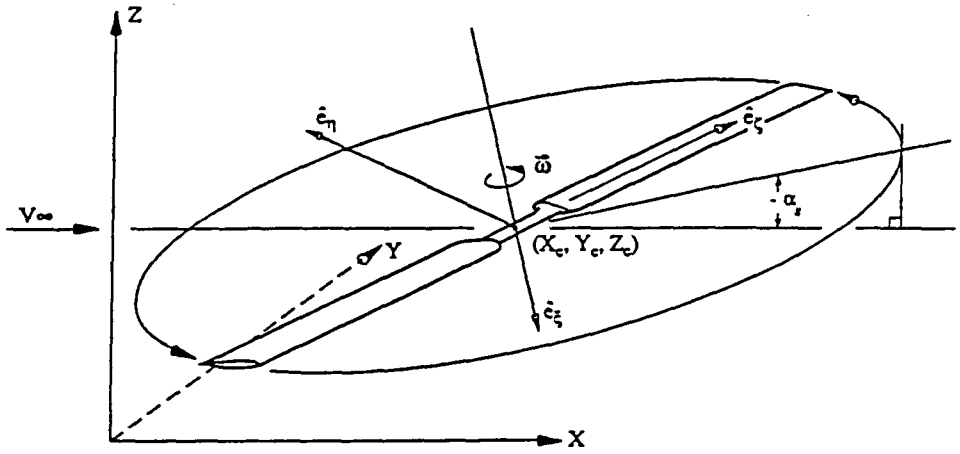

Figure 3.2: Rotor based Cartesian system

$$= \mathbf{M_1} \begin{bmatrix} X - X_c \\ Y - Y_c \\ Z - Z_c \end{bmatrix} \tag{3.4}$$

where A is the pitch angle and B is the lateral angle defining the orientation of the rotor in the global Cartesian system; the derivation of this matrix equation (3.4) is given in Appendix A of Reference [20]. The unit vectors ($\hat{e}_\xi$,$\hat{e}_\eta$,$\hat{e}_\zeta$) are related to the unit vectors ($\hat{e}_X$,$\hat{e}_Y$,$\hat{e}_Z$) through the matrix transformation:

$$\begin{bmatrix} \hat{e}_\xi \\ \hat{e}_\eta \\ \hat{e}_\zeta \end{bmatrix} = \begin{bmatrix} \cos B & \sin A \sin B & -\cos A \sin B \\ 0 & \cos A & \sin A \\ \sin B & -\sin A \cos B & \cos A \cos B \end{bmatrix} \begin{bmatrix} \hat{e}_X \\ \hat{e}_Y \\ \hat{e}_Z \end{bmatrix} \tag{3.5}$$

Rotor Based Cylindrical Polar System, (r,θ,z)

This coordinate system is used to keep track of the rotor blade as it spins about its axis. Like in the rotor based Cartesian system, the z axis in this system is normal to the rotor tip path plane and points in the inflow direction. In other words, the z axis coincides with the ξ axis of the rotor based Cartesian system. Thus, the rotor based cylindrical coordinates are defined such that,

$$\begin{aligned} \xi &= z \\ \eta &= r\cos\theta \\ \zeta &= r\sin\theta \end{aligned} \tag{3.6}$$

and the unit vectors are related to those in the rotor based Cartesian system by

$$\begin{aligned} \begin{bmatrix} \hat{e}_r \\ \hat{e}_\theta \\ \hat{e}_z \end{bmatrix} &= \begin{bmatrix} 0 & \cos\theta & \sin\theta \\ 0 & -\sin\theta & \cos\theta \\ 1 & 0 & 0 \end{bmatrix} \begin{bmatrix} \hat{e}_\xi \\ \hat{e}_\eta \\ \hat{e}_\zeta \end{bmatrix} \\ &= \mathbf{M_2} \begin{bmatrix} \hat{e}_\xi \\ \hat{e}_\eta \\ \hat{e}_\zeta \end{bmatrix} \end{aligned} \tag{3.7}$$

As shown in Figure 3.3, the position of a blade is described by the azimuth angle ψ, which is measured from an axis coinciding with a component of the freestream velocity parallel to the plane of rotation, and related to the angle θ by

$$\theta = \frac{\pi}{2} - \psi \tag{3.8}$$

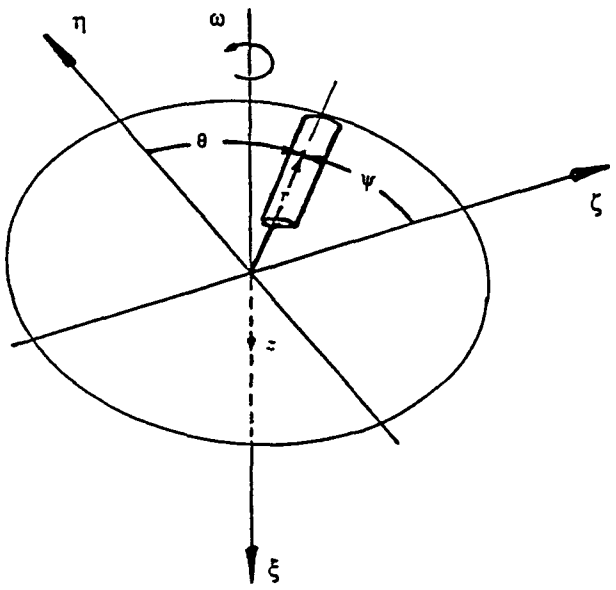

Figure 3.3: Rotor based cylindrical polar system

Blade Deflection Coordinate System, (n,θ,s)

This coordinate system is needed to describe the blade deflection or sweep as shown in Figure 3.4. The coordinates (n,θ,s) of this system are chosen such that s is in the spanwise direction of the blade, and that the unit vector $\hat{e}_s$ is tangent to the blade deflection at a given point. The unit vector $\hat{e}_\theta$ is common to both (n,θ,s) and (r,θ,z) systems, while the unit vector $\hat{e}_n$ is perpendicular to $\hat{e}_\theta$ and $\hat{e}_s$. The matrix relation that relates the blade deflection to the plane of rotation is

$$\begin{bmatrix} \hat{e}_n \\ \hat{e}_\theta \\ \hat{e}_s \end{bmatrix} = \begin{bmatrix} \sin\delta & 0 & -\cos\delta \\ 0 & 1 & 0 \\ \cos\delta & 0 & \sin\delta \end{bmatrix} \begin{bmatrix} \hat{e}_r \\ \hat{e}_\theta \\ \hat{e}_z \end{bmatrix}$$

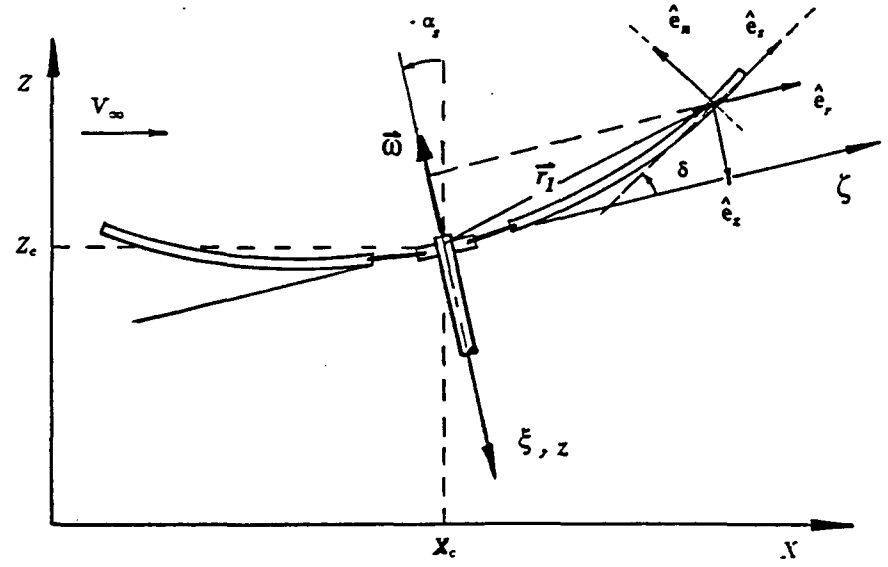

Figure 3.4: Blade deflection coordinate system

$$= \mathbf{M_3} \begin{bmatrix} \hat{e}_r \\ \hat{e}_\theta \\ \hat{e}_z \end{bmatrix} \tag{3.9}$$

As a final note, on the description of coordinate systems, one should add that $\mathbf{M_0}$, $\mathbf{M_1}$, $\mathbf{M_2}$ and $\mathbf{M_3}$ are all orthonormal transformations. The inverse of these matrices can be easily obtained by taking their transpose. Thus

$$\mathbf{M_0}^{-1} = \mathbf{M_0}^{\mathbf{T}} \qquad \mathbf{M_1}^{-1} = \mathbf{M_1}^{\mathbf{T}}$$

$$\mathbf{M_2}^{-1} = \mathbf{M_2}^{\mathbf{T}} \qquad \mathbf{M_3}^{-1} = \mathbf{M_3}^{\mathbf{T}}$$

Using the transformation matrices, a vector in any coordinate system can be transformed to other systems by applying the proper sequence of transformations.

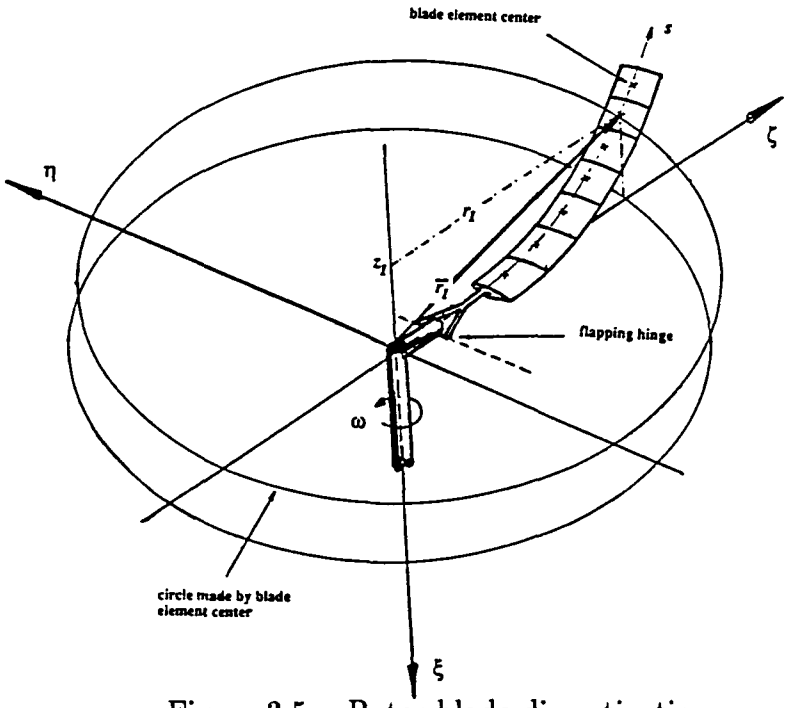

Figure 3.5: Rotor blade discretization

Rotor Discretization

To evaluate the blade source terms the rotor must be discretized into spanwise elements as shown in Figure 3.5. By doing so, we are assuming that the blade properties such as, chord length, airfoil thickness, plane deflections, and cross–sectional area are constant over that element. Since the effect of the spinning blades is lumped at specific grid points through which the centers of the discretized sections pass, circles with radius from the center of the rotor to the center of the discretized section are drawn (Figure 3.5) to obtain the path of the blade section center. The main task is to determine the grid cells of the computational domain through which these circles pass by. A general algorithm developed by Mathur [20] has been modified to accommodate the new coordinate systems essential for the present work.

For a given blade element on the discretized rotor shown in Figure 3.5, the vector

$$\vec{\mathbf{r}}_1 = \mathbf{r}_1\hat{\mathbf{e}}_\mathbf{r} + \mathbf{z}_1\hat{\mathbf{e}}_\mathbf{z} \tag{3.10}$$

defines the the position of the blade element center in the rotor based cylindrical system. As the blade revolves around its axis, the center of the blade element will describe a circle traced by the loci of the points:

$$\begin{aligned} r &= r_1 \\ z &= z_1 \end{aligned} \tag{3.11}$$

Our objective is to transform the above equation to the (**R**,**Φ**,**Z**) system so that the indices of the control volumes, which make up the circle traversed by the blade section in the computational domain, can be determined. The blade source terms are to be added only at these specific grid points. Rewriting Equation 3.11 in the rotor based Cartesian system, we get

$$\begin{aligned} \xi &= z_1 \\ \eta &= r_1 \cos\theta \\ \zeta &= r_1 \sin\theta \end{aligned} \tag{3.12}$$

The next step is to write the above equations in global Cartesian system using relation 3.4 to obtain

$$\begin{bmatrix} X \\ Y \\ Z \end{bmatrix} = \begin{bmatrix} X_c \\ Y_c \\ Z_c \end{bmatrix} + \mathbf{M}_1^\mathbf{T} \begin{bmatrix} \xi \\ \eta \\ \zeta \end{bmatrix} \tag{3.13}$$

where X_c,Y_c and Z_c are the center of the rotor disc in global Cartesian system. Expanding and rearranging Equation 3.13, the parametric equations of a circle can now be rewritten in the global Cartesian system as,

$$X = A_x \cos\theta + B_x \sin\theta + C_x \tag{3.14}$$

$$Y = A_y \cos\theta + B_y \sin\theta + C_y \tag{3.15}$$

$$Z = A_z \cos\theta + B_z \sin\theta + C_z \tag{3.16}$$

where A_x, B_x,...., C_z are coefficients defined by the orientation and size of the circle.

Finally we transfer Equations 3.14–3.16 to the cylindrical computational domain, using relation 3.2, to obtain the following parametric equations of a circle:

$$\mathbf{R} = \left[(A_y \cos\theta + B_y \sin\theta + C_y)^2 + (A_z \cos\theta + B_z \sin\theta + C_z)^2\right]^{\frac{1}{2}} \tag{3.17}$$

$$\mathbf{\Phi} = \arctan\left[(A_z \cos\theta + B_z \sin\theta + C_z) / (A_y \cos\theta + B_y \sin\theta + C_y)\right] \tag{3.18}$$

$$\mathbf{Z} = A_x \cos\theta + B_x \sin\theta + C_x \tag{3.19}$$

Once the equation of the circle is determined in the computational domain the following steps are utilized to locate the control volumes through which the circle passes.

1. Determine the **R**,**Φ**,**Z** extrema from Equations 3.17–3.19, then obtain the corresponding maximum and minimum plane indices. By doing so the region in the computational domain that the circle does not occupy is eliminated.

2. Traverse the **Z** grid planes of the computational domain that the circle occupies, to solve for θ from Equation 3.19. In general, two intersections will be found for each plane. Substitute the θ's in Equations 3.17 and 3.18 to get the two

intersection points. For each intersection point, indices of two neighboring control volumes can be located and saved. This procedure should be repeated for all the **Z** planes between the extrema of **Z**.

3. Repeat step 2 for the **Φ** and the **R** grid planes. Proper care should be taken when searching the **R**–planes. One, two or even four intersection points can be found for a given **R**–plane, due to the curved nature of these planes.

4. With careful bookkeeping, the location of all the control volumes, through which the circle passes can be located. In addition, the $\Delta\theta$s (the angular distance traversed by the center of the blade element in passing through a control volume) is also obtained and saved. The $\Delta\theta$s are needed in the calculations of the rotor blade source terms as will be described in the next section.

5. The four steps above must be repeated for each of the V_R, V_Φ and V_Z staggered grid system.

Calculation of Rotor Blade Source Terms

In calculating the rotor forces and blade source terms, our objective is to use the computed velocity field to obtain the local angle of attack and the Mach number at each blade element. Then, a look-up table corresponding to the given blade section is used to get the local C_l and C_d values, from which the rotor forces and the source terms can be calculated. To show this procedure in a more detailed manner, let $\vec{V}$ be the absolute velocity vector in the computational domain located at the position (s,θ) on a given blade. thus,

$$\vec{V} = V_R\hat{e}_R + V_\Phi\hat{e}_\Phi + V_Z\hat{e}_Z \tag{3.20}$$

The above velocity vector, through sequence of transformations can be transferred to the blade deflection coordinate system (n,θ,s) as

$$\vec{V} = v_n\hat{e}_n + v_\theta\hat{e}_\theta + v_s\hat{e}_s \tag{3.21}$$

where

$$\begin{bmatrix} v_n \\ v_\theta \\ v_s \end{bmatrix} = \mathbf{M_3M_2M_1M_0} \begin{bmatrix} V_R \\ V_\Phi \\ V_Z \end{bmatrix} \tag{3.22}$$

The blade velocity due to its rotation about its axis is given in (n,θ,s) system by

$$\vec{V}_{bl} = \mathbf{M_3}\left(\mathbf{M_2M_1}\vec{\omega} \times \vec{\mathbf{r}}\right) \tag{3.23}$$

where $\vec{\omega}$ is defined in Equation 3.3, and $\vec{\mathbf{r}}$ in Equation 3.10. Using relation 3.22 and 3.23, the flow velocity relative to the blade at a given point on the s axis can be written as

$$\begin{aligned} \vec{V}_{rel} &= \vec{V} - \vec{V}_{bl} \\ &= \mathbf{M_3M_2M_1M_0}\vec{\mathbf{V}} - \mathbf{M_3}\left(\mathbf{M_2M_1}\vec{\omega} \times \vec{\mathbf{r}}\right) \\ &= v'_n\hat{e}_n + v'_\theta\hat{e}_\theta + v'_s\hat{e}_s \end{aligned} \tag{3.24}$$

In most helicopter configurations, the rotor blades are permitted to flap about a flapping hinge as illustrated in Figure 3.6. For a given blade element of a rotor blade in a flapping motion the tangential velocity of the center of the blade element with respect to a flapping hinge is given by

$$v_{flap} = \dot{\beta}R_f \tag{3.25}$$

where R_f is the radial distance from the hinge off-set to the center of the blade element and $\dot{\beta}$ is the flapping rate. The flapping motion of a rotor is usually represented by a Fourier series:

$$\beta = a_o + \sum_{n=1}^{N} [a_n \cos(n\psi) + b_n \sin(n\psi)] \tag{3.26}$$

where β is positive if the blade flaps up. Therefore, the flapping rate can be determined from Equation 3.26 as

$$\begin{aligned} \dot{\beta} &= \frac{\partial \beta}{\partial \psi}\frac{\partial \psi}{\partial t} \\ &= \frac{\partial \beta}{\partial \psi}\omega \end{aligned} \tag{3.27}$$

where ω is the magnitude of the blade rotation, and $\frac{\partial \beta}{\partial \psi}$ is the variation of flapping motion with the azimuthal angle. As the rotor blade flaps upward the relative wind contribution due to flapping will be downward. Thus, the relative velocity normal to a blade element can be corrected to include flapping contribution as:

$$v''_n = v'_n - \dot{\beta} R_f \tag{3.28}$$

The aerodynamic forces on an airfoil section at location s, is primarily a function of the angle of attack α at that section (Figure 3.7), and α is defined by

$$\alpha = \phi - \epsilon \tag{3.29}$$

where ϵ is the angle made by the components of the relative velocity normal to the unit vector $\hat{e}_s$ given by:

$$\epsilon = \arctan\left(-v''_n / v'_\theta\right) \tag{3.30}$$

and ϕ is the angle of twist at a section with respect to the plane of rotation. This angle, ϕ, in turn is determined from the rotor blade geometric twist and from the

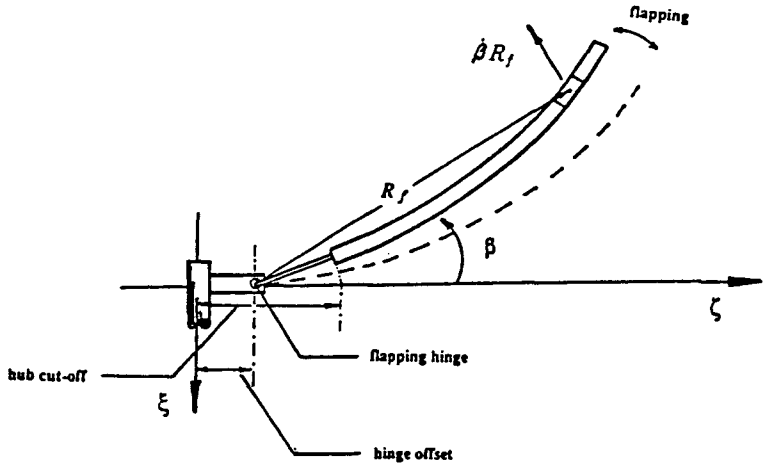

Figure 3.6: Blade flapping

cyclic pitch variation of the blade root section, θ_r. Like the flapping motion, the blade root section cyclic pitch variation can be written in terms of a Fourier series:

$$\theta_r = A_o + \sum_{n=1}^{N} [A_n \cos(n\psi) + B_n \sin(n\psi)] \tag{3.31}$$

The next step towards the determination of the aerodynamic forces on a blade element is to determine the local Mach number, M'. The local Mach number can be obtained from the following relation:

$$M' = \frac{v'}{a_\infty} \tag{3.32}$$

where a_∞, is the speed of sound and v', is the relative velocity seen by the airfoil section, given by

$$v' = \sqrt{{v''_n}^2 + {v'_\theta}^2} \tag{3.33}$$

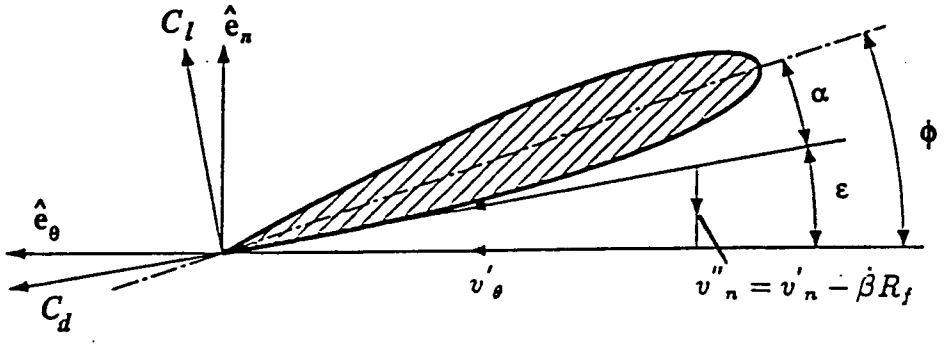

Figure 3.7: Aerodynamic forces at a blade section

Once the angle of attack and the local Mach number are obtained, the section aerodynamic coefficients C_l and C_d are easily determined from the look-up table. It is important to note that by considering the local Mach number in the determination of the aerodynamic coefficients, C_l and C_d, we are implicitly accounting for the compressibility effects on the aerodynamic characteristics of the blade section.

The lift and the drag forces experienced by the blade section are:

$$\begin{aligned} L &= \frac{1}{2}\rho v'^2 C_l \, c \, ds \\ D &= \frac{1}{2}\rho v'^2 C_d \, c \, ds \end{aligned} \tag{3.34}$$

where c, is the blade chord, and ds, is the length of the blade element. Furthermore, lift and the drag forces can be resolved into the $\hat{e}_n$ and $\hat{e}_\theta$ direction as follows

$$f_n = L\cos\epsilon - D\sin\epsilon$$

$$f_\theta = L\sin\epsilon + D\cos\epsilon \tag{3.35}$$

The force in the spanwise coordinate, f_s, is zero since there are no aerodynamic forces acting in that direction. The resultant aerodynamic force vector $\vec{f}$ is now written as

$$\vec{f} = f_n\hat{e}_n + f_\theta\hat{e}_\theta + f_s\hat{e}_s \tag{3.36}$$

The above force vector is transformed to the computational cylindrical system through:

$$\vec{F} = \mathbf{M_0}^{\mathrm{T}}\mathbf{M_1}^{\mathrm{T}}\mathbf{M_2}^{\mathrm{T}}\mathbf{M_3}^{\mathrm{T}}\vec{\mathbf{f}} \tag{3.37}$$

where $\vec{F}$ is the resultant aerodynamic force vector on the blade. Consequently, $-\vec{F}$ is then the instantaneous force vector acting on a fluid element at location (s,θ), which must be added to the momentum equation as an external force acting on the fluid. However, for a time averaged solution, only a time fraction of this force is to be added at a computational cell. This time fraction is determined as follows. The time taken by the center of the blade element to traverse one revolution is:

$$t_{1.rev} = \frac{2\pi}{\omega} \tag{3.38}$$

and the time the center of a blade element spends in a given control volume of width $\Delta\theta$ radians is:

$$t_{\Delta\theta} = \frac{\Delta\theta}{\omega} \tag{3.39}$$

therefore, the fractional time that the blade element spends in a cell is:

$$\begin{aligned} t_{frac} &= \frac{\Delta\theta/\omega}{2\pi/\omega} \\ &= \frac{\Delta\theta}{2\pi} \end{aligned} \tag{3.40}$$

for a rotor with N blades the time averaged source term to be added to the momentum equation is

$$\vec{S} = \frac{N\ \Delta\theta}{2\pi}\left(-\vec{F}\right) \tag{3.41}$$

The source terms are grid specific and are calculated from the velocity field of the previous iteration level. Figure 3.8, summarizes the coupling of the SIMPLER algorithm and the rotor source term calculations.

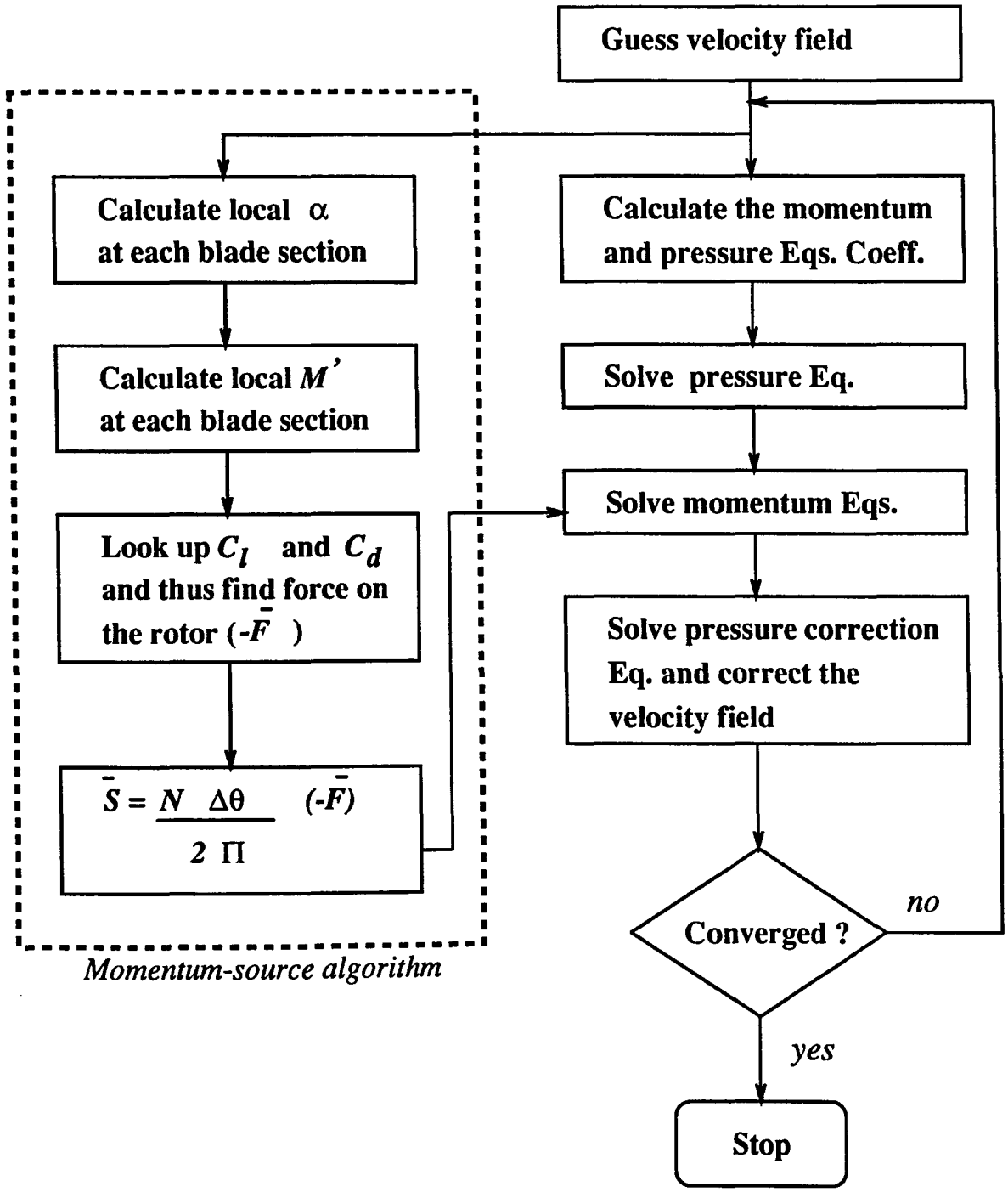

Figure 3.8: Momentum-source/SIMPLER algorithms coupling

CHAPTER 4. RESULTS AND DISCUSSION

A computer code has been developed to analyze the flow field and load distributions of a rotor/airframe configuration. The code consists of two parts. The first is the flow field solver based on the SIMPLER algorithm. The second part implements the rotor model using source–momentum procedure. The results of a rotor in forward flight from the present analysis are validated with experimental results and previously developed 3–D Cartesian code [21]. The ability of the code to predict aerodynamic interactions of rotor/airframe problem is then demonstrated on a simplified geometry representing a helicopter fuselage.

Forward Flight Code Validation

Test Cases

In order to validate the 3–D, cylindrical, N–S rotor code, calculations are carried out for three cases of a rotor in forward flight. The three cases span a range of advance ratios from low (0.064) to a relatively high (0.227). The helicopter rotor chosen is the four–bladed H–34 rotor. The choice of the rotor is motivated by the availability of a large experimental and theoretical data base. Table 4.1 describes the important geometric characteristics of the H–34 rotor. Flight and test operating conditions for the three cases investigated are given in Table 4.2.

Table 4.1: H–34 rotor characteristics

Radius	8.5400 m
Chord	0.4170 m
Hub radius	1.3968 m
Hinge offset	0.3049 m
Number of Blades	4
Twist	-8 deg.
Airfoil type	Modified NACA 0012

Table 4.2: Forward flight test conditions

	Case 1	Case 2	Case 3
μ	0.227	0.129	0.064
$\mathbf{V}_\infty$, m/s	45.27	24.70	11.84
V_{tip}, m/s	198.54	191.38	185.13
ω, RPM	222	214	207
ρ, kg/m^3	1.103	1.309	1.309
$\alpha_{s_{long}}$, deg.	-4.0	-0.7	-0.6
$\alpha_{s_{lat}}$, deg.	-2.1	-0.6	-2.6
$\alpha_{TPP_{long}}$, deg.	-4.204	-1.131	-0.612
$\alpha_{TPP_{lat}}$, deg.	-1.851	-0.084	-2.258
Reference	[23], Table 14	[23], Table 9	[23], Table 6

Table 4.3: Blade pitch harmonics

	Case 1		Case 2		Case 3	
n	A_n	B_n	A_n	B_n	A_n	B_n
0	15.1690	0.0000	11.2590	0.0000	12.3260	0.0000
1	1.5710	-5.9310	1.9660	-2.5790	2.2160	-0.3450
2	-0.0760	0.0610	0.0320	0.0180	0.1140	-0.0230
3	0.0180	0.1200	0.0270	0.0910	-0.0410	0.0000
4	0.0440	-0.0350	0.0820	-0.0820	-0.0270	-0.0270
5	-0.0260	-0.0230	-0.0230	-0.0410	0.0000	0.0360
6	0.0000	-0.0060	0.0230	-0.0230	0.0360	-0.0180
7	0.0230	0.0120	0.0050	-0.0050	-0.0090	-0.0180
8	0.0000	0.0180	0.0320	0.0050	0.0000	0.0000
9	-0.0120	0.0090	0.0090	0.0000	0.0180	-0.0230
10	0.0030	0.0000	0.0050	0.0050	0.0050	0.0000

As mentioned in the previous chapter helicopter rotor may undergo a cyclic pitch and flapping motion. The kinematics of the motion are given with the flight operating conditions and are included in the present code to simulate the rotor motion as recorded in the flight test. The pitch and flapping motion are described by harmonic series. The coefficients of the harmonics are listed in Table 4.3 and 4.4. It should be noted that the cyclic lagging motion which most rotor possess is ignored in the current analysis. Also, no elastic blade motion is included and no iterative trim procedure is attempted to correct the pitch angle to obtain a specific lift and momentum. However, the longitudinal and the lateral tip–path plane angles are corrected such that $\alpha_{TPP_{long}} = \alpha_{s_{long}} - a_1$ and $\alpha_{TPP_{lat}} = \alpha_{s_{lat}} - b_1$. The rotor blade pre-coning angle is set equal to the zero-flapping harmonic coefficient (a_0).

The calculations for the three cases are performed on the same ($50 \times 40 \times 58$) grid over a cylindrical domain of 40 rotor diameters in diameter and 62 rotor diameters in

Table 4.4: Blade flapping harmonics

	Case 1		Case 2		Case 3	
n	a_n	b_n	a_n	b_n	a_n	b_n
0	3.8640	0.0000	3.5900	0.0000	3.8640	0.000
1	0.2040	-0.2490	0.4310	-0.5160	0.2040	-0.249
2	-0.1510	-0.0900	0.0020	0.2790	-0.1510	-0.090
3	0.0000	-0.2200	0.2000	-0.0610	0.0000	-0.220
4	0.0820	-0.0450	0.1220	0.1050	0.0820	-0.045
5	0.0000	-0.0040	0.0080	-0.0530	0.0000	-0.004
6	-0.0080	-0.0330	0.0630	0.0360	-0.0080	-0.033
7	0.0200	0.0000	0.0320	0.0180	0.0200	0.000
8	-0.0080	-0.0120	0.0570	0.0220	-0.0080	-0.012
9	0.0200	-0.0200	0.0200	-0.0140	0.0200	-0.020
10	0.0080	-0.0290	0.0470	0.0120	0.0080	-0.029

height. The converged solutions are obtained within 350 to 450 iterations with each iteration taking about 10 CPU seconds on a CRAY-YMP.

Blade Load Prediction

The aerodynamic loads for $\mu = 0.227$ case as a function of azimuthal location, at radial positions of r/R =0.25, 0.40, 0.55, 0.75, 0.85, and 0.90, are presented in Figures 4.1 through 4.3. In general, the correlation of blade loading between the cylindrical code and the 3–D Cartesian code [21] are very good. In Figure 4.1 comparison between the experimental loads and the loads computed using the 3–D Cartesian code as well as the present code at stations r/R =0.25 and 0.75 are shown. The results from this analysis and the 3–D Cartesian code match quite well. Any discrepancy between the two computational results can be attributed to differences in grid density. At station r/R =0.25 the predicted lift loads over-estimate the

measured loads slightly on the advancing side of the rotor. This over-estimation is in reality a shift between computed and measured loads since the lagging motion has not been compensated for in the current analysis. In the same figure, the load phase is captured well for r/R =0.75 curve. However, over-prediction of lift loads is observed for the azimuth angle range between 120 to 230 degrees.

In the next two figures (4.2, 4.3) the correlation of numerical results with field test data is quite good. The trend in load distribution observed at r/R =0.25 continue until station r/R =0.55, whereas the trend at the outboard region of the rotor is similar to station r/R =0.75.

The predicted results for the case of $\mu = 0.129$ are also compared to experimental data and found to be in excellent agreement up to r/R =0.75. In Figures 4.4 through 4.6, at the outboard region the trend in load is good but the absolute load values are under-predicted between the load peaks. The rotor wake convection in this case is slower than the $\mu = 0.227$ case. Therefore, the rotor's wake strongly influences the blade loading. This is evident in the appearance of the sharp peaks in the load distributions. Again the results are compared to predictions obtained from the 3–D Cartesian code for validating the current code. As can be seen from Figure 4.4 the two theoretical results are in good agreement. The low advance ratio ($\mu = 0.064$) theoretical airloads correlate only reasonably with experimental results as seen in Figures 4.7– 4.9.

In Figures 4.5, 4.6, 4.8, and 4.9 the uniform inflow model and the distorted wake inflow model results, from Reference [24], are plotted with current predicted results and experimental data. The uniform inflow model results are characterized by the lack of any local peaks, that can be observed specially at the outboard region of the

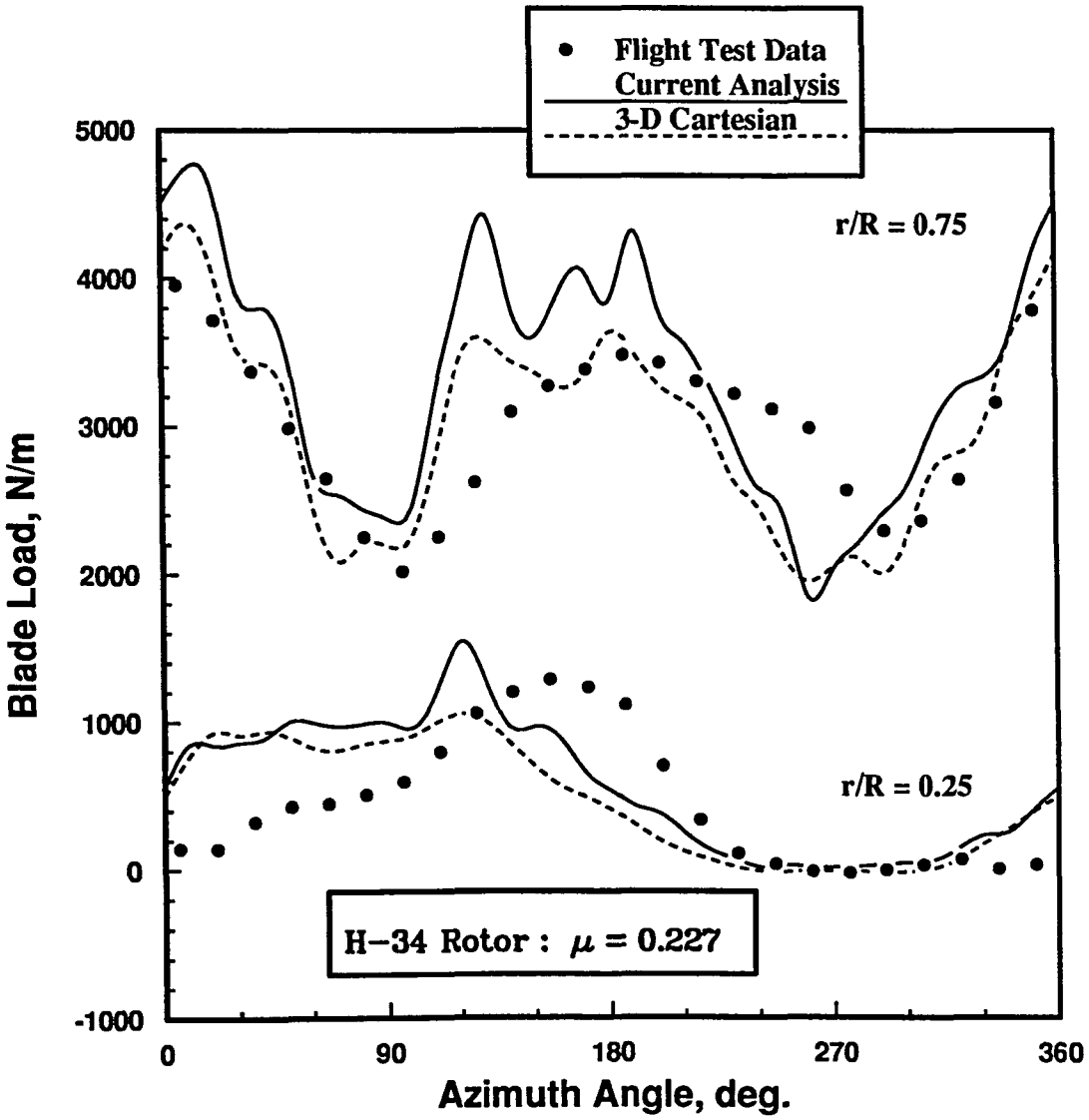

Figure 4.1: Blade load at r/R =0.25 and 0.75 for μ =0.227

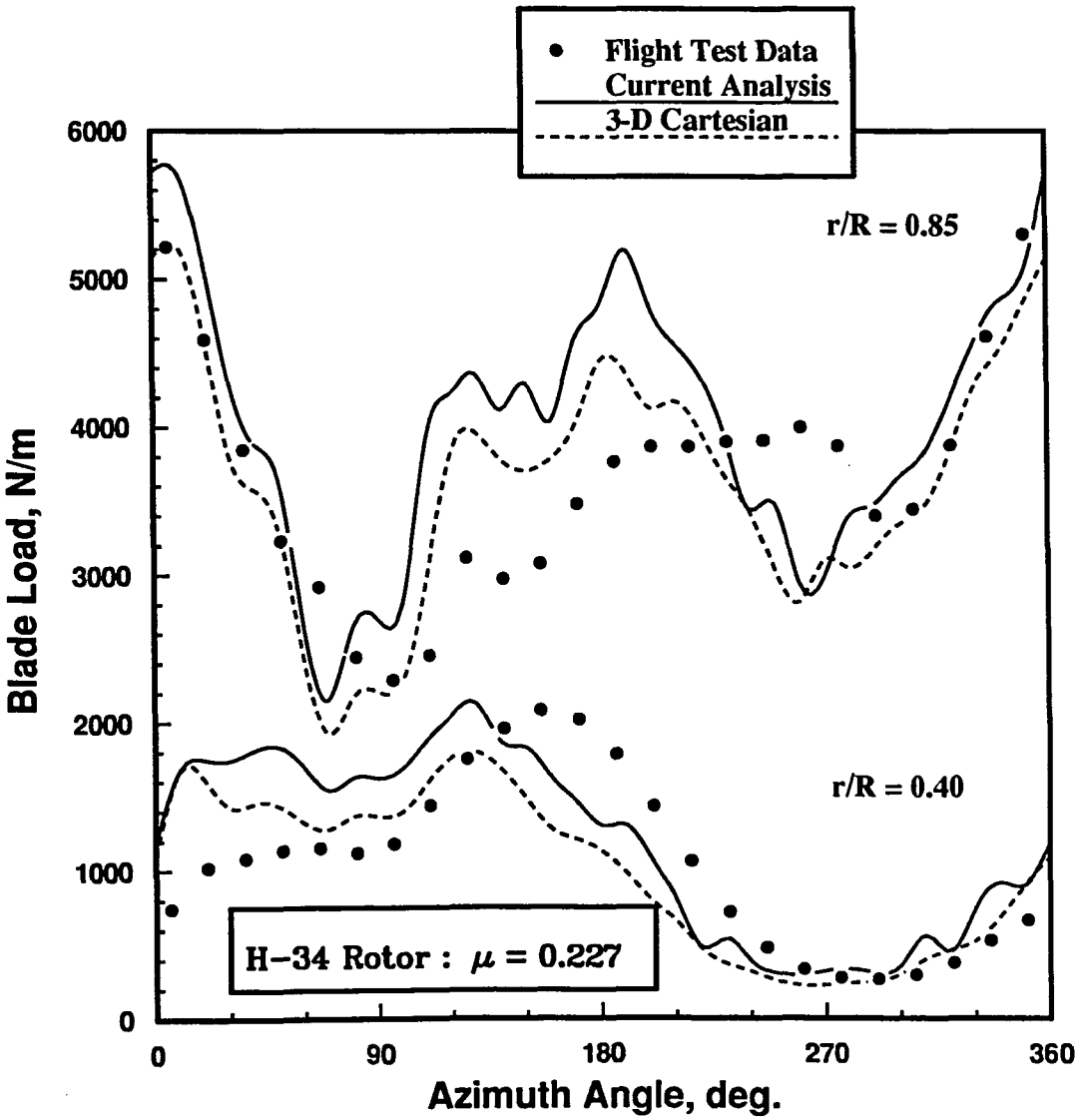

Figure 4.2: Blade load at r/R =0.40 and 0.85 for μ =0.227

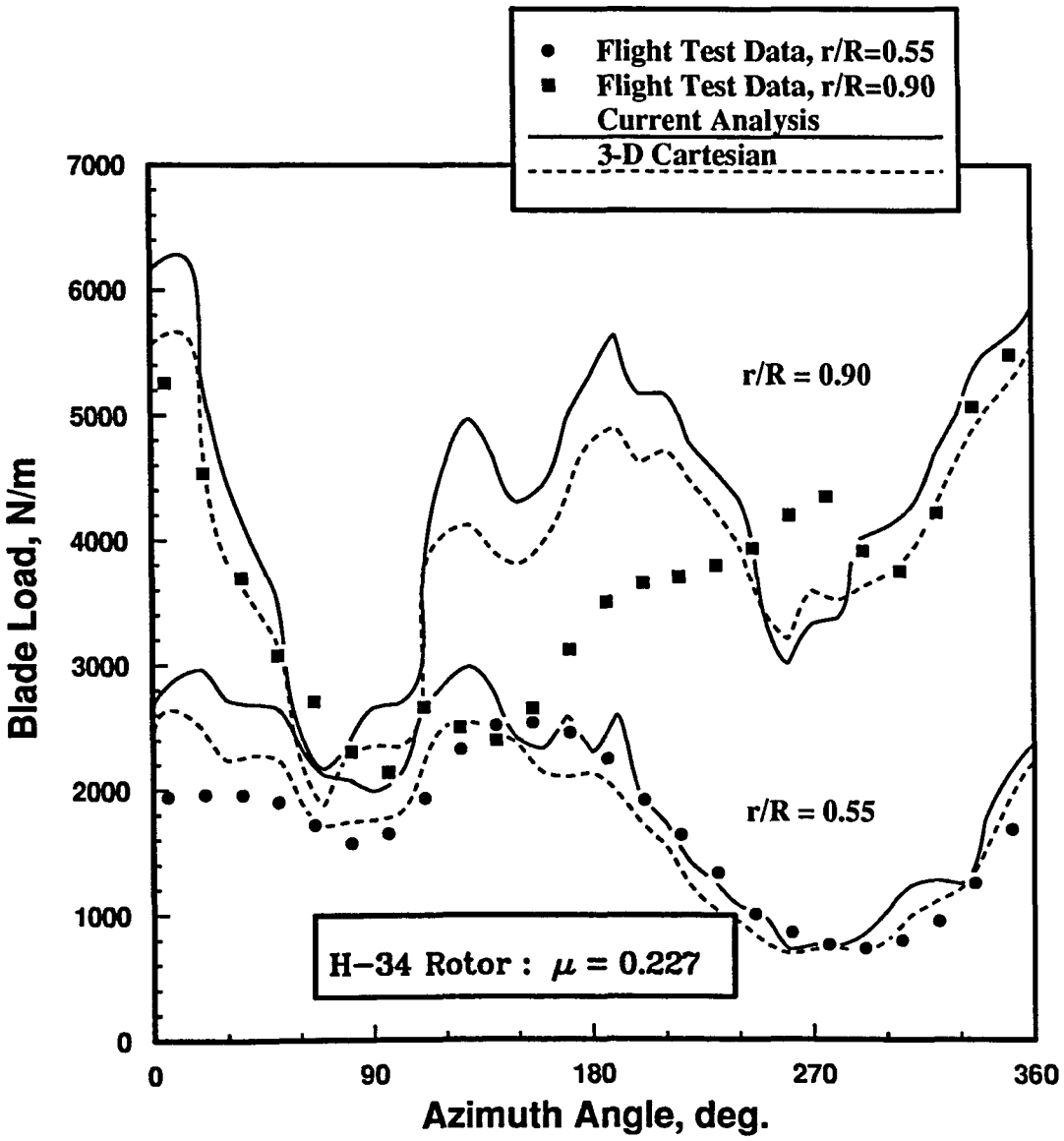

Figure 4.3: Blade load at r/R =0.55 and 0.90 for μ =0.227

rotor. This is expected, since the load distribution of the uniform inflow model is related only to the non-induced velocity variation, which is a combination of the rotor forward and rotational speeds. The rotor loads predicted by the distorted wake inflow model on the other hand, possess harmonic behavior that is closer to the experimental results. However, they tend to over-predict or under-predict the amplitudes of the local load peaks by fairly a wide margin. The better load predictions of the current analysis are evident and clearly seen in all the figures presented. The peak–to–peak load levels and the trend are consistently demonstrated to be in good agreement with flight load data, while the accuracy of predicting the exact value of the load distribution varied from very good to fair.

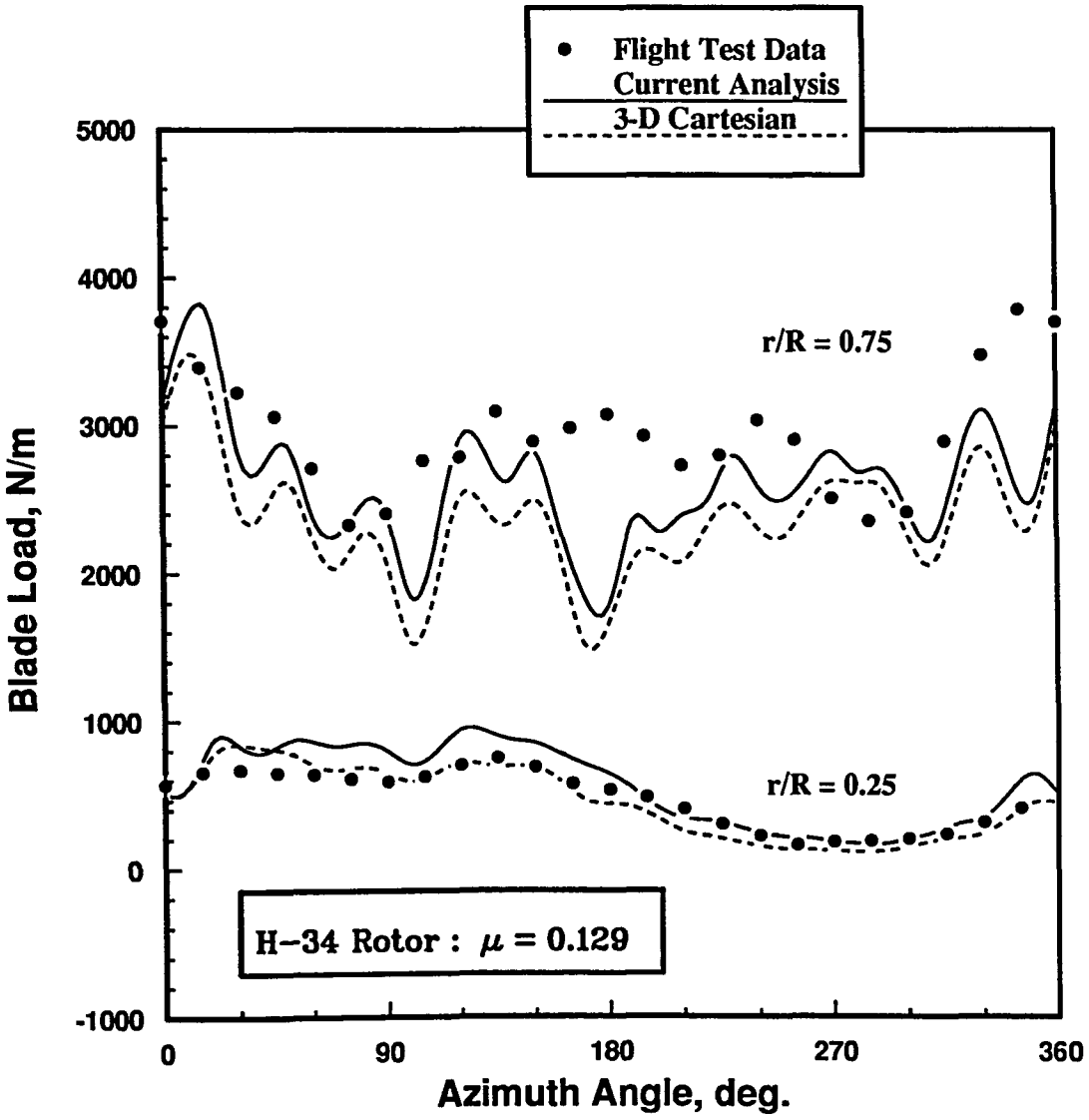

Figure 4.4: Blade load at r/R =0.25 and 0.75 for μ =0.129

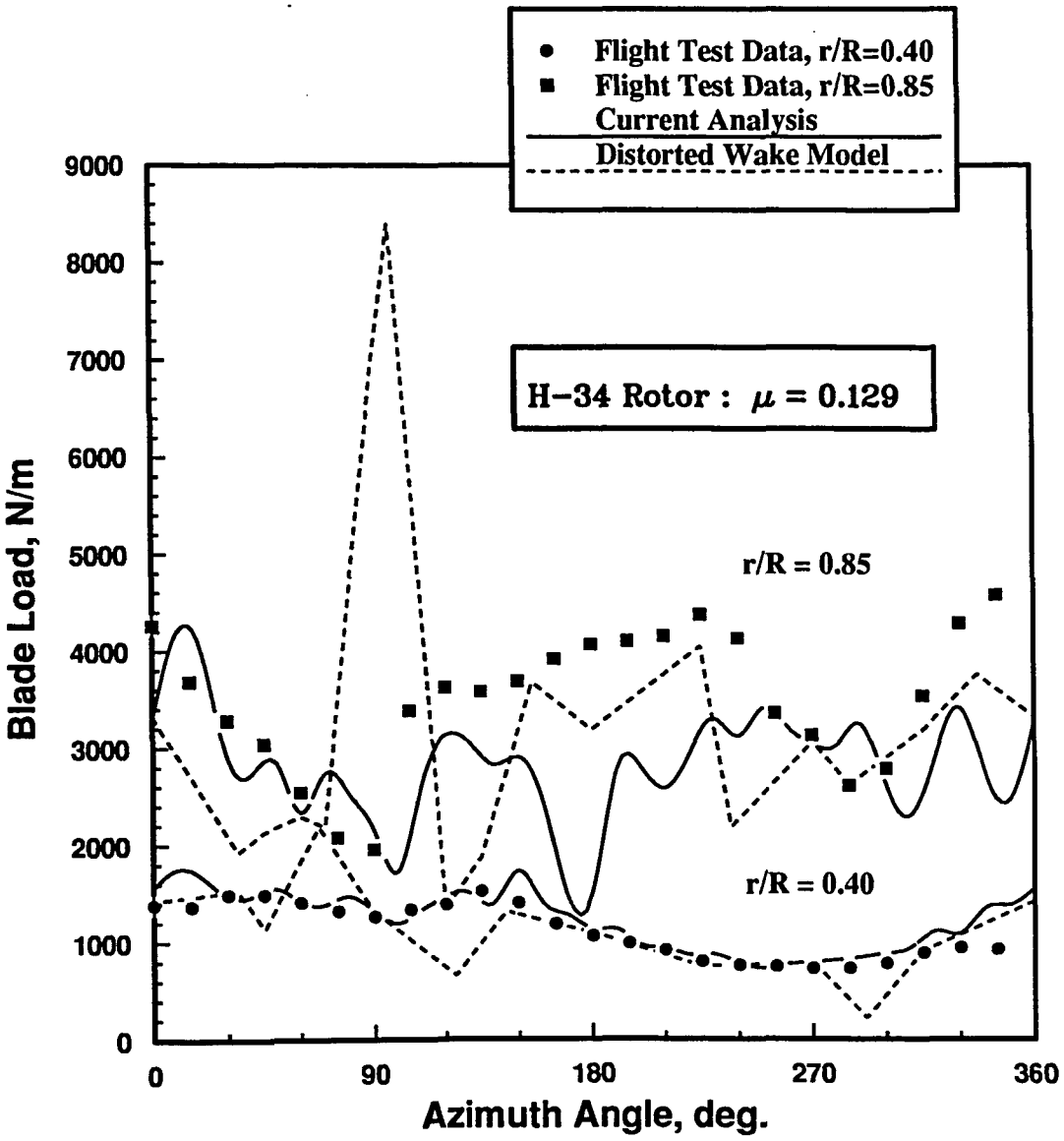

Figure 4.5: Blade load at r/R =0.40 and 0.85 for μ =0.129

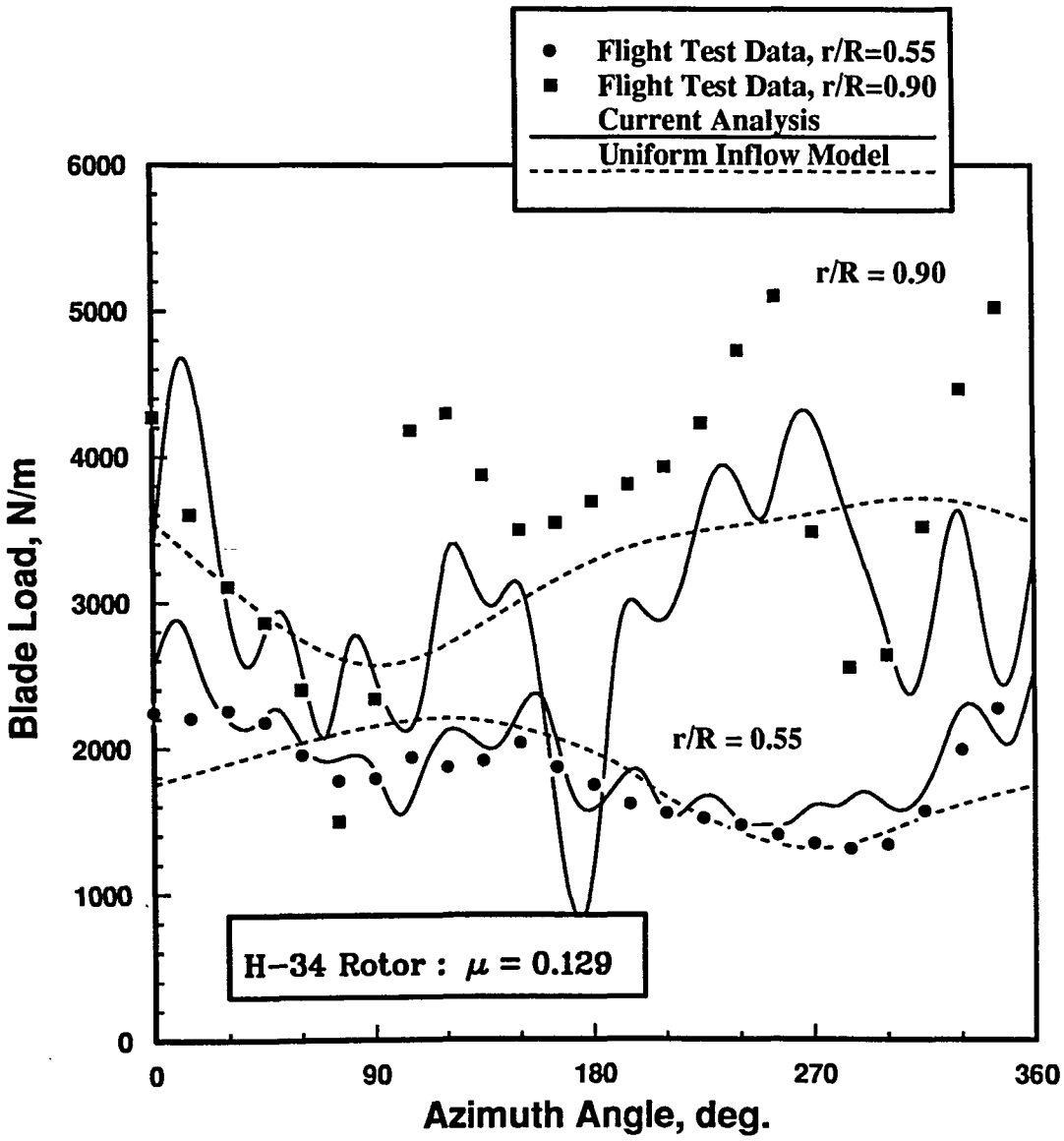

Figure 4.6: Blade load at r/R =0.55 and 0.90 for μ =0.129

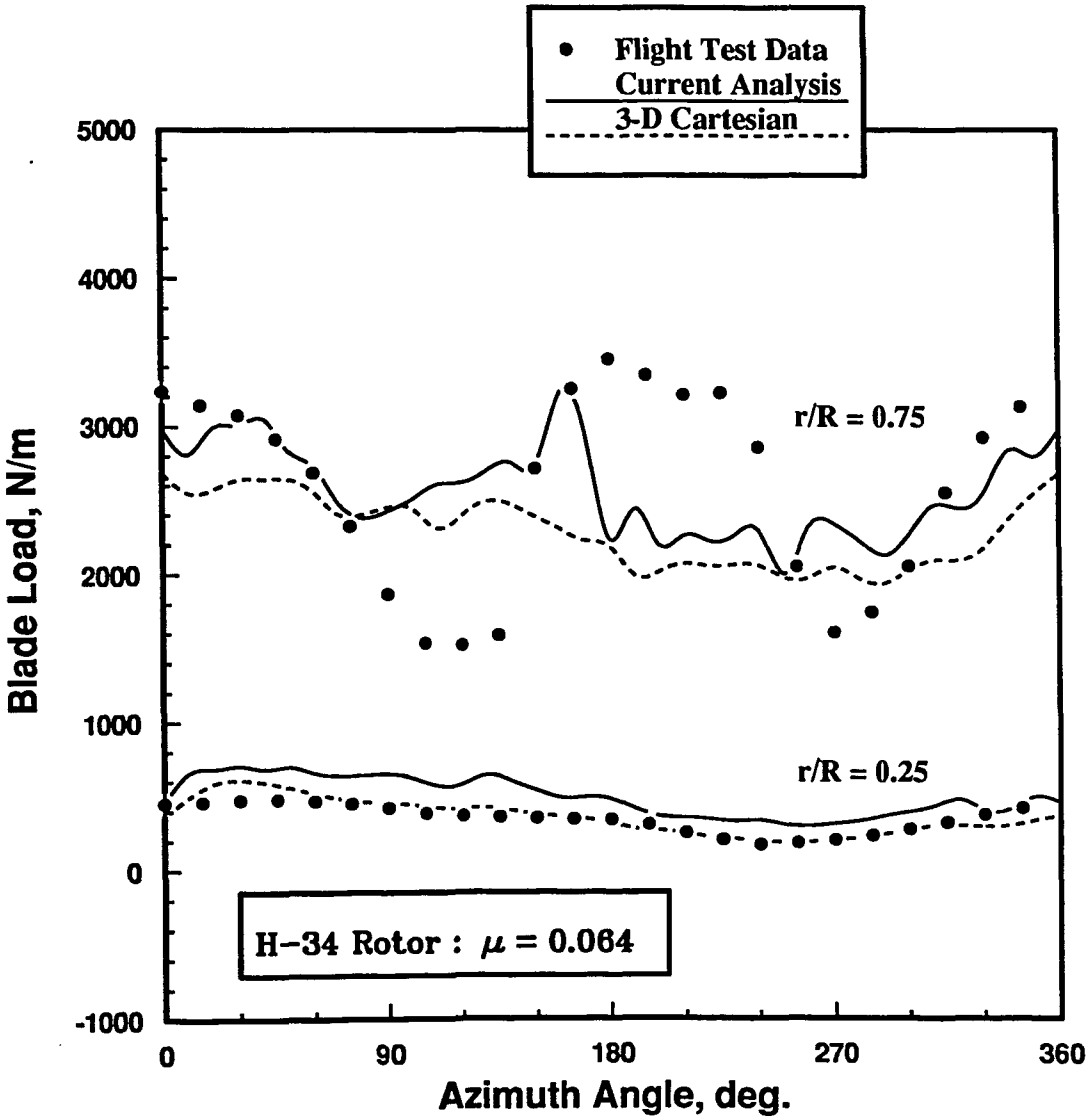

Figure 4.7: Blade load at r/R =0.25 and 0.75 for μ =0.064

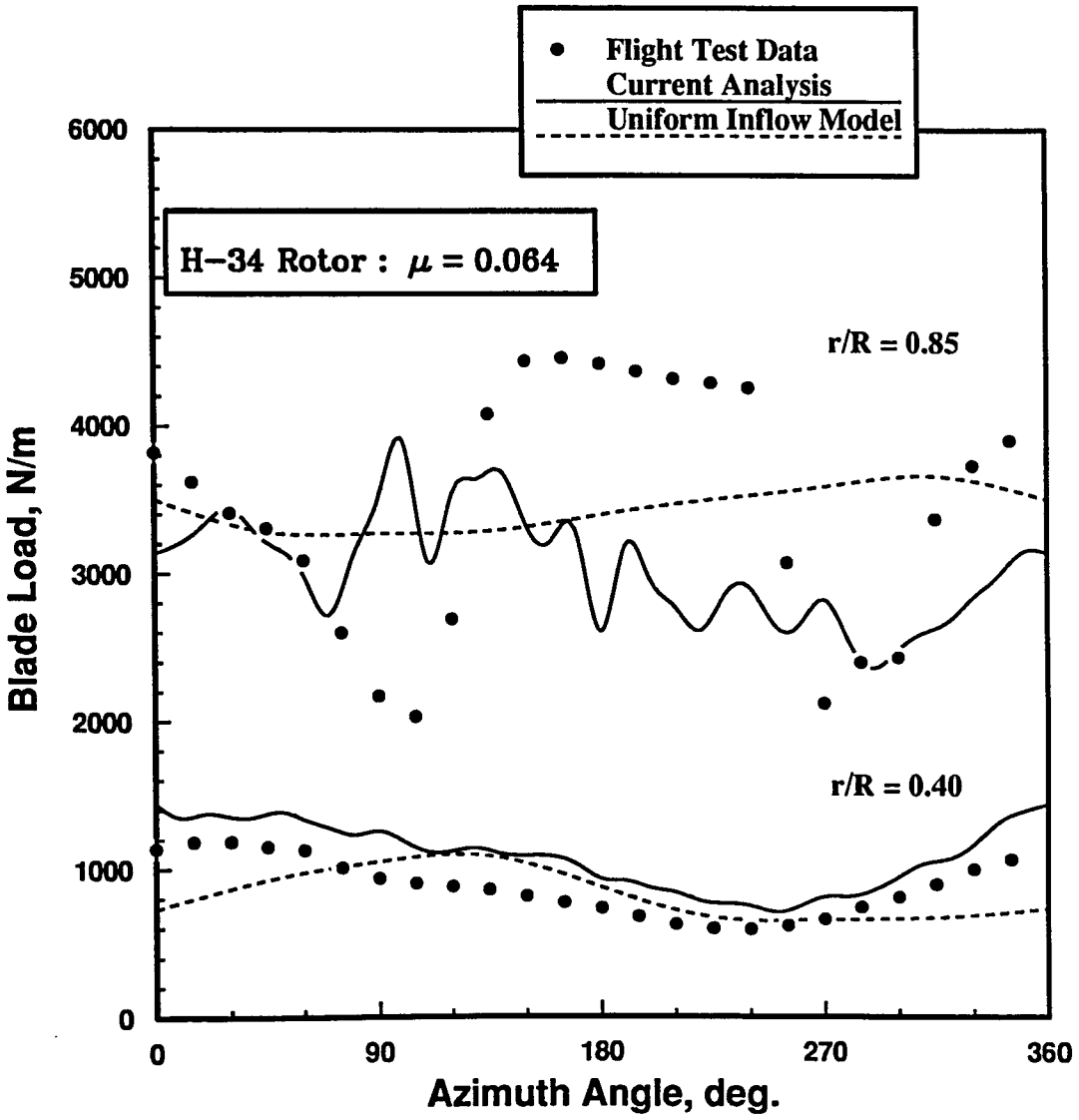

Figure 4.8: Blade load at r/R =0.40 and 0.85 for μ =0.064

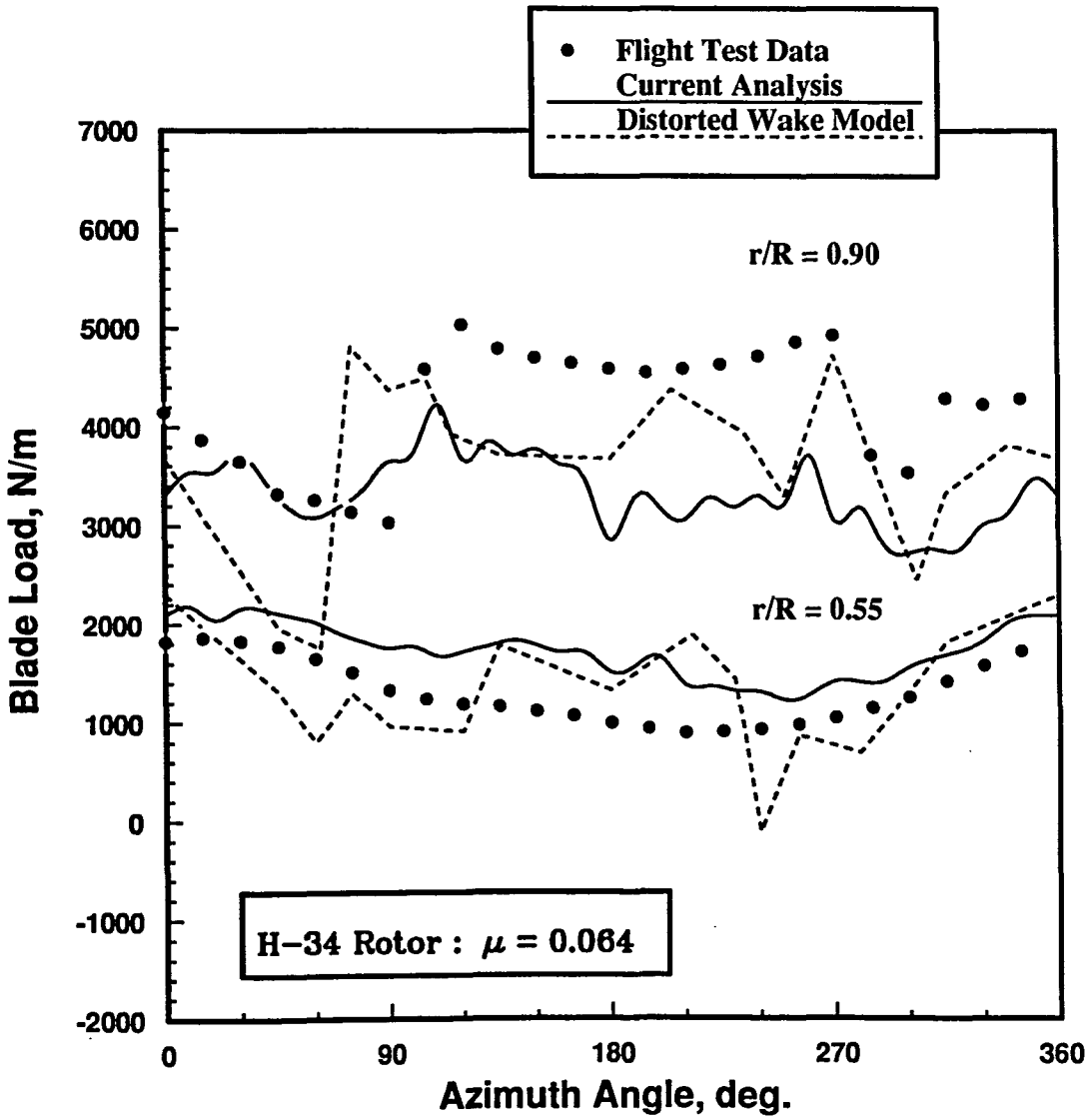

Figure 4.9: Blade load at r/R =0.55 and 0.90 for μ =0.064

Rotor/Airframe Interaction in Forward Flight

Test Case and Configuration

A model consisting of a cylindrical body with a hemispherical nose and two-bladed teetering rotor has been chosen for the calculation of rotor/airframe interaction problem. The use of a simple geometric airframe model results in less complicated interactions and yet reveals the major characteristics of the aerodynamic interference. This model has been extensively tested in the Georgia Institute of Technology 2.13×2.74 meter wind tunnel ([6–12],[14]).

The airframe model is a cylinder of 134 mm in diameter with a hemispherical nose. The teetering rotor has a radius of 0.45 m and consists of two untwisted NACA 0015 blades. Figure 4.10 describes the rotor/airframe geometry, and Table 4.5 lists the important geometric characteristics of the configuration. The rotor blades are set at 10 degrees fixed pitch and have no cyclic pitch variations; but they are permitted to flap. Table 4.6 contains the flapping harmonic coefficients deduced from the data presented in Reference [10]. The computations are carried out for an advance ratio of 0.1 at a constant rotor speed of 2100 RPM. Three runs of isolated airframe, isolated rotor and rotor/airframe are performed with the same flight conditions as listed in Table 4.7.

All of the three calculations are conducted on the same ($77 \times 59 \times 80$) grid over a cylindrical domain with a size of 40 rotor diameters in diameter and 70 rotor diameters in height. The grid is arranged to have a very high density near the surface of the airframe to resolve the viscous boundary layer, and a relatively high density in the neighborhood of the rotor disc to capture the complex vortical flow.

Table 4.5: Rotor/airframe geometric characteristics

Rotor radius	0.4570 m
Chord	0.0860 m
Hub radius	0.0125 m
Hinge offset	0.0000 m
Number of Blades	2
Twist	0.00 deg.
Collective pitch	10.0 deg.
Airfoil type	NACA 0015
Airframe length	1.350 m
Airframe diameter	0.134 m
Rotor/airframe clearance*	0.135 m

* measured from rotor center to airframe surface

Table 4.6: Blade flapping harmonics for rotor/airframe configuration

n	a_n	b_n
0	0.0000	0.0000
1	-1.9400	-2.0300

Table 4.7: Forward flight test conditions for rotor/airframe configuration

μ	0.100
V_∞, m/s	9.895
V_{tip}, m/s	98.95
ω, RPM	2100
ρ, kg/m^3	1.2766
$\alpha_{s_{long}}$, deg.	-6.0
$\alpha_{s_{lat}}$, deg.	0.0
$\alpha_{TPP_{long}}$, deg.	-4.06
$\alpha_{TPP_{lat}}$, deg.	2.03
Reference	[9], Table 2

Computations for the isolated rotor and isolated airframe are started with an initial guess of free-stream flow everywhere in the domain, while the converged flow field solution from the isolated airframe case is used to start the rotor/airframe problem. It is found that for the rotor/airframe configuration a converged solution is achieved after 1000 iterations in roughly about 12 hours of CPU time on the CRAY-2S. For the first 200 iterations a constant low under–relaxation was used (about 0.02), which was later gradually increased to 0.32.

Surface Pressure and Skin Friction Coefficient Predictions

The pressure coefficient (C_p) distribution over the airframe model in the absence of the rotor is compared to experimental result as shown in Figure 4.11. The agreement between the theoretical and experimental prediction is excellent over most of the body surface except for slight discrepancies near the nose region. However, it must be borne in mind that the modelling of the nose portion of the airframe is very

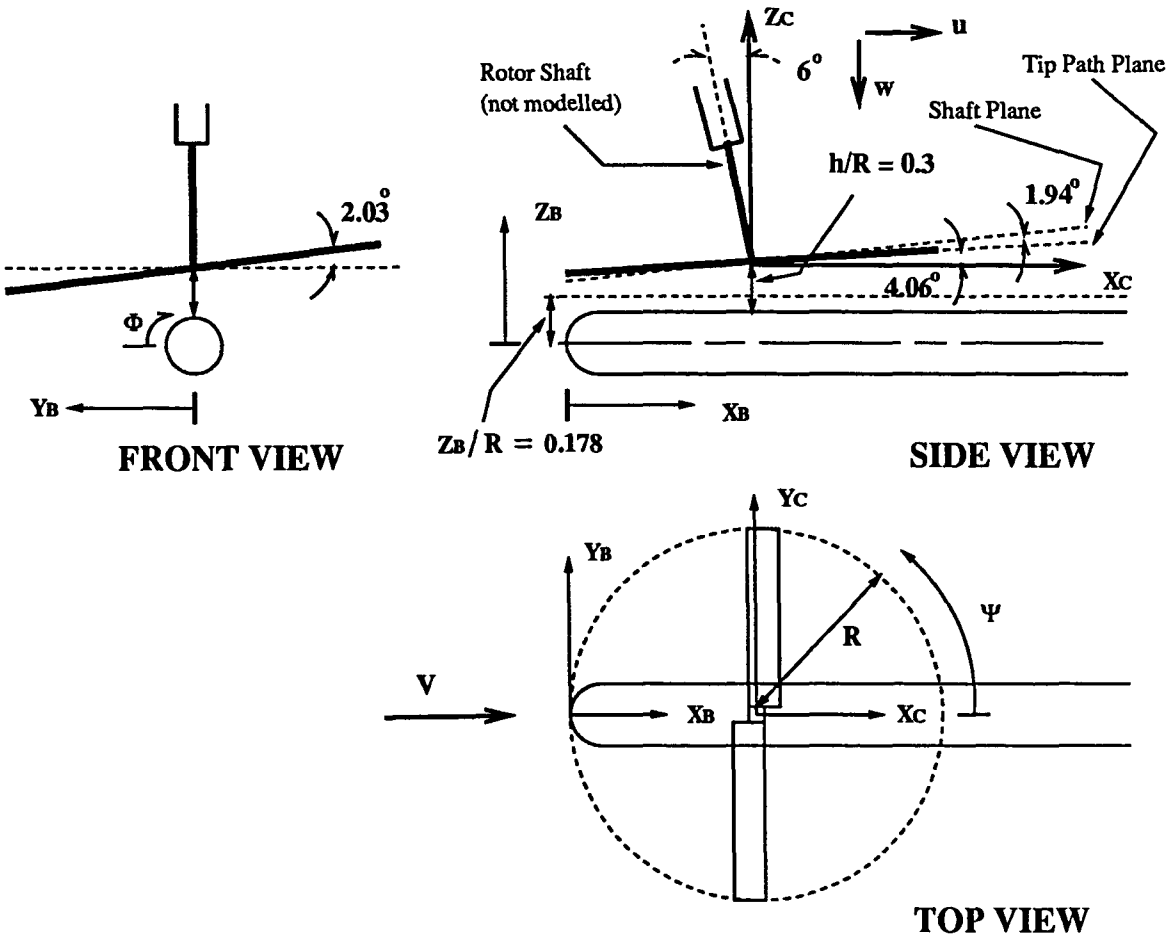

Figure 4.10: Rotor/airframe schematic details

rough since a body–fitted grid is not used at this location. A pressure decrease in experimental result in the vicinity of $X_B/R = 1.0$ (hub region) can also be observed in the figure. This is due to flow acceleration around the hub. The hub is not modelled in the current analysis and therefore the agreement with experimental result in this region is not anticipated.

The rotor's influence on the airframe surface pressure distribution is profound and is clearly demonstrated in Figures 4.12 through 4.15. In the first figure, the altered pressure distribution along the top of the airframe ($\Phi = 90°$) obtained from the current analysis is compared to experimental results and to two other theoretical predictions by Lorber [13] and Mavris [14]. The experimental data are measures of mean surface pressure made by digitizing and averaging the analog signals from a pressure transducer over a time interval corresponding to 140 rotor revolutions (more details on the data acquisition are given in [9]). The untwisted and non-tapered rotor blades cause the blade loading to shift outboard resulting in the generation of a strong tip vortex and severe rotor–wake/airframe interference near the edges of the wake. The two peaks of positive pressure shown in Figure 4.12, near $X_B/R = 0.5$ and $X_B/R = 2.0$, correspond to this rotor–wake/airframe interaction and since there is addition of energy by the rotor inside the wake the C_p distribution takes on values greater than unity (C_p, used herein, is defined as $C_p = (p_{surf} - p_\infty)/q_\infty$). The first peak due to wake leading edge impingement is not captured by the current procedure, while the second peak and the nose stagnation pressure are captured remarkably well. The reason for this is not immediately clear. One possible cause is the close proximity of the rotor blade tip to the nose of the airframe, which results in a stronger rotor–wake/airframe interaction near the leading edge, where the current grid resolution

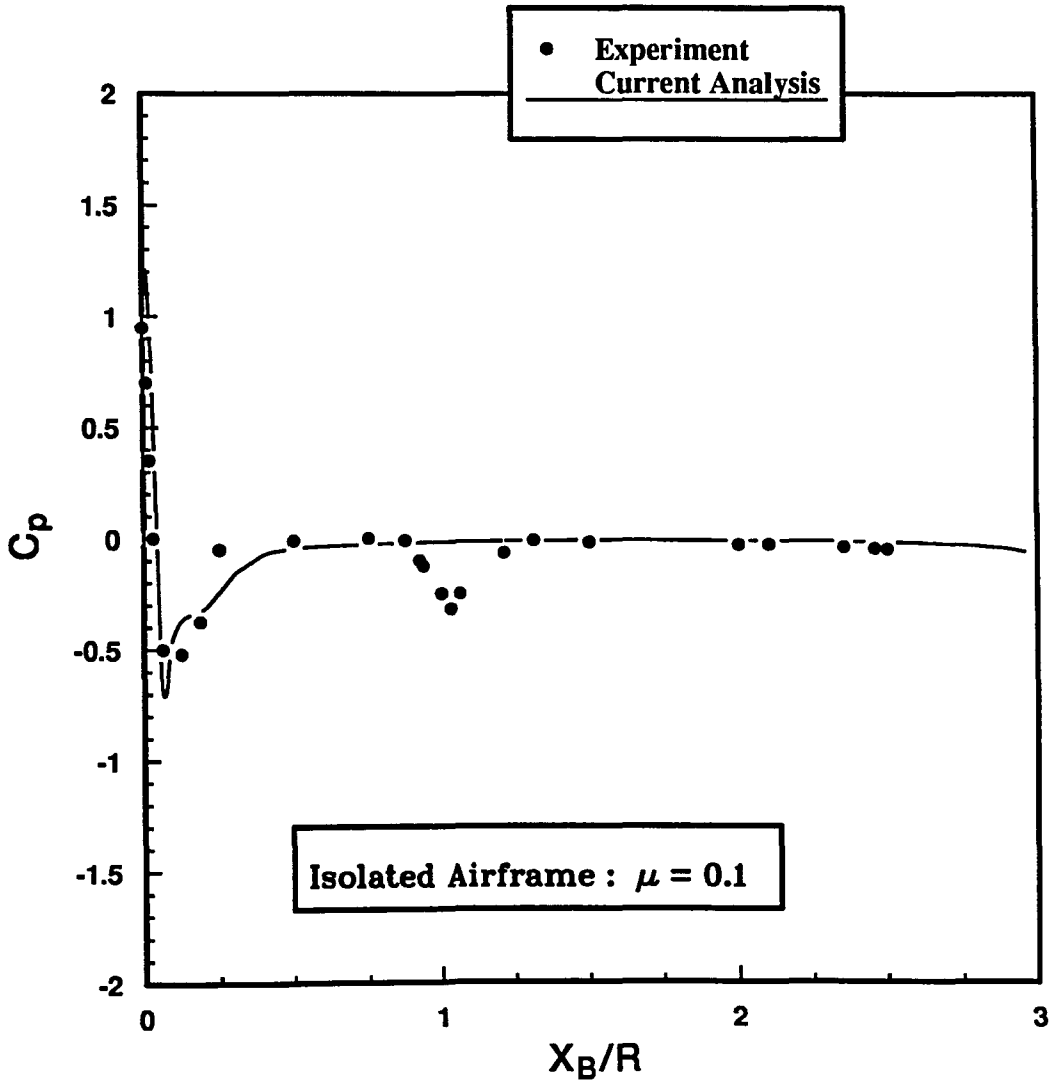

Figure 4.11: C_p distribution on the top of an isolated airframe at condition of μ =0.1

may not be sufficient to capture it. Also, it should be mentioned that the flapping motion is not very well defined in the experiment (it was only deduced from the results presented in Reference [10]) and errors in the flapping motion could be a contributor to the pressure deviation near the nose. The non–body fitted grid near the nose region is another suspect and further work is necessary for a better understanding.

The flowfield in forward flight is characterized by asymmetry. Therefore, the surface pressure distributions for other Φ locations are quite different from the one along the top of the airframe. In Figures 4.13 and 4.14 the predictions at the retreating ($\Phi = 180°$) and the advancing ($\Phi = 0°$) sides, respectively, are presented. The nature of the two curves at these two sections are completely reversed from the previous pressure distribution at $\Phi = 90°$. Here, two suction peaks on each curve, indicated by negative pressure distribution, emerge. This is a direct consequence of rotor–wake leading and trailing edges interfering with the airframe. The impinged flow on the top of the airframe accelerates around the sides of the cylindrical body causing a drop in pressure. The present results correlate well with experimental data along most of the body span with the exception of the leading suction peaks that are not captured in both figures. At the advancing side even though the current results follow the trend in test data, a premature pressure recovery is predicted after the trailing suction peak.

Along the bottom of the airframe ($\Phi = 270°$), the severe rotor–wake interaction is mostly blocked by the airframe itself as seen in Figure 4.15, and the pressure disturbance is minimal. The interference from the edges of the wake can still be seen, but they are swept rearward. Once again, the computational results from the current analysis predict this reduction in aerodynamic interference quite well.

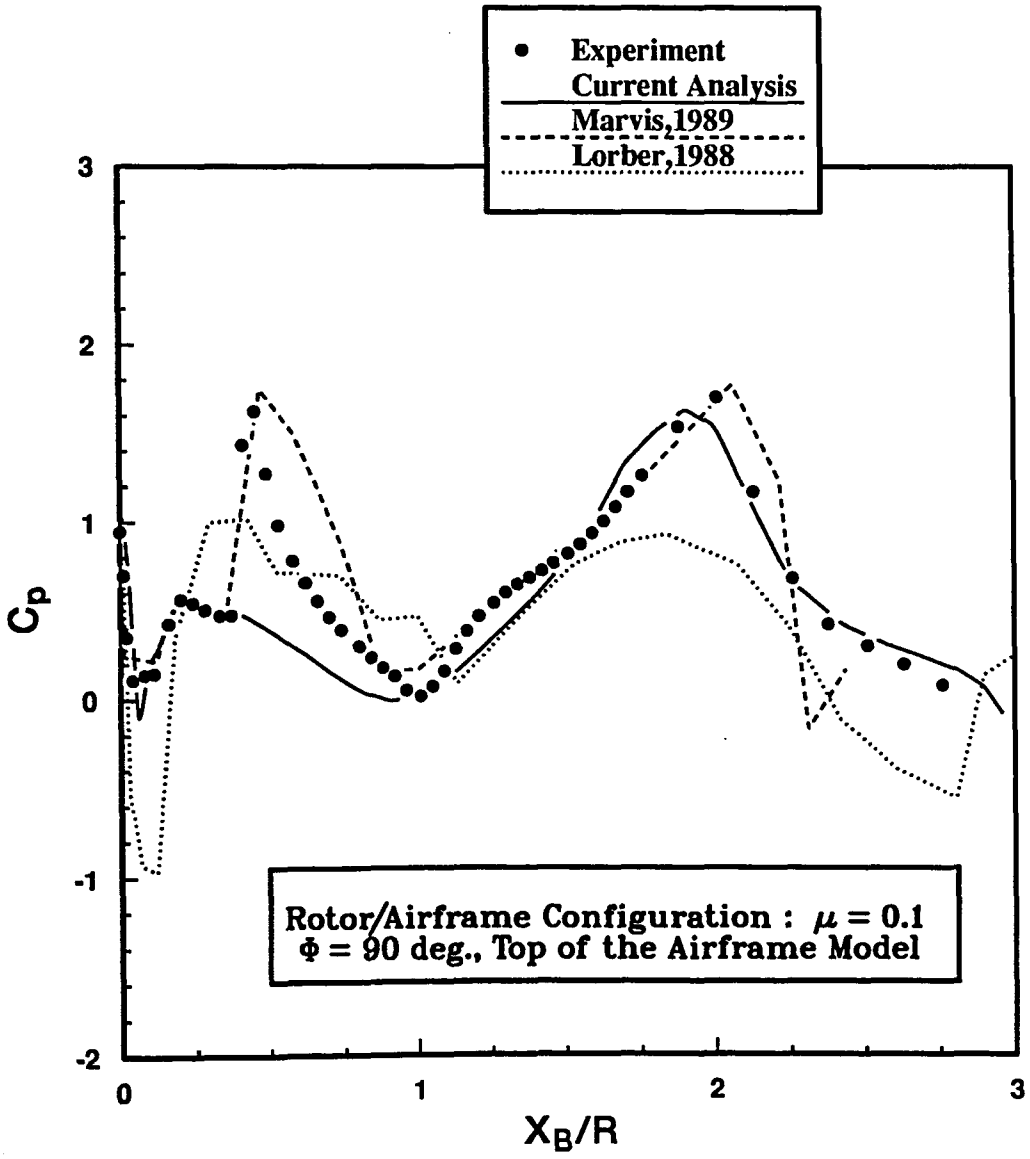

Figure 4.12: Comparison of measured and computed pressure coefficient along the top of the airframe for μ =0.1

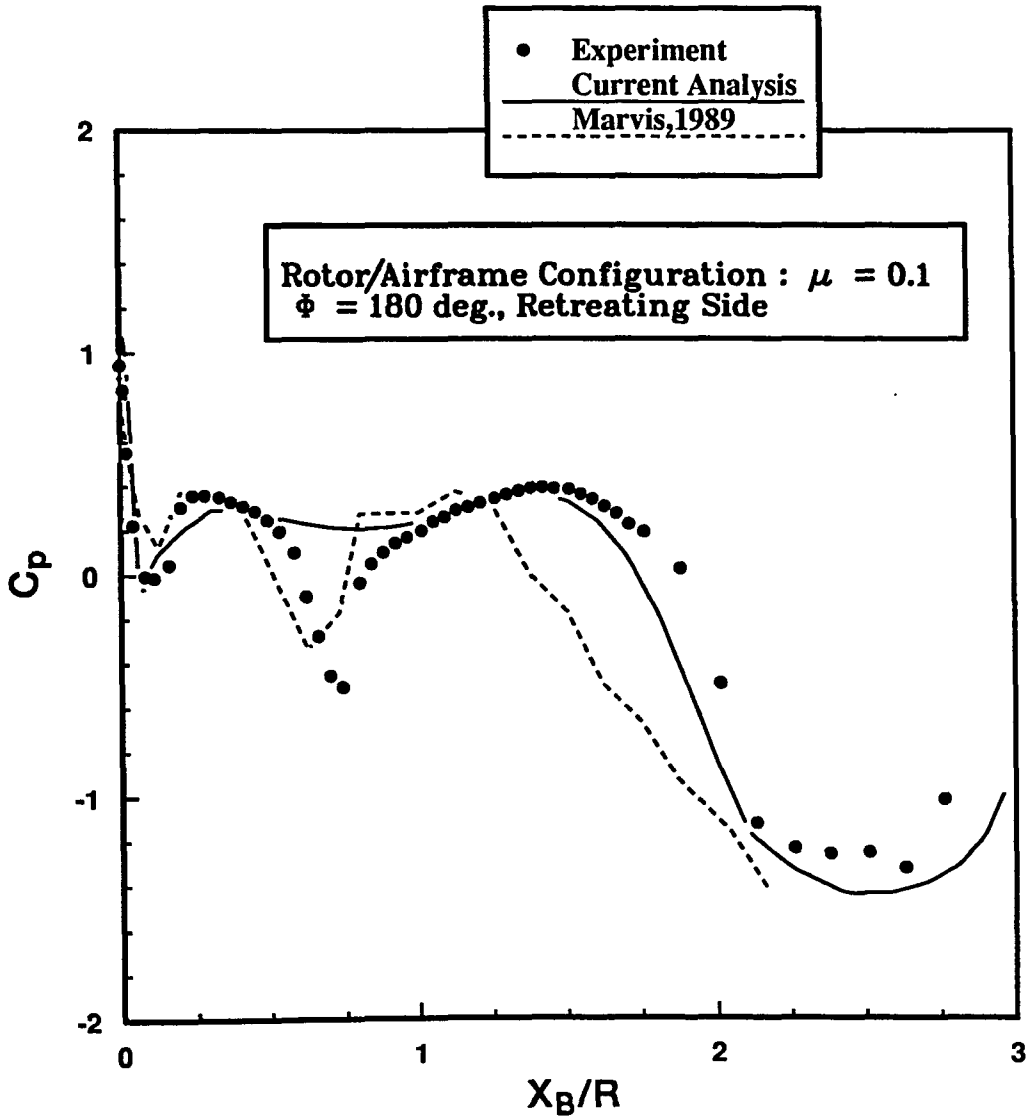

Figure 4.13: Comparison of measured and computed pressure coefficient along the side of the airframe at $\Phi = 180°$ for μ =0.1

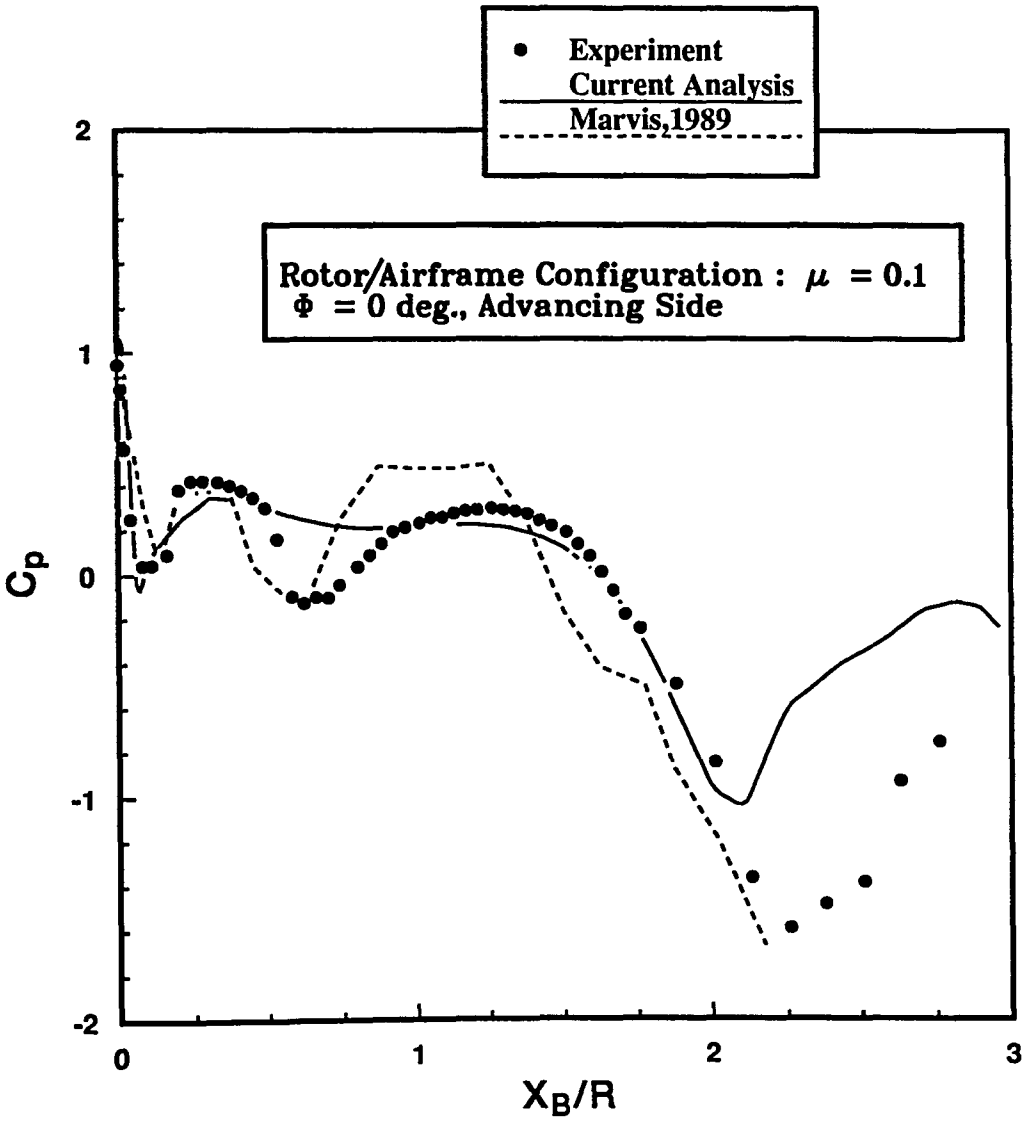

Figure 4.14: Comparison of measured and computed pressure coefficient along the side of the airframe at $\Phi = 0°$ for μ =0.1

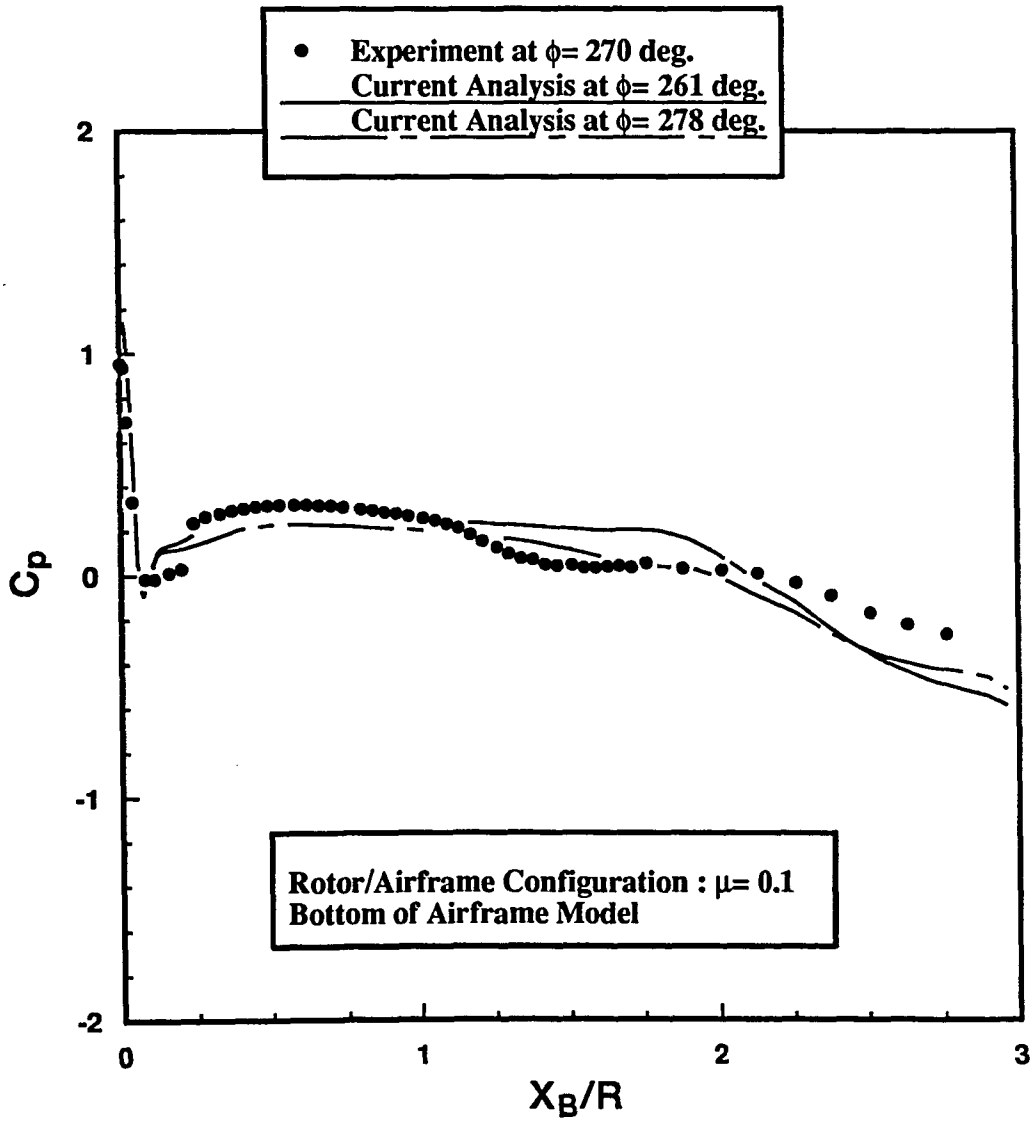

Figure 4.15: Comparison of measured and computed pressure coefficient along the bottom of the airframe at $\Phi = 270°$ for μ =0.1

To present a general view of the variation in pressure on the airframe surface, Figures 4.16.a and 4.16.b display contour plots of the measured and computed C_p distribution respectively. The pressure distribution on the round surface of the cylindrical airframe is unwrapped and projected on a flat surface. The overall characteristics of the theoretical results match extremely well with the measured distribution.

The rotor–wake/airframe interaction is a highly viscous phenomena. The set of Figures 4.17 to 4.21 illustrate the effect of the rotor–wake on the airframe's skin friction coefficient distribution at different Φ locations. The skin friction coefficient (C_f) on the airframe surface for rotor/airframe configuration are compared with the C_f distribution on the surface of isolated airframe case. The C_f values at the nose region are not calculated because of insufficient grid density. In the first figure two peaks can be observed in the rotor/airframe's skin friction coefficient curve. The two peaks are located at the points of the leading and trailing rotor–wake impingements on the surface. Also, an area of negative skin friction coefficient are seen to exist after the nose region for both isolated airframe and rotor/airframe configuration, as an indication of regions of separated flow. However, the reattachment point (where $C_f = 0$) for the rotor/airframe case occurs at a point earlier than the isolated airframe case.

The next three Figures 4.18 to 4.20 clearly show the effect of the aerodynamic interference on the skin friction coefficient distribution. Figure 4.21, is given to present an overview of the C_f distribution on the airframe surface in the presence of the rotor. The ability to predict the airframe skin friction coefficient and the pressure distribution are extremely important, for estimating low speed bluff body drag as their integration on the body surface yields the components of the total drag.

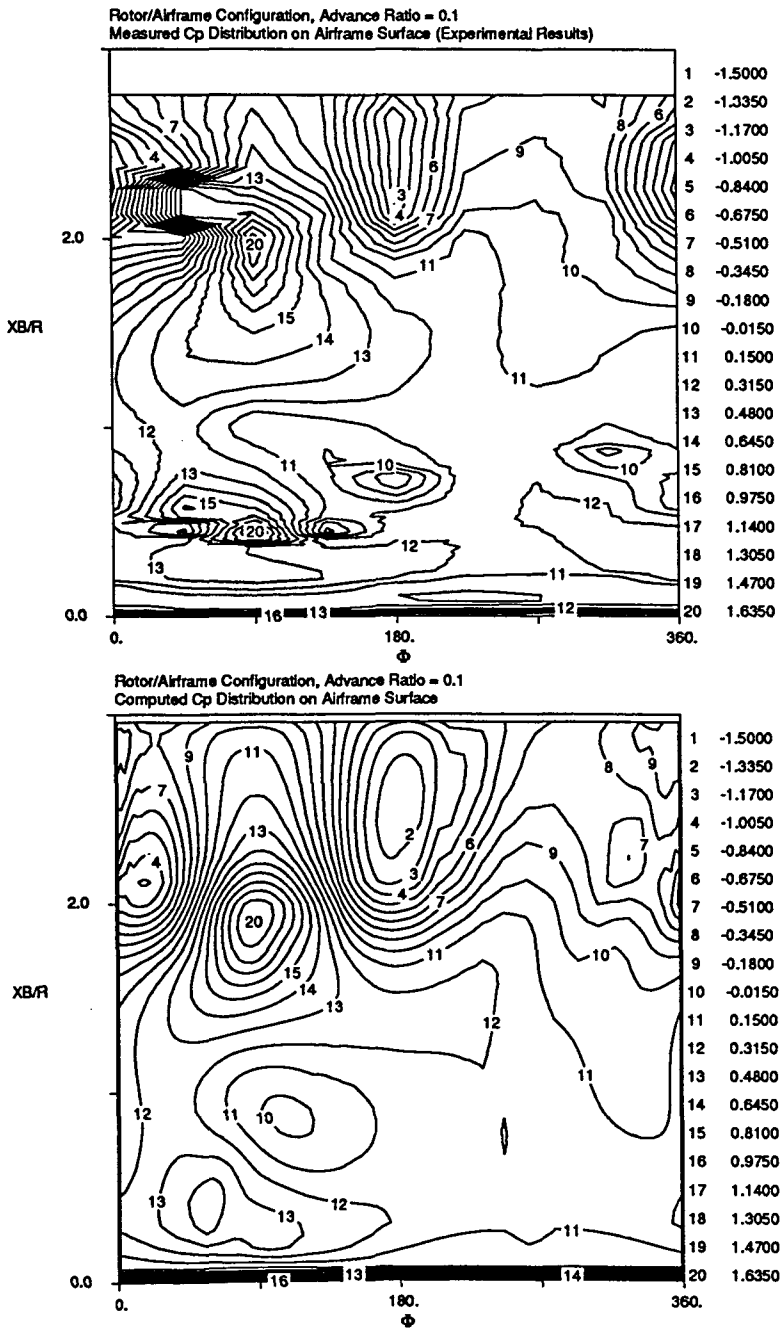

Figure 4.16: Comparison of contour plots for measured and computed pressure distribution around the airframe for μ =0.1

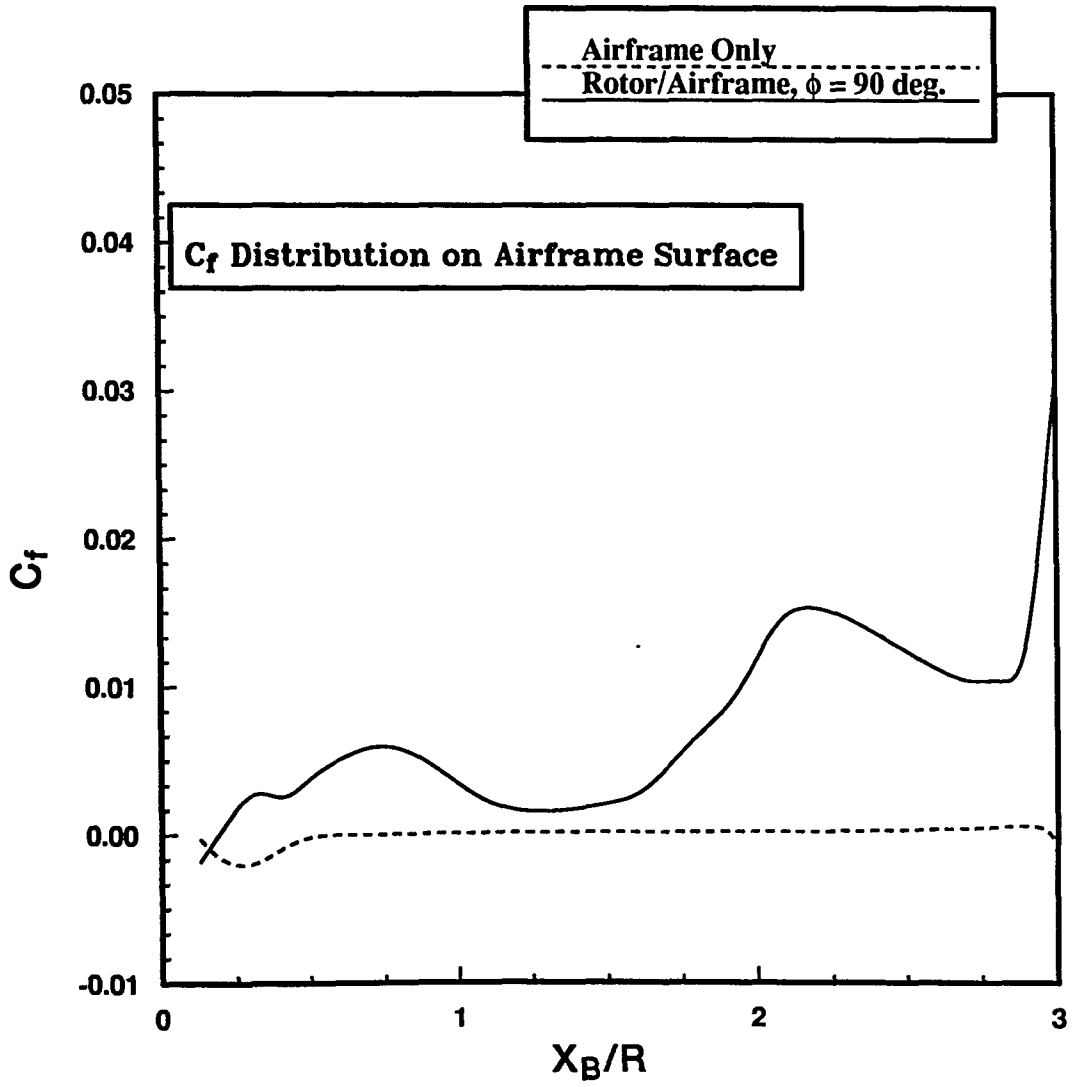

Figure 4.17: Comparison of skin friction coefficient distribution for rotor/airframe and isolated rotor at the top of the airframe, ($\Phi = 90°$)

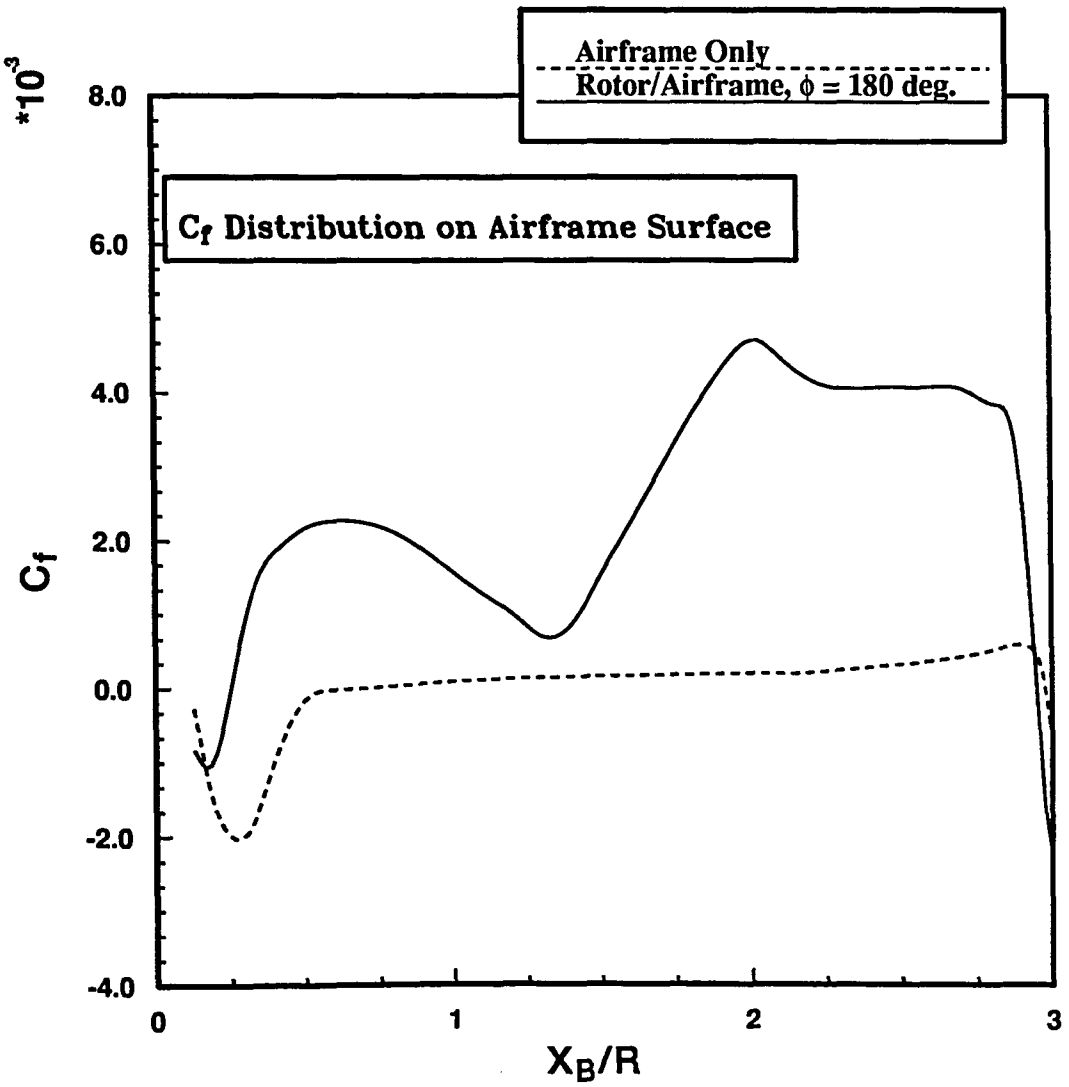

Figure 4.18: Comparison of skin friction coefficient distribution for rotor/airframe and isolated rotor at the retreating side of the airframe, ($\Phi = 180°$)

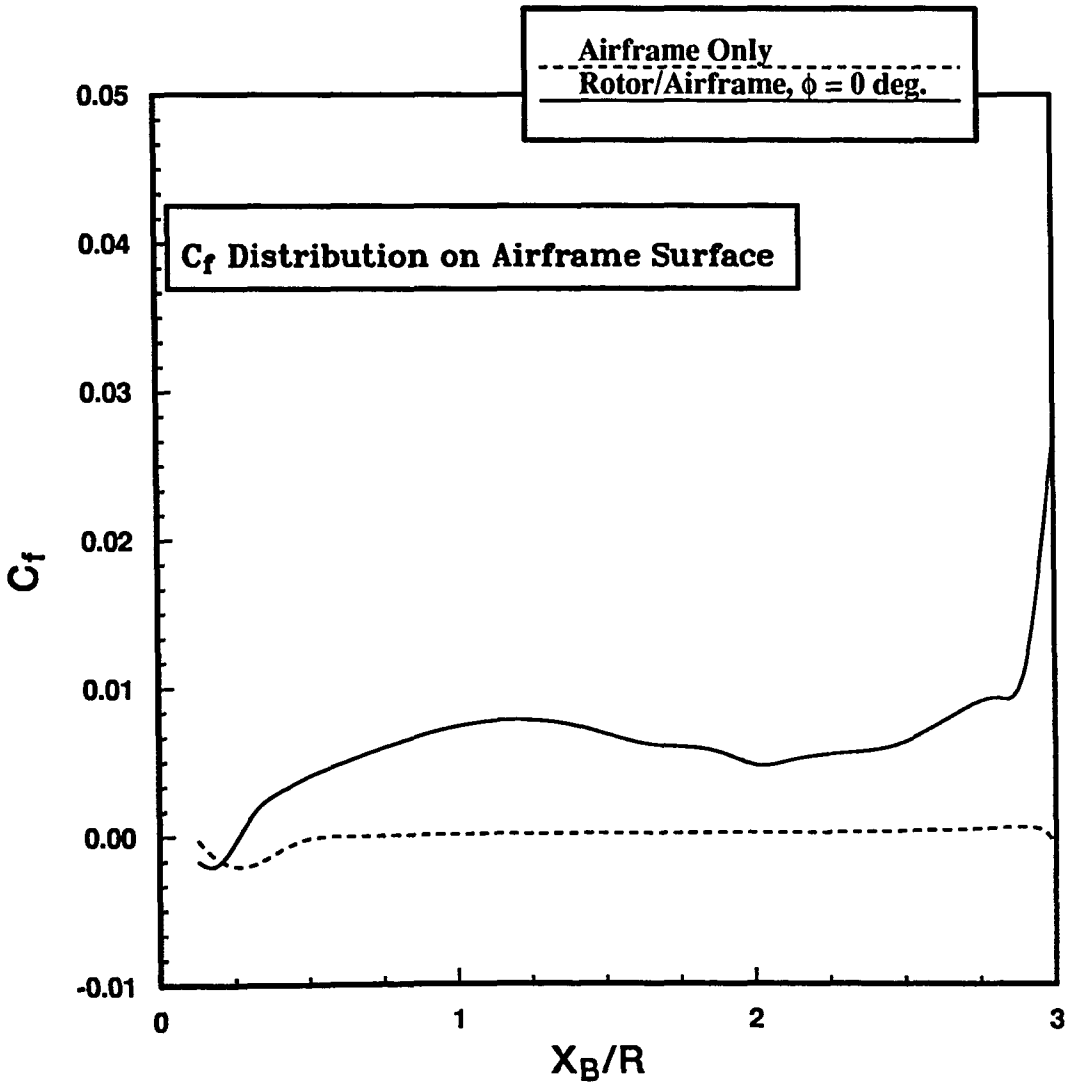

Figure 4.19: Comparison of skin friction coefficient distribution for rotor/airframe and isolated rotor at the advancing side of the airframe, ($\Phi = 0°$)

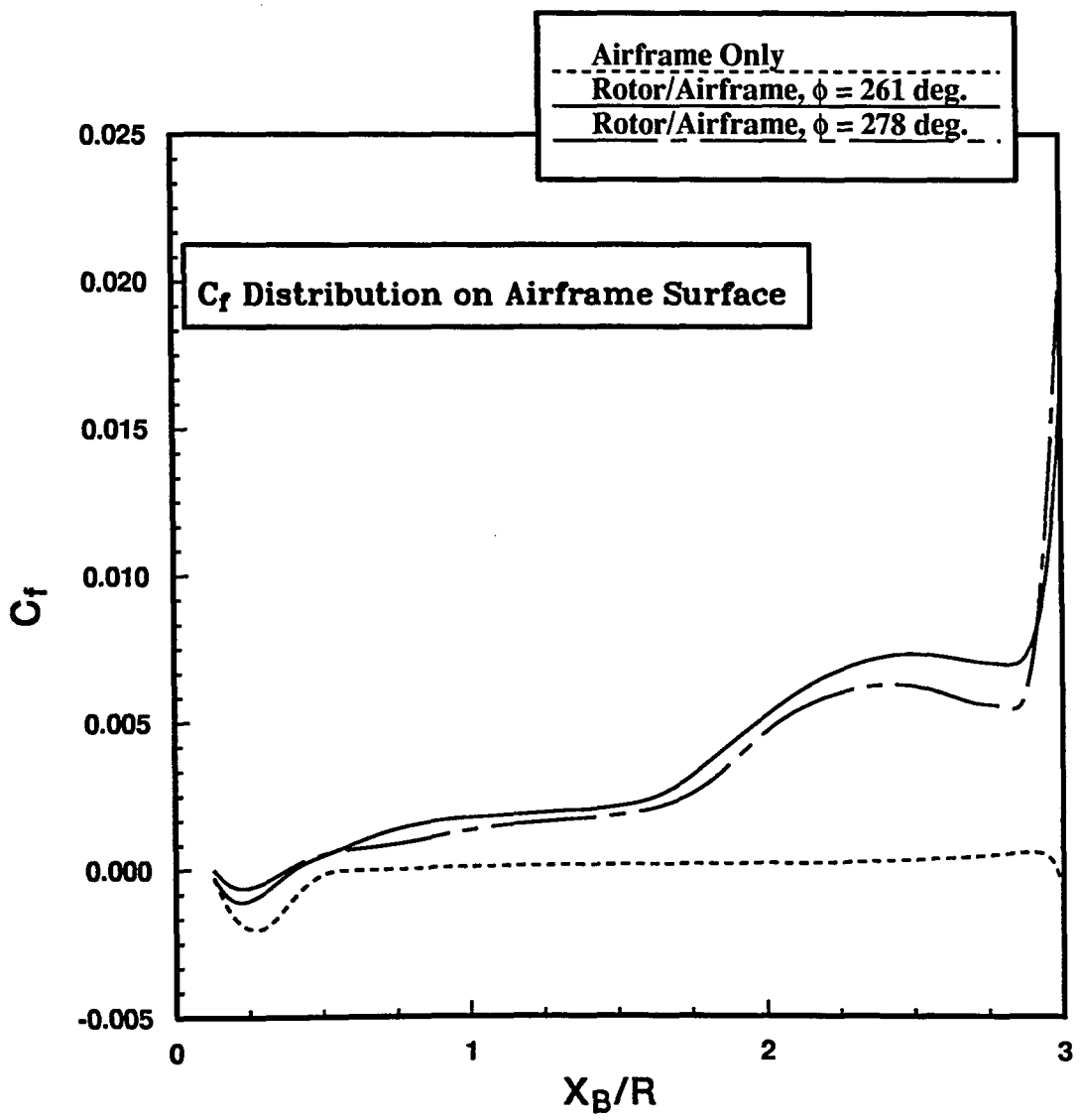

Figure 4.20: Comparison of skin friction coefficient distribution for rotor/airframe and isolated rotor at the bottom of the airframe, ($\Phi = 261°$ and $278°$)

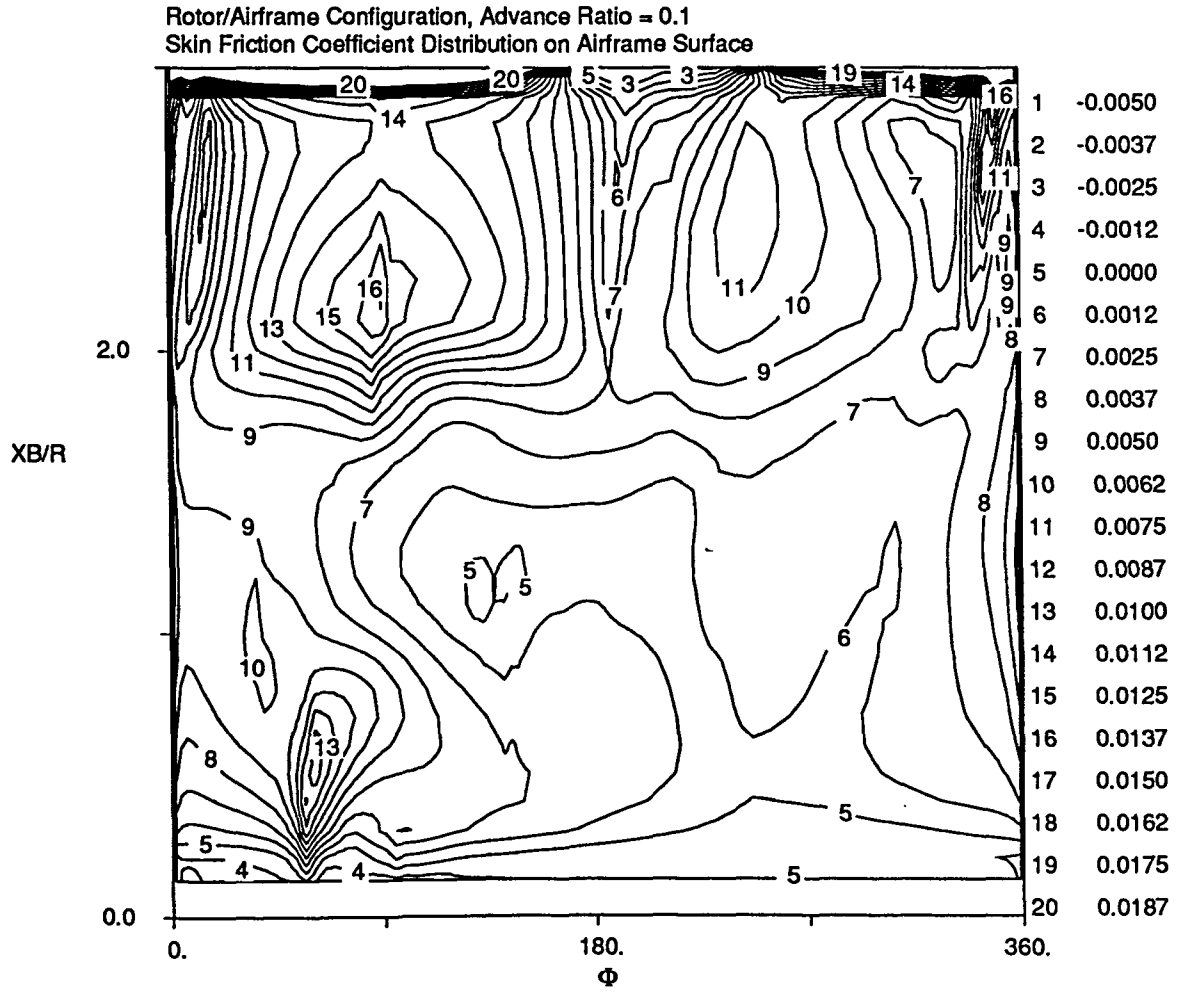

Figure 4.21: Contour plot for the computed skin friction coefficient distribution around the airframe for μ =0.1

Rotor Inflow Velocity Field and Blade Load Distribution

Contour plots of the inflow velocity at a plane 12.7 mm below the rotor disc for isolated rotor and rotor/airframe configuration are shown in Figures 4.22 and 4.23 respectively. The effect of airframe on the inflow velocity is found to be nearly negligible. The airframe redirects the flow causing a slight increase in upwash velocity (negative values) at the outermost region of the rotor in the vicinity of $\psi = 180°$.

The increase in upward velocity, in turn, is translated into higher incident angle of attack seen by the rotor blades and thereby alters the blade load distribution in a narrow band between the azimuth angle range of 160° to 200° , as can be observed in Figures 4.24 and 4.25. These figures also show that the blade load alteration due to the presence of the airframe is minimal and is most noticeable at the outboard region of the rotor disc in the neighborhood of $\psi = 180°$ and also $\psi = 0°$.

The prediction of rotor wake velocity below the rotor disc, along a line located 12.7 mm above the body surface, are compared to measured data from Ref. [11] in Figures 4.26–4.29. Figures 4.26 and 4.27 compare the predicted normalized streamwise velocity component $u/\mathbf{V}_\infty$ with experimental results for an isolated rotor and rotor/airframe configuration respectively. The correlation between the two results is good.

The next two Figures 4.28 and 4.29 present the normalized downward velocity components, $w/\mathbf{V}_\infty$. The results clearly show the upwash (negative values) near the vicinity of the nose of the airframe. Again, the first peak in $w/\mathbf{V}_\infty$ near $X_B/R = 0.5$ for the isolated rotor and the rotor/airframe configurations are under-predicted in the present analysis.

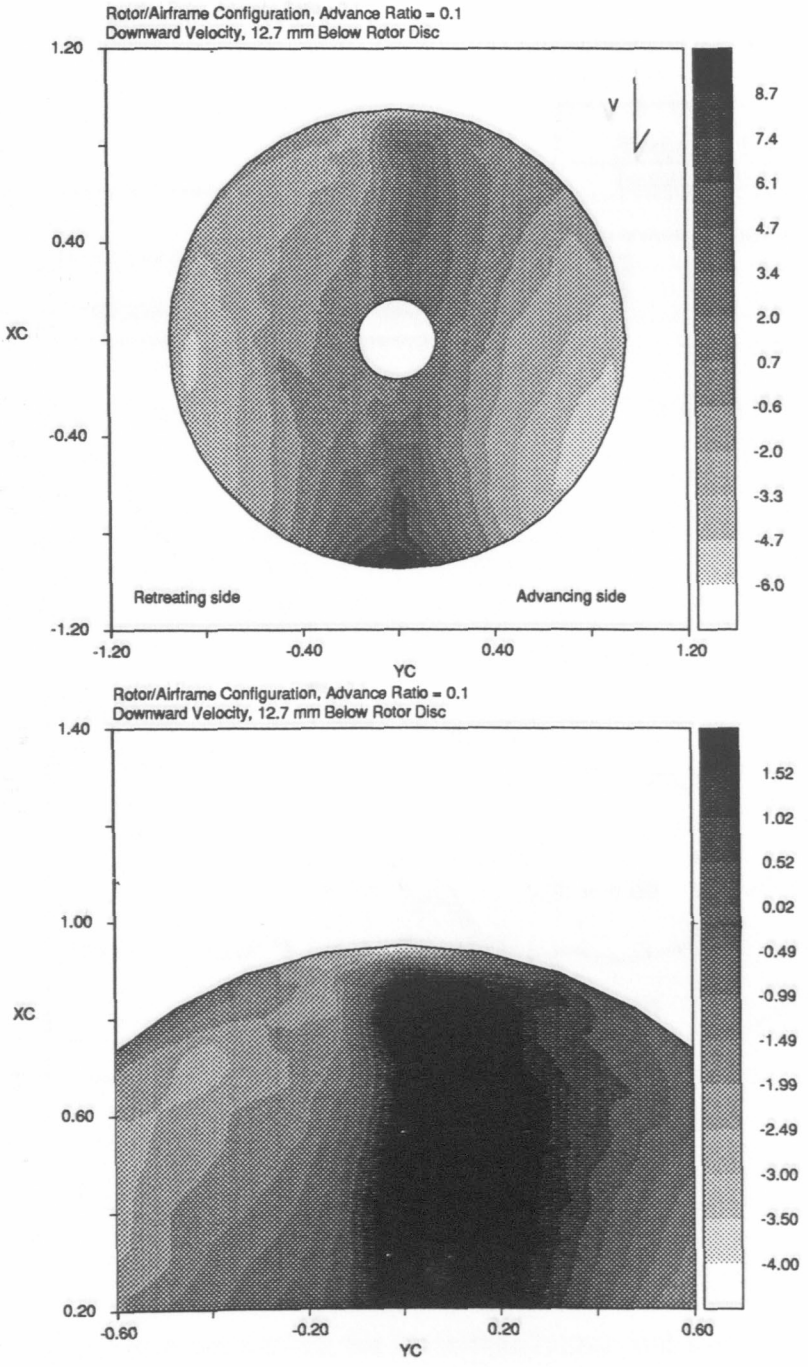

Figure 4.22: Contour plot of the predicted induced flow for a rotor/airframe configuration calculated 12.7 mm below the rotor disc at μ =0.1

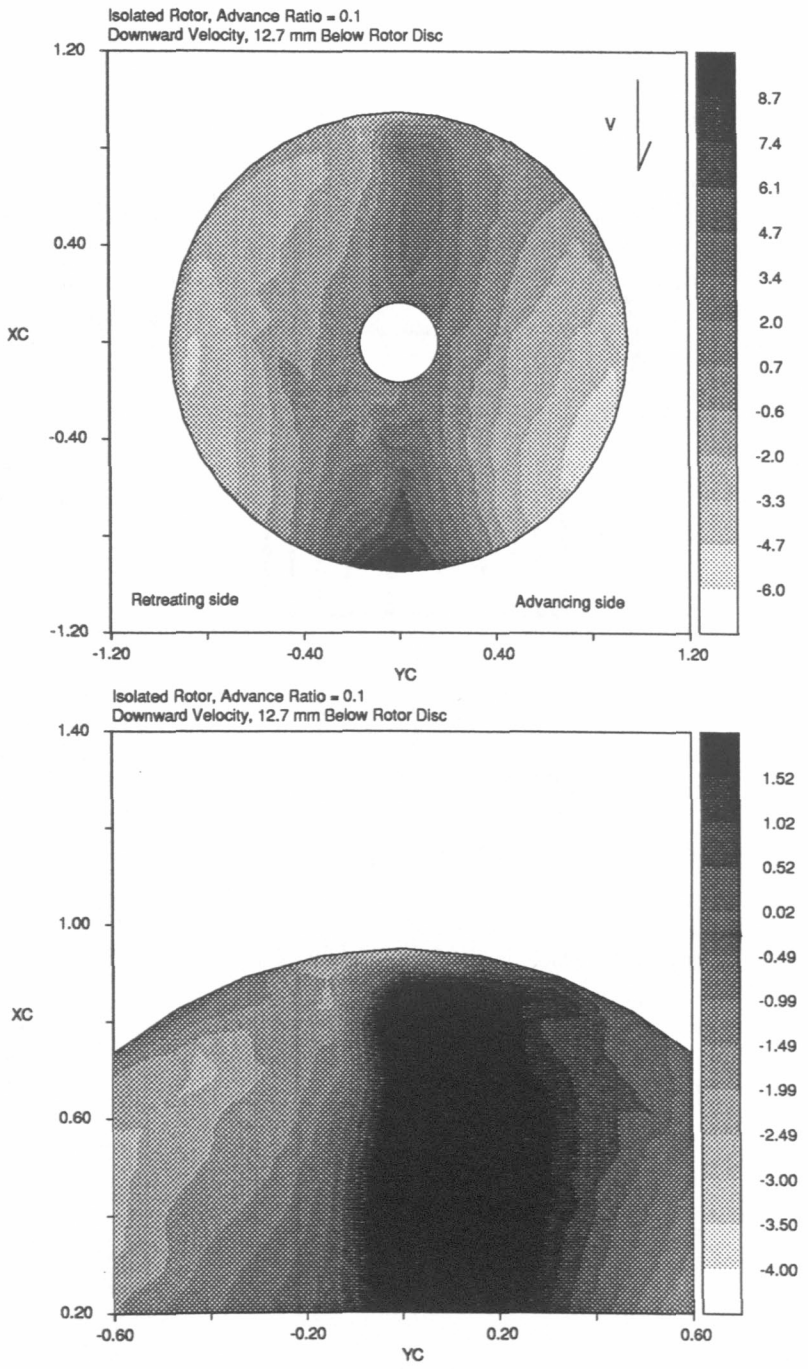

Figure 4.23: Contour plot of the predicted induced flow for an isolated rotor calculated 12.7 mm below the rotor disc at μ =0.1

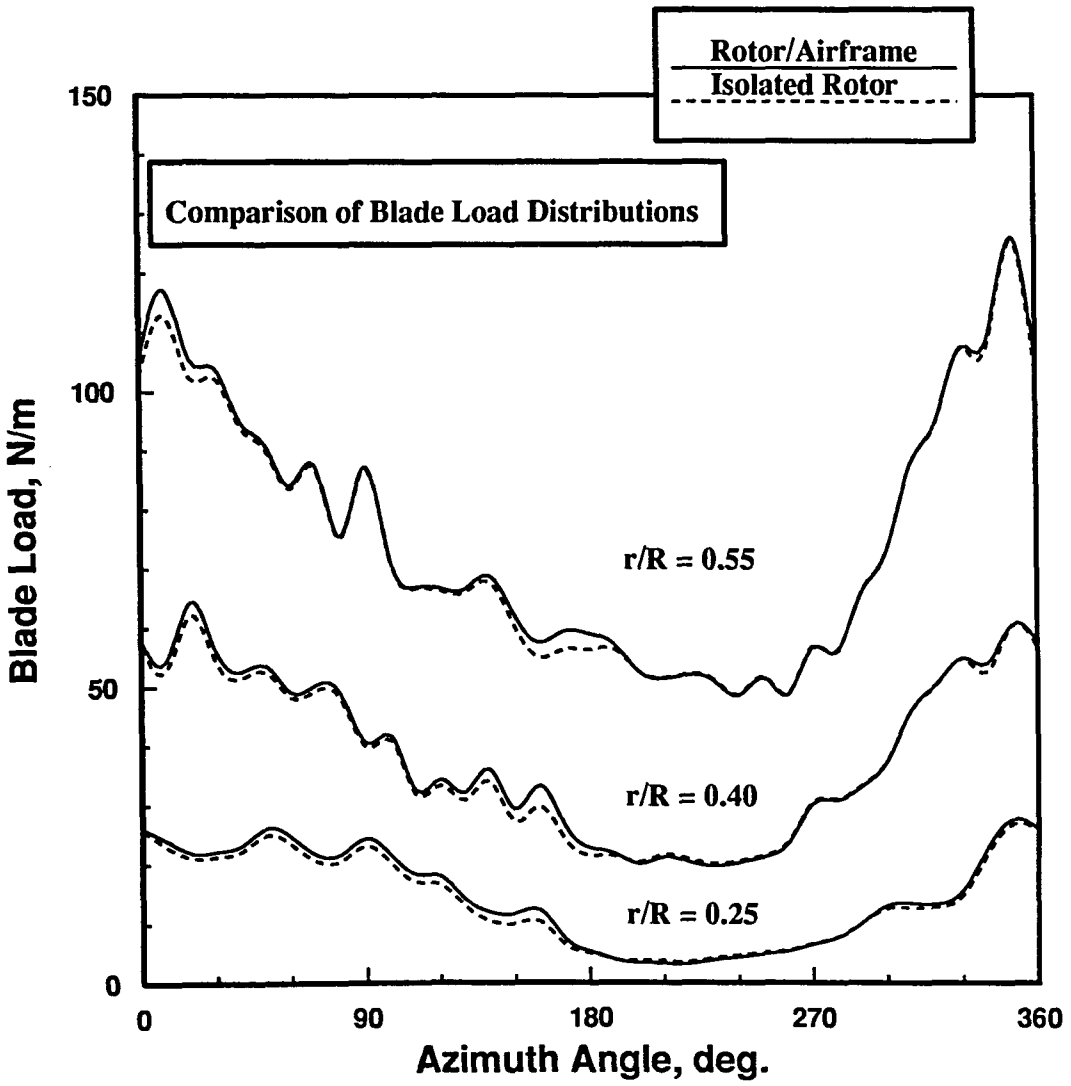

Figure 4.24: Blade load comparison for an isolated rotor and rotor/airframe configuration at r/R =0.25, 0.4 and 0.55 for μ =0.1

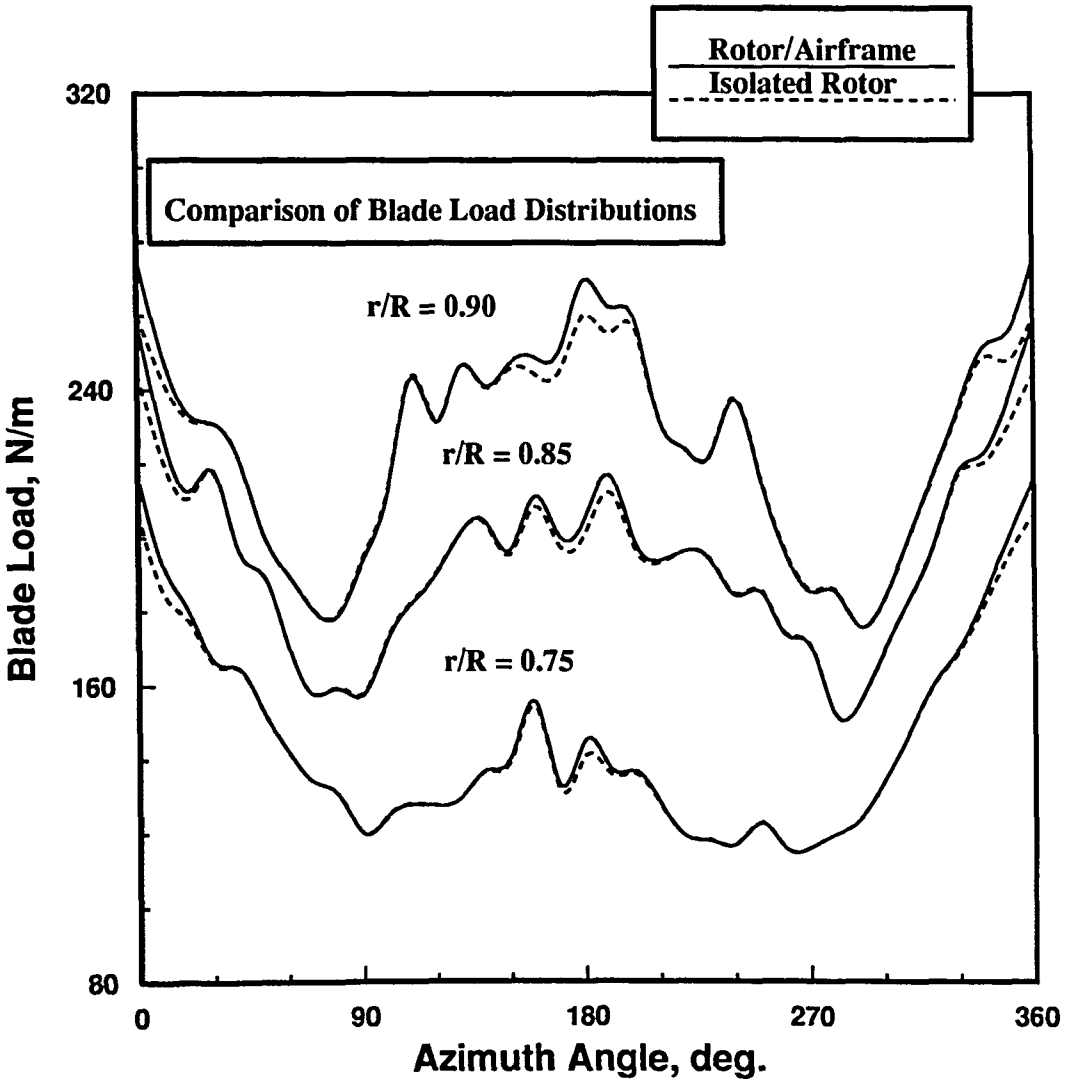

Figure 4.25: Blade load comparison for an isolated rotor and rotor/airframe configuration at r/R =0.75, 0.85 and 0.90 for μ =0.1

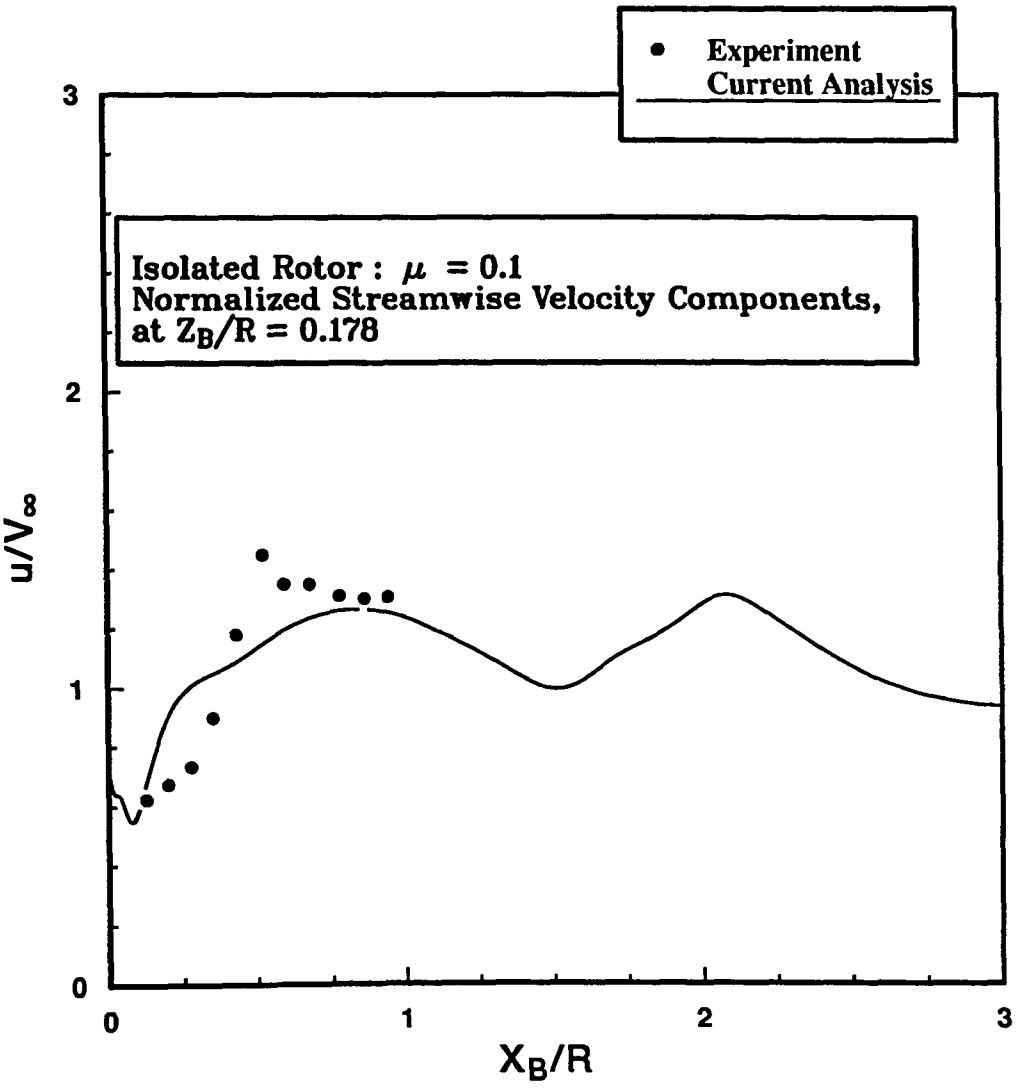

Figure 4.26: Comparison of measured and computed normalized streamwise velocity components, u/V_∞, for isolated rotor at Z_B/R =0.178

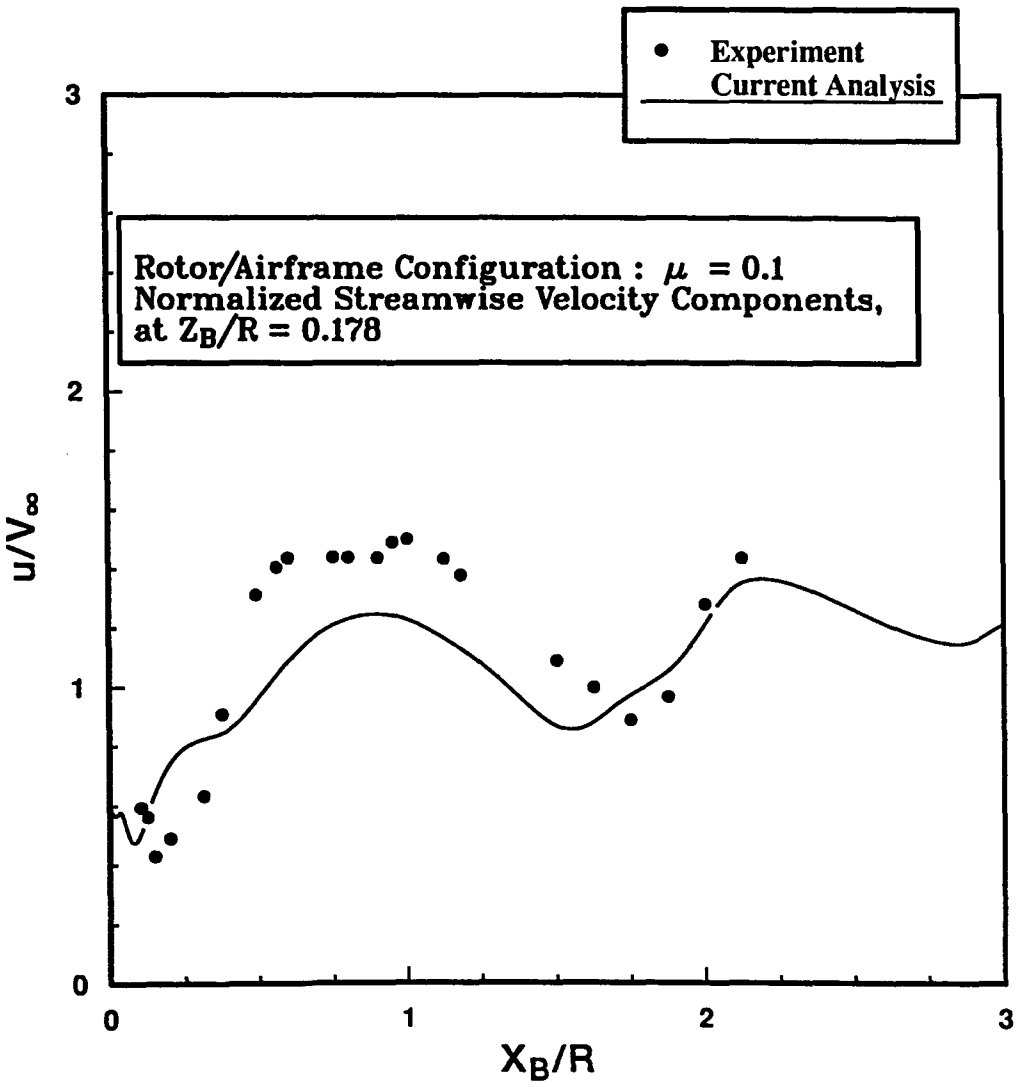

Figure 4.27: Comparison of measured and computed normalized streamwise velocity components, u/V_∞, for rotor/airframe configuration at Z_B/R =0.178

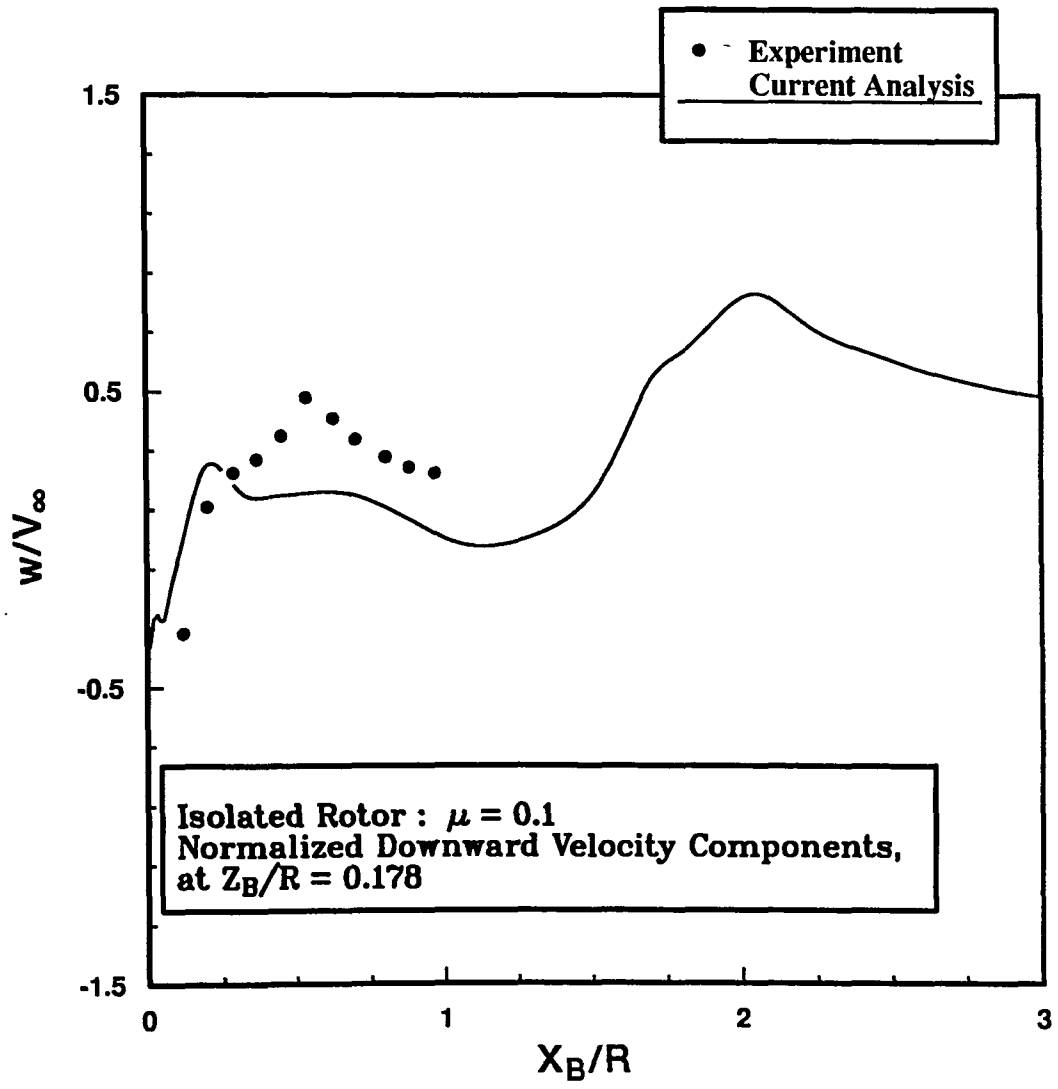

Figure 4.28: Comparison of measured and computed normalized downward velocity components, w/V_∞, for isolated rotor at Z_B/R =0.178

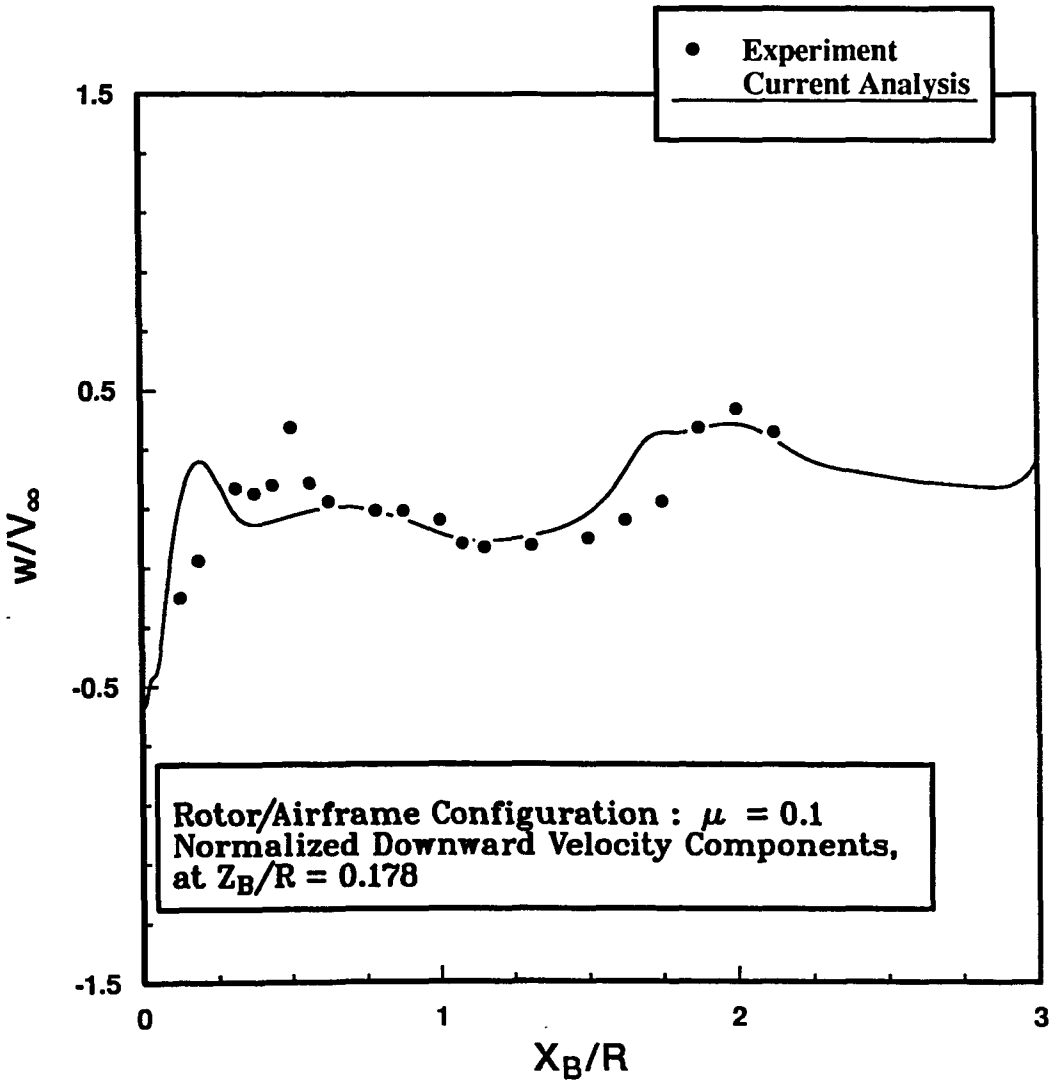

Figure 4.29: Comparison of measured and computed normalized downward velocity components, w/V_∞, for rotor/airframe configuration at Z_B/R =0.178

General Flowfield Predictions

An important feature of the current method is its ability to predict not only the blade load distributions but also the complex flow field in the vicinity of the rotor as well as far from it. Since there are no experimental data bases available for comparison with the flowfield predictions, only computational results are presented. Therefore, physical intuition and qualitative comparison must be adapted in evaluating the flow field results.

The first set of figures (4.30-4.33) are vector plots of the cross–flow velocities. The plots are viewed from planes normal to the freestream flow and from behind the rotor/airframe configuration. These figures trace the development of the strong shed vortices from the tip of the rotor. The vectors in these figures are scaled to show the magnitude of velocity. The plots indicate that as the two tip vortices move downstream they gradually diffuse as well as descend downward. This downward movement of the two vortices is related to the wake rate of convection. Figure 4.34 displays a side view of the flowfield. At this low advance ratio ($\mu = 0.1$) the wake can be clearly seen to convect in the streamwise and the downward directions. A closer view of the flow field around the airframe, given in Figure 4.35, reveals the complex and highly viscous flow over the body surface. A separation bubble exists at the top, near the nose of the airframe.

Contour plots of pressure at locations similar to those in Figures 4.30-4.33 are presented in Figures 4.36-4.39. The pressure differential between the top and the bottom surface of the rotor disc in the first two figures is quite obvious. The empty region at the center of the plots is the airframe body, whereas the thick bar on top of it is the rotor. The two tip vortices are depicted by a series of tightly concentrated

closed loop contours. This concentration is seen to weaken downstream (Figures 4.38-4.39), indicating the diffusion of the vortex core.

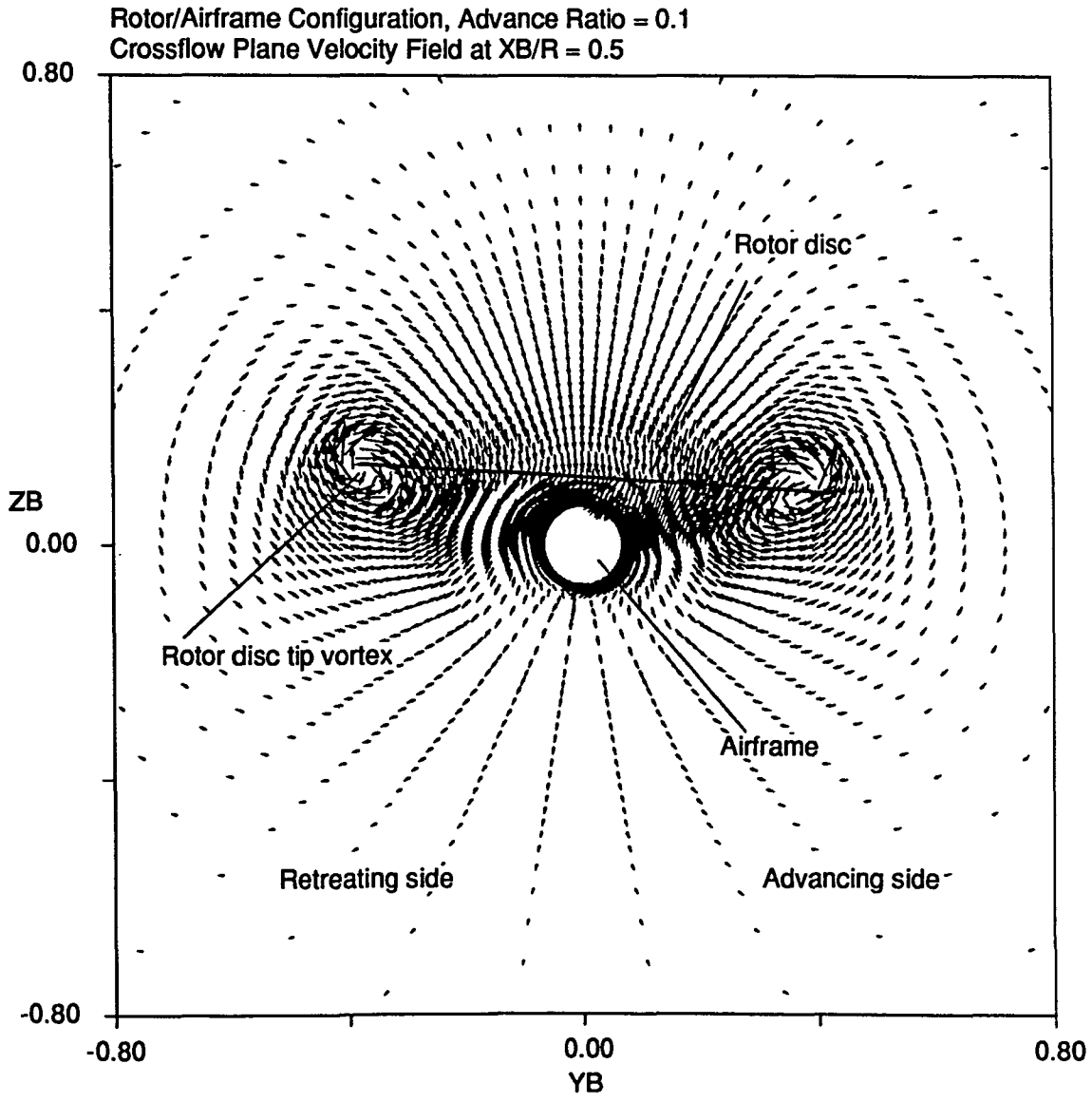

Figure 4.30: Velocity field in the crossflow plane at $X_B/R = 0.5$

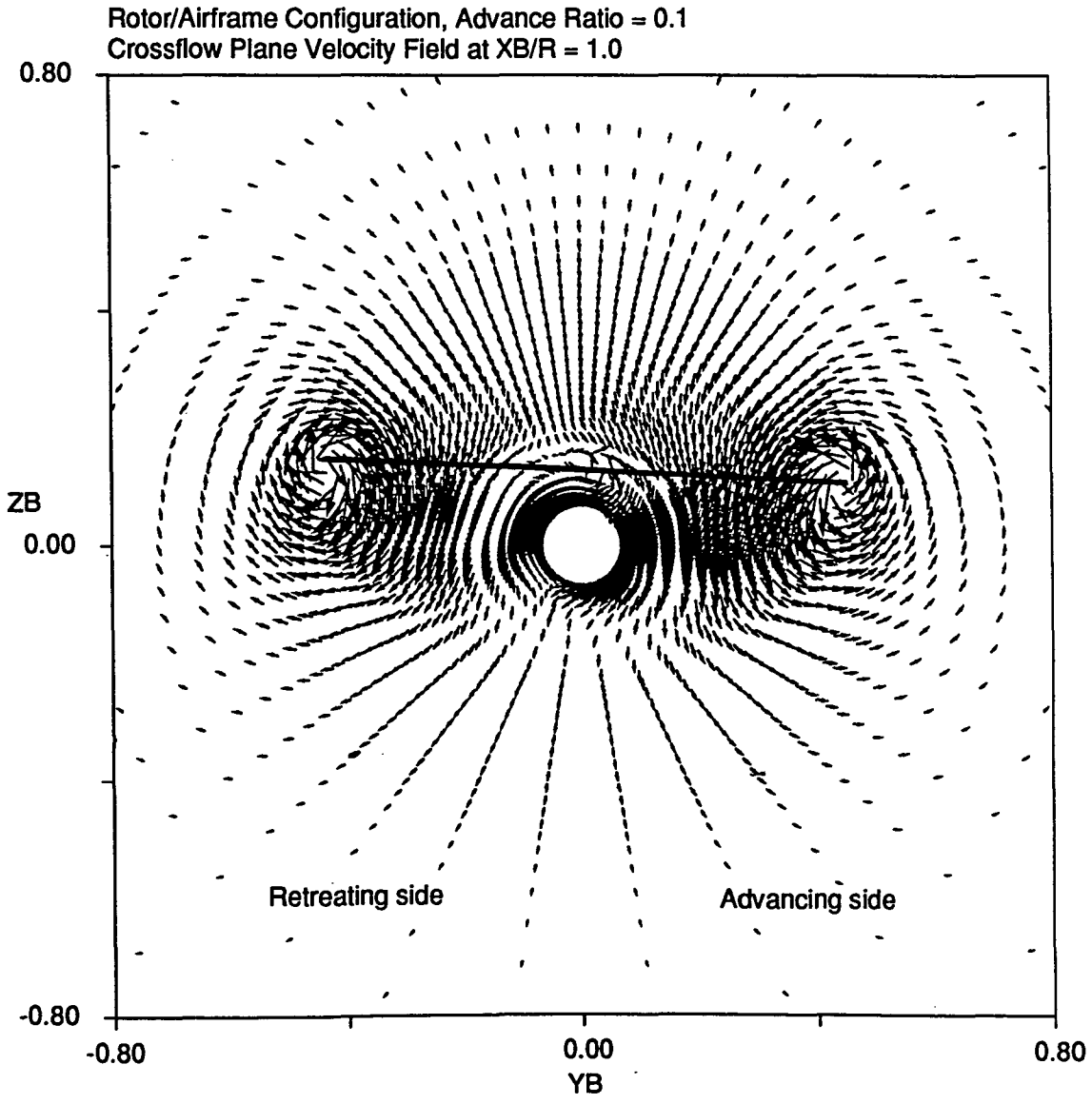

Figure 4.31: Velocity field in the crossflow plane at $X_B/R = 1.0$

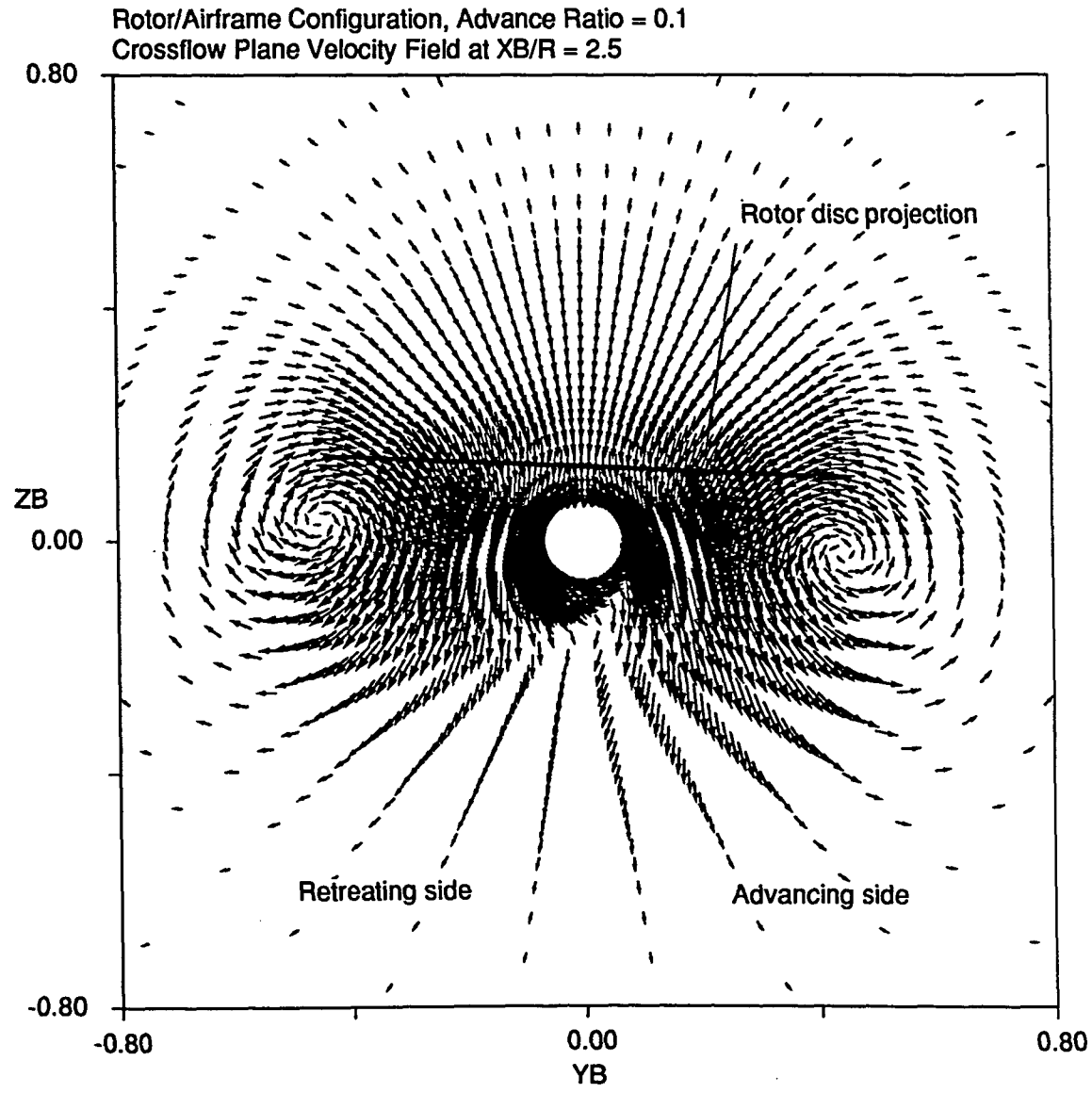

Figure 4.32: Velocity field in the crossflow plane at $X_B/R = 2.5$

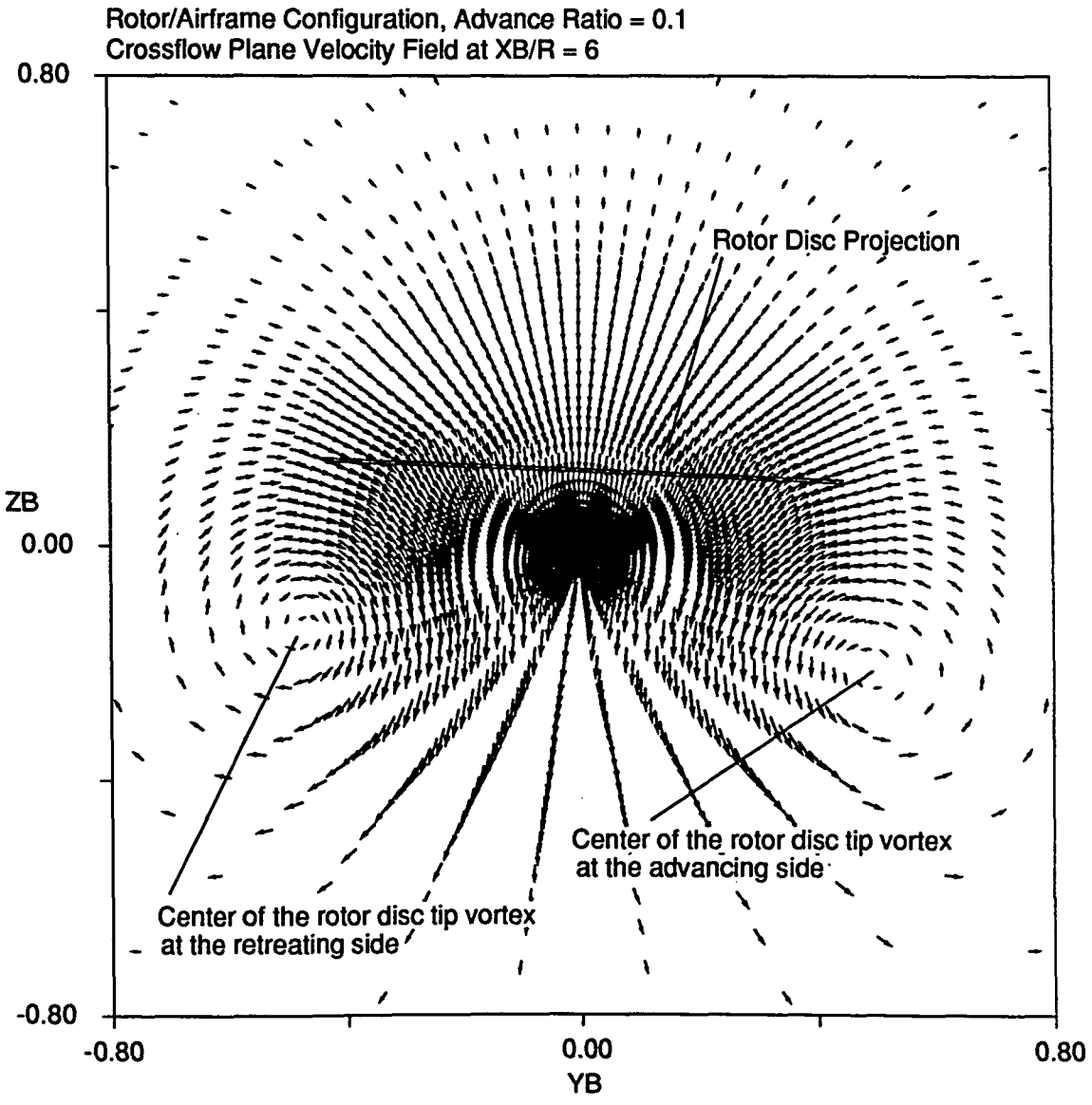

Figure 4.33: Velocity field in the crossflow plane at $X_B/R = 6.0$

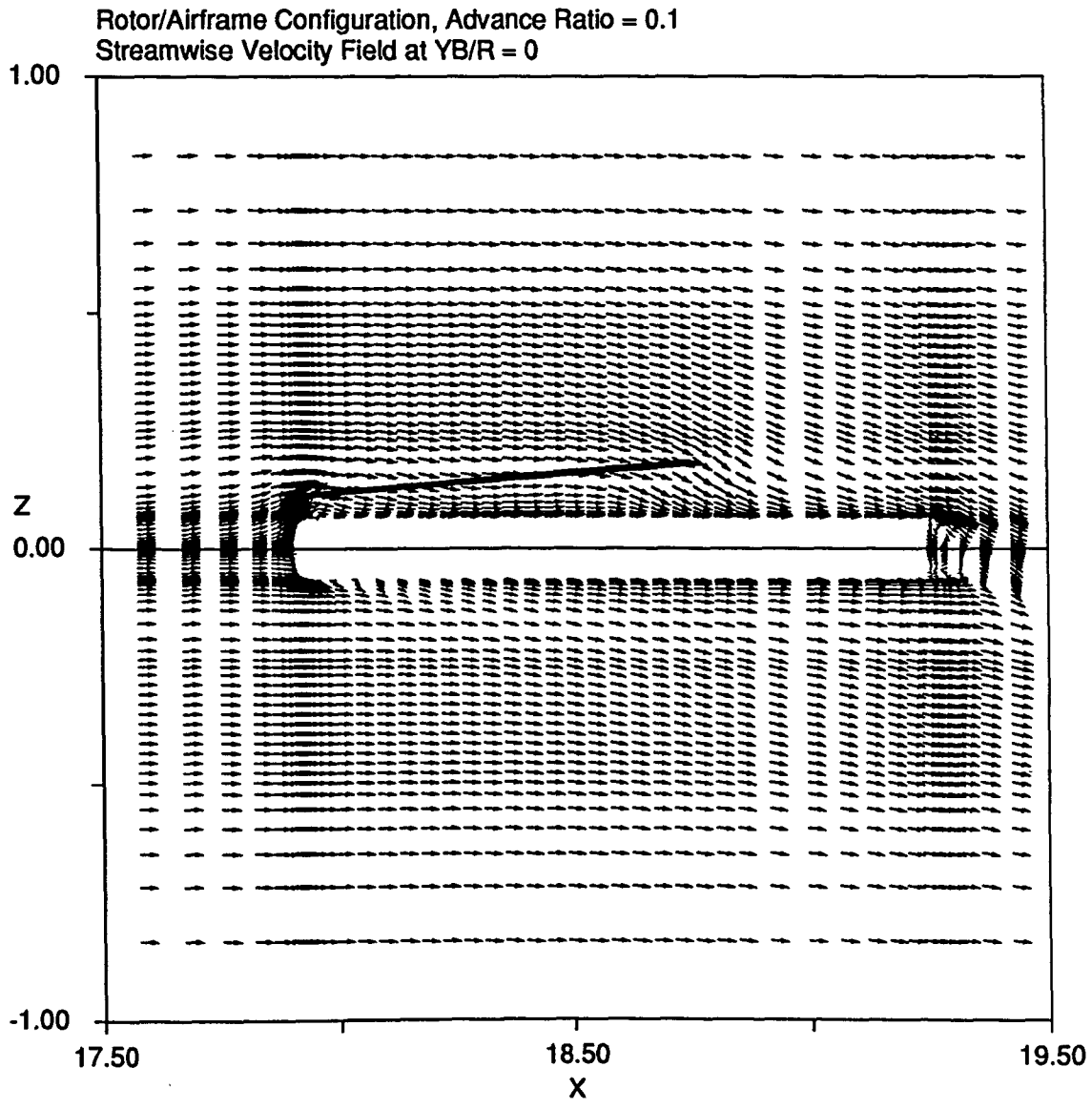

Figure 4.34: Velocity field in the streamwise plane at Y_B/R =0

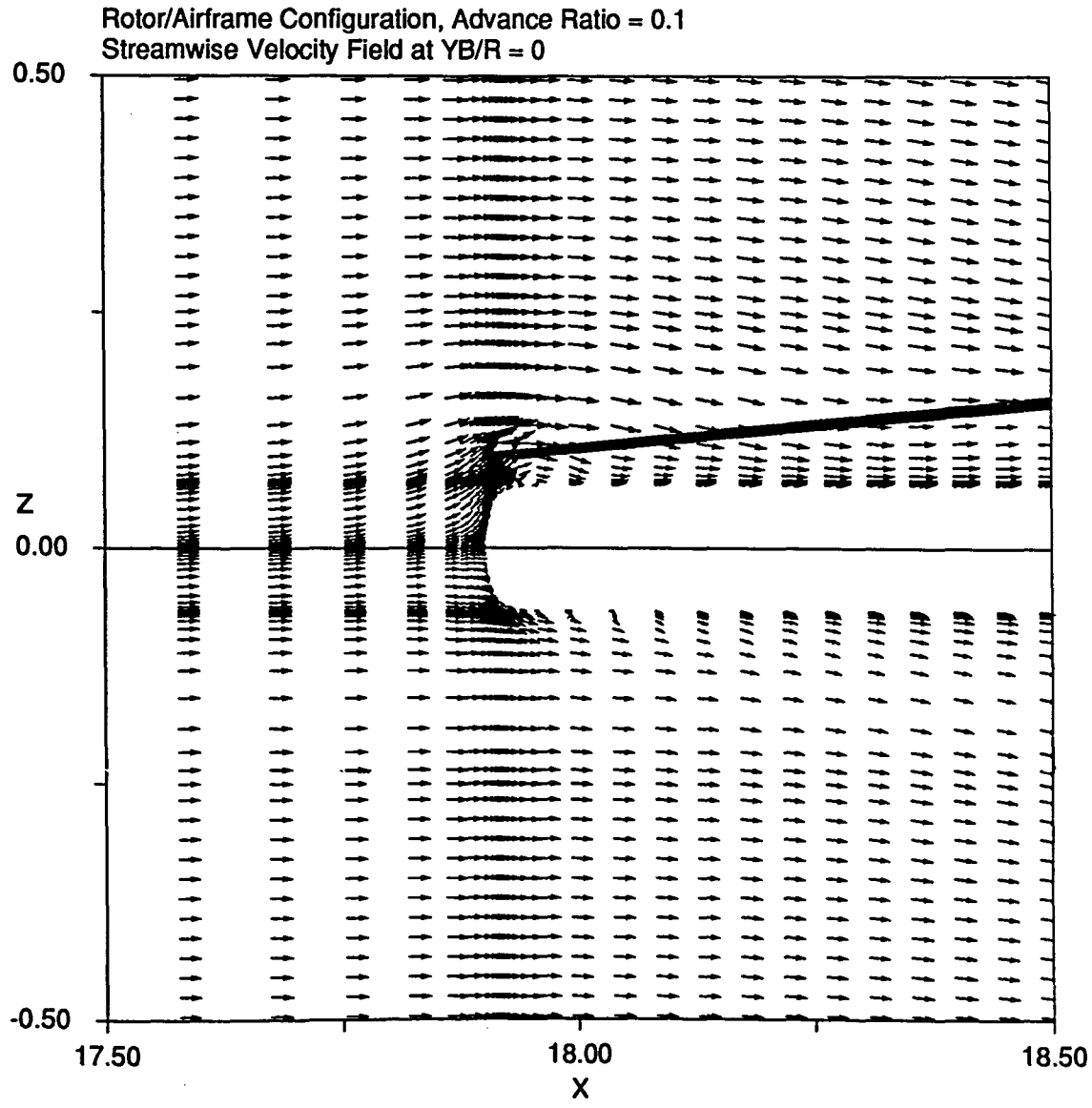

Figure 4.35: Velocity field in the streamwise plane at $Y_B/R = 0$

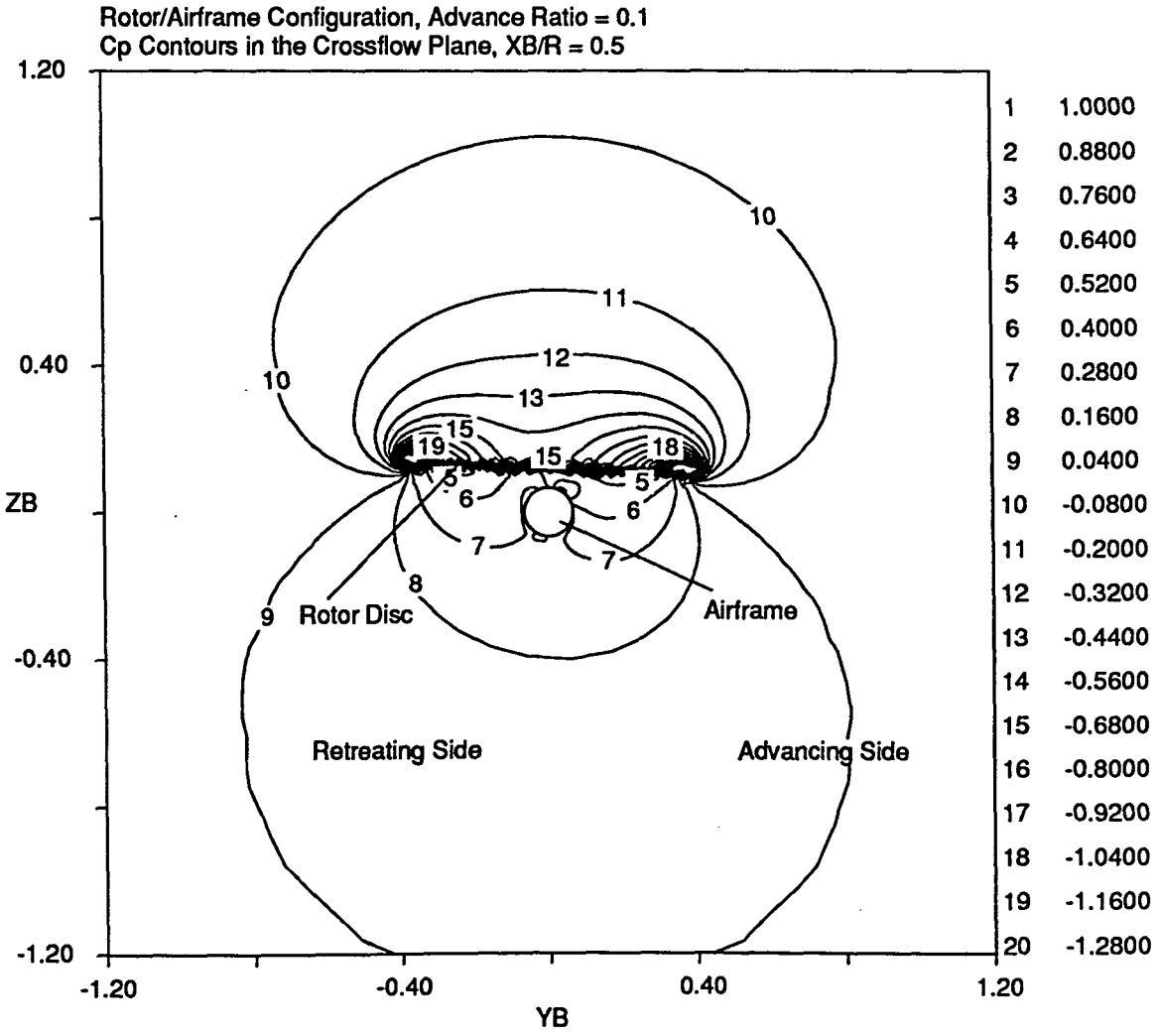

Figure 4.36: Pressure contours in the crossflow plane at $X_B/R = 0.5$

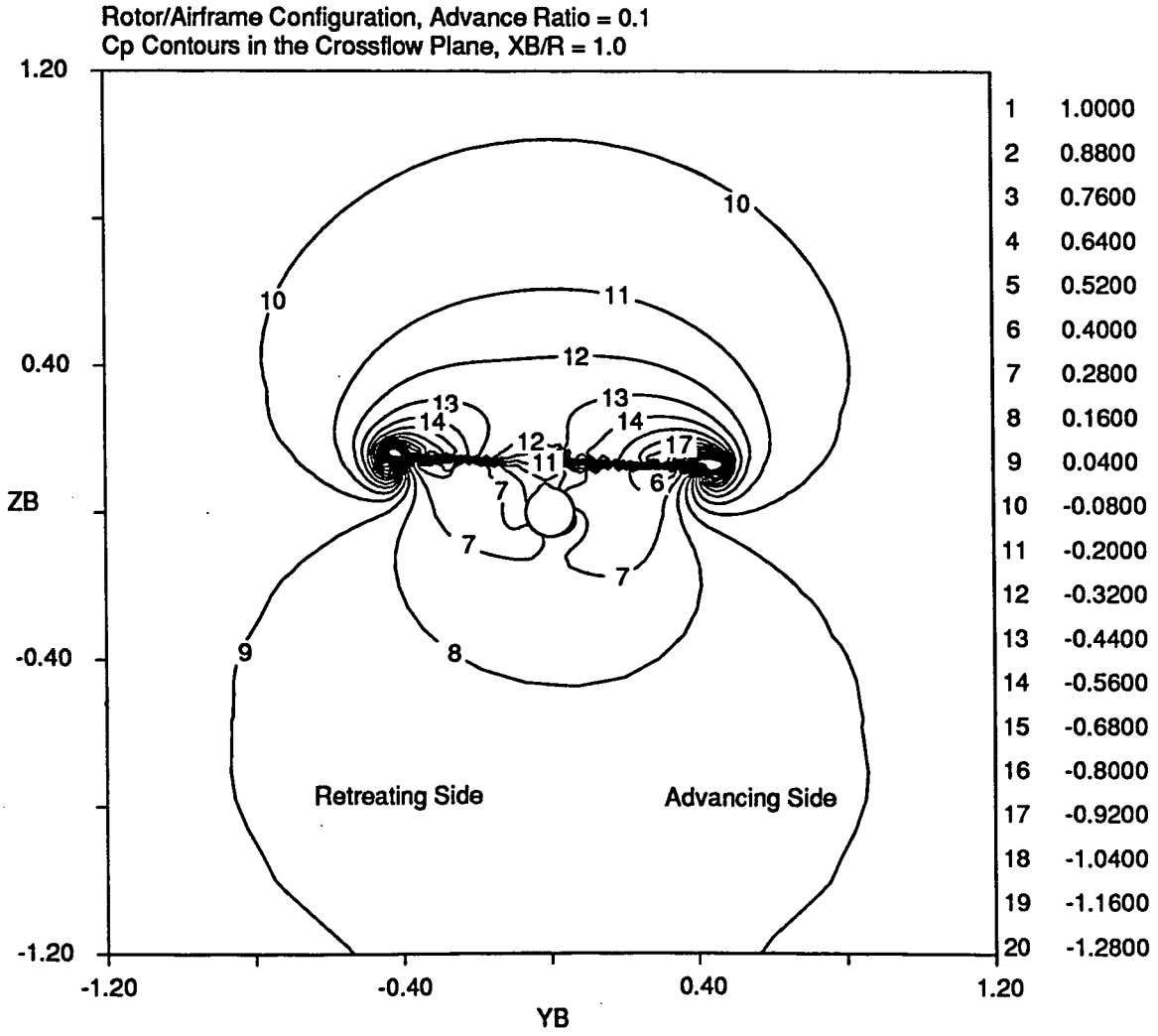

Figure 4.37: Pressure contours in the crossflow plane at $X_B/R = 1.0$

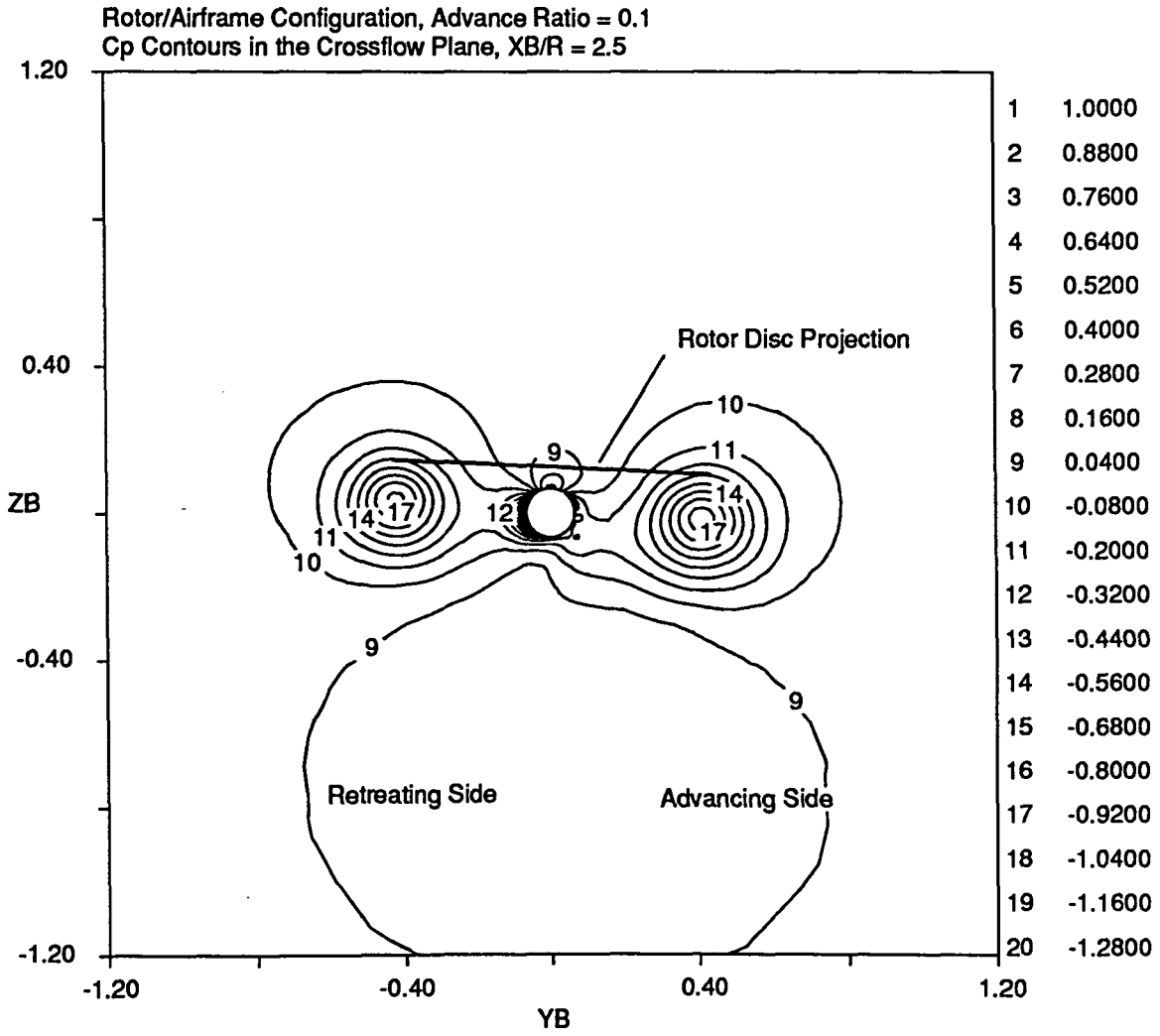

Figure 4.38: Pressure contours in the crossflow plane at $X_B/R = 2.5$

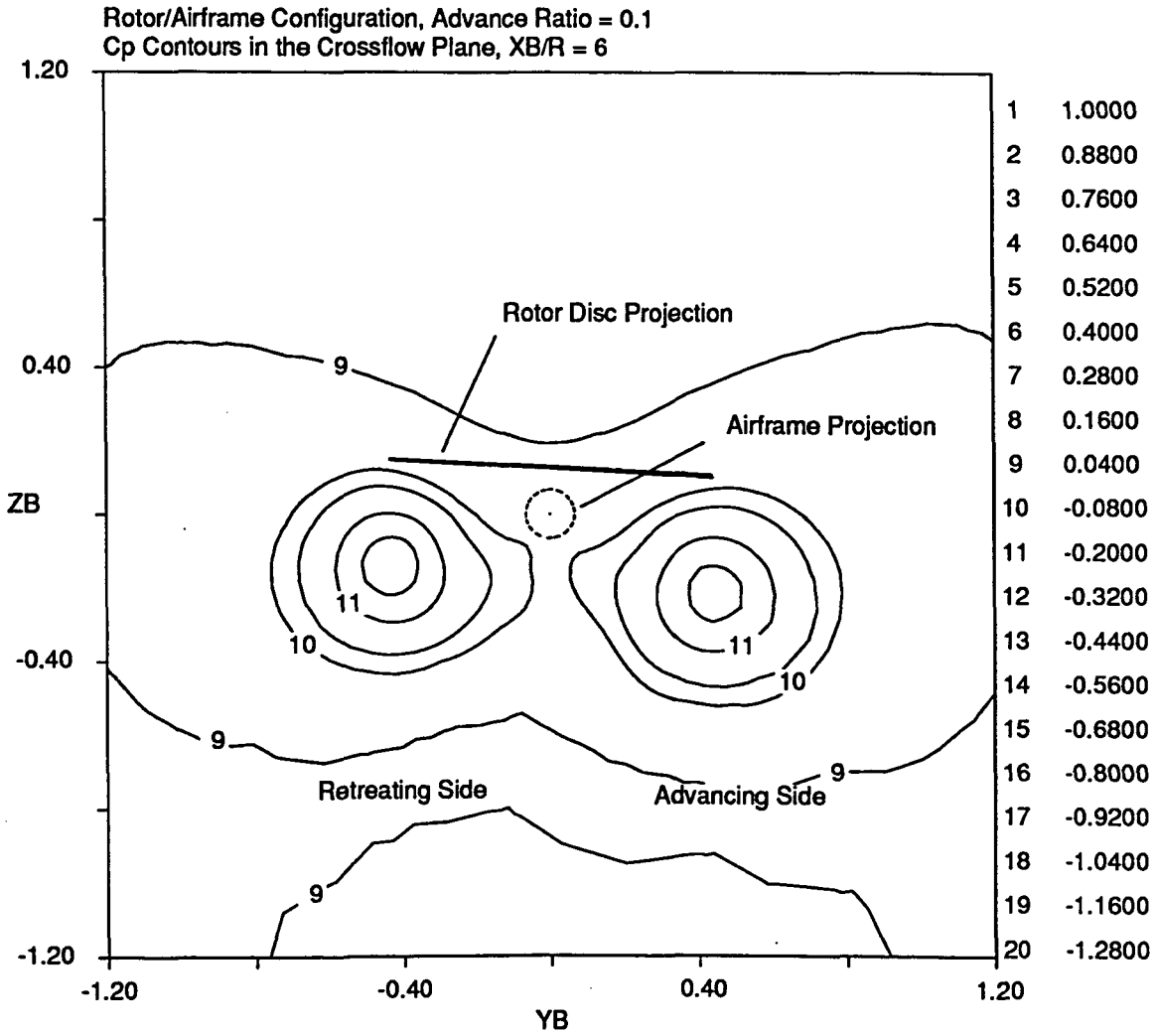

Figure 4.39: Pressure contours in the crossflow plane at $X_B/R = 6.0$

CHAPTER 5. CONCLUSIONS

A method for predicting the aerodynamic loads on the rotor blades and for analyzing the mutual aerodynamic interaction between a rotor and an airframe model has been presented. This technique models the rotor implicitly through the source terms of the momentum equations. Three–dimensional, cylindrical coordinate, incompressible, laminar, finite volume, Navier–Stokes solver based on SIMPLER algorithm was developed for analyzing the rotor/airframe problem.

The computer code is validated by comparing the predicted theoretical load distribution, on an H–34 rotor at advance ratios of 0.064, 0.129 and 0.227, with the results obtained from a previously developed code [21] and experimental data. The calculations for the aerodynamic interaction problem are performed on a simplified rotor/airframe model at an advance ratio of 0.1. The airframe surface pressure predictions are found to be in good agreement with wind tunnel test data. A slight increase in upwash and a small change in blade load distribution near the rotor azimuth of $\psi = 180°$ are observed (due to the presence of the airframe). The rotor's influence on the airframe aerodynamics is more profound than the airframe interference on the rotor blade aerodynamics.

The momentum–source concept, applied to the aerodynamic analysis of forward flight, in the current work has shown to be an effective and ingenious way of circum-

venting the large computer memory and computational expenses that would have been required for a similar application using the traditional full Navier–Stokes methods. An attractive feature of the present method is the fact that no wake modelling is necessary. The wake is properly accounted for by the governing fluid flow equations and develops as part of the solution.

The method presented in this thesis provided, in general, encouraging and promising predictions. Yet, there still exist some deficiencies in the modelling of the rotor/airframe interaction problem. As we have learned from the previous chapter, the flowfield around a rotor/airframe configuration in forward flight is extremely complex. Moreover, numerous experimental investigators ([4],[5],[6],[7],[10]) have reported that the aerodynamic interaction between the components of a helicopter are characterized by highly unsteady aerodynamic behaviors, such as large pressure oscillation at the fuselage due to mainly periodic blade passage and rotor vortex–blade impingement on the airframe surface. Therefore, design–standard predictions can not be accurately established until these complex phenomena are carefully modelled. A list of possible improvements to the current analysis for better computational predictions are given below.

1. Modifying the current steady solver to a time–dependent algorithm to enhance the predictions of vortex–blade interactions and vortex impingement on body.

2. Inclusion of a body fitted generalized coordinates for better flow modelling over the airframe and for precise drag calculations.

3. Additions of a turbulence model to accurately capture the viscous wake interactions between the blades and the airframe.

4. Incorporation of an elastic blade motion and blade response analysis for accurate blade load estimation.

Being a proof of concept, the code developed in this work has not been optimized for computational efficiency. It is very well recognized that there is room for improvement in rewriting the flow solver. Moreover, with simple modifications, the vectorizing and multiprocessing capabilities of the present day supercomputers can be exploited to reduce the CPU requirements.

REFERENCES

[1] Betzina M. D., Smith C. A. and Shinoda P., "Rotor/Body Aerodynamic Interactions," Vertica, Vol. 9, No. 1, pp. 65-81, 1985.

[2] Wilby P. G., Young C. and Grant J., "An Investigation of The Influence of Fuselage Flow Field on Rotor Loads and The Effects of Vehicle Configuration," Vertica, Vol. 3, pp. 79-94, 1979.

[3] Sheridan P. F. and Smith R. P., "Interactional Aerodynamics - A New Challenge to Helicopter Technology," Print No. 79-59, Presented at the 35th Annual Forum of the American Helicopter Society, Washington D.C., May 1979.

[4] Leishman J. G., Bi N., Samak D. K. and Green M., "Investigation of Aerodynamic Interactions Between a Rotor and a Fuselage in Forward Flight," Presented at the 45th Annual Forum of the American Helicopter Society, Boston, MA., May 1989.

[5] Leishman J. G. and Bi N., "Aerodynamic Interactions Between a Rotor and a Fuselage in Forward Flight," Journal of the American Helicopter Society, Vol. 35, No. 3, pp. 22-31, 1990.

[6] Brand A. G., McMahon H. M. and Komerath N. M., "Correlation of Rotor Wake/Airframe Interaction Measurements with Flow Visualization Data," Journal of the American Helicopter Society, Vol. 35, No. 4, pp. 4-15, 1990.

[7] Brand A. G., McMahon H. M. and Komerath N. M., "Surface Pressure Measurements on a Body Subjected to Vortex Wake Interaction," AIAA Journal, Vol. 27, No. 5, pp. 569-574, 1989.

[8] Brand A. G., McMahon H. M. and Komerath N. M., "Results from Laser Sheet Visualization of a Periodic Rotor Wake," Journal of Aircraft, Vol. 26, No. 5, pp. 438-443, 1989.

[9] Brand A. G., Komerath N. M. and McMahon H. M., "Wind Tunnel Data From a Rotor Wake/Airframe Interaction Study," School of Aerospace Engineering, Georgia Institute of Technology, Contract No. DAAG29-82-K-0094, July 1986.

[10] Liou S. G., Komerath N. M. and McMahon H. M., "Velocity Measurements of Airframe Effects on a Rotor in Low-Speed Forward Flight," Journal of Aircraft, Vol. 26, No. 4, pp. 340-348, 1989.

[11] Liou S. G., Komerath N. M. and McMahon H. M., "Velocity Field of a Cylinder in the Wake of a Rotor in Forward Flight," Journal of Aircraft, Vol. 27, No. 9, pp. 804-809, 1990.

[12] Liou S. G., Komerath N. M. and McMahon H. M., "Measurement of the Interaction Between a Rotor Tip Vortex and a Cylinder," AIAA Journal, Vol. 28, No. 6, pp. 975-981, 1990.

[13] Lorber P. F. and Egolf T. A., "An Unsteady Helicopter Rotor-Fuselage Aerodynamic Interaction Analysis," Journal of the American Helicopter Society, Vol. 35, No. 3, pp. 32-42, 1990.

[14] Mavris D. N., Komerath N. M. and McMahon H. M., "Predicition of Aerodynamic Rotor-Airframe Interaction in Forward Flight," Journal of the American Helicopter Society, Vol. 34, No. 4, pp. 37-46, 1989.

[15] Brian E. W. and Sankar L. N. "Solution of the Navier–Stokes Equations for the Flow About a Rotor Blade," Journal of the American Helicopter Society, Vol. 34, No. 2, pp. 13-23, 1989.

[16] Srinivasan G. R. and McCroskey W. J., "Navier–Stokes Calculations of Hovering Rotor Flowfields," Journal of Aircraft, Vol. 25, No. 10, pp. 865-874, 1988.

[17] Rajagopalan R.G. and Fanucci J. B. "Finite Difference Model for Vertical Axis Wind Rotors," Journal of Propulsion and Power, Vol. 1, No.6, pp. 432-436, 1985.

[18] Rajagopalan R. G. and Zhang Zhaoxing, "Performance and Flow Field of a Ducted Propeller," AIAA/ASME/SAE/ASEE 25th Joint Propulsion Conference, Monterey, CA., July 10-12, 1989.

[19] Rajagopalan R. G. and Lim C. K., "Laminar Flow Analysis of a Rotor in Hover," Journal of the American Helicopter Society, Vol. 36, No. 1, pp. 12-23, 1991.

[20] Mathur S. R., "Three dimensional analysis of a rotor in forward flight," M.S. Thesis, Iowa State University, 1989.

[21] Rajagopalan R. G. and Mathur S. R., "Three dimensional analysis of a rotor in forward flight," Presented at the 47th Annual Forum of the American Helicopter Society, Phoenix, Arizona, May 1991.

[22] Patankar S. V., "Numerical Heat Transfer and Fluid Flow," Hemisphere Publishing Corporation, 1980.

[23] Scheiman J., "A Tabulation of Helicopter Rotor–Blade Differential Pressures, and Motions as Measured in Flight," NASA TM X-952, March 1964.

[24] Egolf T. A. and Landgrebe A. J., "Helicopter Rotor Wake Geometry and Its Influence in Forward Flight.Volume I- Generalized Wake Geometry and Wake Effect on Rotor Airloads and Performance," NASA Contractor Report 3726, Oct. 1983.

APPENDIX A. GOVERNING FLUID FLOW EQUATIONS

Development of the Navier-Stokes equations for 3–D, steady, incompressible, laminar, general orthogonal, curvilinear coordinates.

The purpose here is to develop the 3–D, steady , incompressible, laminar, N–S equations in general orthogonal curvilinear coordinate system. The mass and momentum conservation equations describe low speed fluid motion adequately and are developed sequentially in what is to follow.

I. Conservation of Mass

The conservation of mass law applied to a fluid passing through an infinitesimal fixed control volume yields the following equation of continuity

$$\frac{\partial \rho}{\partial t} + \nabla \bullet \left(\rho \vec{V}\right) = 0 \tag{A.1}$$

When the flow is steady the field properties are not functions of time and the continuity equation reduces to

$$\nabla \bullet \left(\rho \vec{V}\right) = 0 \tag{A.2}$$

If the fluid is incompressible, ρ is constant and the above equation becomes

$$\nabla \bullet \vec{V} = 0 \tag{A.3}$$

For

$$\rho\vec{V} = \rho u\hat{e}_1 + \rho v\hat{e}_2 + \rho w\hat{e}_3 \tag{A.4}$$

Equation A.2 can be expanded and the continuity equation can be written in general orthogonal curvilinear coordinates as follows

$$\frac{1}{h_1h_2h_3}\left[\frac{\partial}{\partial x_1}(h_2h_3\rho u) + \frac{\partial}{\partial x_2}(h_1h_3\rho v) + \frac{\partial}{\partial x_3}(h_1h_2\rho w)\right] = 0 \tag{A.5}$$

here u, v, w are the velocity components, x_1, x_2, x_3 are the coordinate directions, and h_1, h_2, h_3 are the scale factors of the coordinate system.

II. Conservation of Momentum

Newton's second law applied to a fluid passing through an infinitesimal, fixed control volume yields the following momentum equation:

$$\frac{\partial}{\partial t}\left(\rho\vec{V}\right) + \nabla \bullet \rho\vec{V}\vec{V} = \rho\vec{f} + \nabla \bullet \Pi_{ij} \tag{A.6}$$

assuming :

- Steady flow $\Longrightarrow \frac{\partial}{\partial t} = 0$
- No body forces $\Longrightarrow \rho\vec{f} = 0$

the momentum equation reduces to

$$\nabla \bullet \rho\vec{V}\vec{V} = \nabla \bullet \Pi_{ij} \tag{A.7}$$

where

$$\nabla \bullet \Pi_{ij} = \nabla \bullet \left[-p\tilde{I} + \tilde{\tau}\right] \tag{A.8}$$

Expanding the right hand side we get:

$$\nabla \bullet \Pi_{ij} = -\left(\tilde{I} \bullet \nabla\right)p - \nabla\left(\nabla \bullet \tilde{I}\right) + \nabla \bullet \tilde{\tau} \tag{A.9}$$

The first term on the right–hand side of the above equation is the pressure gradient ∇p. The second term will vanish to zero for general orthogonal coordinates. Thus the momentum equation can be reduced to the following equation:

$$\nabla \bullet \rho \vec{V} \vec{V} = -\nabla p + \nabla \bullet \tilde{\tau} \tag{A.10}$$

where

$$\tilde{\tau} = \mu \left[\nabla \vec{V} + \left(\nabla \vec{V} \right)^T - \frac{2}{3} \left(\nabla \bullet \vec{V} \right) \tilde{I} \right] \tag{A.11}$$

If we assume the flow to be incompressible, $\nabla \bullet \vec{V} = 0$ from continuity. Moreover, it can be shown that for incompressible flow the term $\nabla \bullet \left(\nabla \vec{V} \right)^T = 0$. Consequently, the momentum equation can now be written as:

$$\nabla \bullet \rho \vec{V} \vec{V} = -\nabla p + \nabla \bullet \left(\mu \nabla \vec{V} \right) \tag{A.12}$$

It is to be mentioned that ρ and μ are treated as variables in the developments that follow for the sake of adopting these equations for compressible flow with additional terms. To expand the above equation the following terms need to be evaluated:

1. $\nabla \bullet \left(\mu \nabla \vec{V} \right)$
2. $\nabla \bullet \left(\rho \vec{V} \vec{V} \right)$
3. ∇p

for

$$\nabla = \frac{\hat{e}_1}{h_1} \frac{\partial}{\partial x_1} + \frac{\hat{e}_2}{h_2} \frac{\partial}{\partial x_2} + \frac{\hat{e}_3}{h_3} \frac{\partial}{\partial x_3} \tag{A.13}$$

and

$$\vec{V} = u\hat{e}_1 + v\hat{e}_2 + w\hat{e}_3 \tag{A.14}$$

The tensor

$$\mu\nabla\vec{V} = \mu\left(\frac{\hat{e}_1}{h_1}\frac{\partial}{\partial x_1}+\frac{\hat{e}_2}{h_2}\frac{\partial}{\partial x_2}+\frac{\hat{e}_3}{h_3}\frac{\partial}{\partial x_3}\right)(u\hat{e}_1+v\hat{e}_2+w\hat{e}_3) \qquad \text{(A.15)}$$

$$= \begin{bmatrix} A_1 & A_2 & A_3 \\ A_4 & A_5 & A_6 \\ A_7 & A_8 & A_9 \end{bmatrix}$$

where

$$\begin{aligned}
A_1 &= \frac{\mu}{h_1}\frac{\partial u}{\partial x_1}+\frac{\mu v}{h_1h_2}\frac{\partial h_1}{\partial x_2}+\frac{\mu w}{h_1h_3}\frac{\partial h_1}{\partial x_3} \\
A_2 &= \frac{\mu}{h_1}\frac{\partial v}{\partial x_1}-\frac{\mu u}{h_1h_2}\frac{\partial h_1}{\partial x_2} \\
A_3 &= \frac{\mu}{h_1}\frac{\partial w}{\partial x_1}-\frac{\mu u}{h_1h_3}\frac{\partial h_1}{\partial x_3} \\
A_4 &= \frac{\mu}{h_2}\frac{\partial u}{\partial x_2}-\frac{\mu v}{h_1h_2}\frac{\partial h_2}{\partial x_1} \\
A_5 &= \frac{\mu}{h_2}\frac{\partial v}{\partial x_2}+\frac{\mu u}{h_1h_2}\frac{\partial h_2}{\partial x_1}+\frac{\mu w}{h_2h_3}\frac{\partial h_2}{\partial x_3} \\
A_6 &= \frac{\mu}{h_2}\frac{\partial w}{\partial x_2}-\frac{\mu v}{h_2h_3}\frac{\partial h_2}{\partial x_3} \\
A_7 &= \frac{\mu}{h_3}\frac{\partial u}{\partial x_3}-\frac{\mu w}{h_1h_3}\frac{\partial h_3}{\partial x_1} \\
A_8 &= \frac{\mu}{h_3}\frac{\partial v}{\partial x_3}-\frac{\mu w}{h_2h_3}\frac{\partial h_3}{\partial x_2} \\
A_9 &= \frac{\mu}{h_3}\frac{\partial w}{\partial x_3}+\frac{\mu u}{h_1h_3}\frac{\partial h_3}{\partial x_1}+\frac{\mu v}{h_2h_3}\frac{\partial h_3}{\partial x_2}
\end{aligned} \qquad \text{(A.16)}$$

The expression, $\nabla \bullet \left(\mu\nabla\vec{V}\right)$, which is contained in the momentum equation can be evaluated as

$$\nabla \bullet \left(\mu\nabla\vec{V}\right) = \left(\frac{\hat{e}_1}{h_1}\frac{\partial}{\partial x_1}+\frac{\hat{e}_2}{h_2}\frac{\partial}{\partial x_2}+\frac{\hat{e}_3}{h_3}\frac{\partial}{\partial x_3}\right)\bullet\begin{bmatrix} A_1 & A_2 & A_3 \\ A_4 & A_5 & A_6 \\ A_7 & A_8 & A_9 \end{bmatrix} \qquad \text{(A.17)}$$

and the term, $\nabla \bullet \rho\vec{V}\vec{V}$, can be written as

$$\nabla \bullet \rho\vec{V}\vec{V} = \left(\frac{\hat{e}_1}{h_1}\frac{\partial}{\partial x_1} + \frac{\hat{e}_2}{h_2}\frac{\partial}{\partial x_2} + \frac{\hat{e}_3}{h_3}\frac{\partial}{\partial x_3}\right) \bullet \rho\vec{V}\vec{V} \tag{A.18}$$

where the tensor, $\rho\vec{V}\vec{V}$, is shown below

$$\rho\vec{V}\vec{V} = \begin{bmatrix} \rho uu & \rho uv & \rho uw \\ \rho vu & \rho vv & \rho vw \\ \rho wu & \rho wv & \rho ww \end{bmatrix} \tag{A.19}$$

Finally, the pressure gradient term, ∇p, can be written in expanded form to yield:

$$\nabla p = \frac{\hat{e}_1}{h_1}\frac{\partial p}{\partial x_1} + \frac{\hat{e}_2}{h_2}\frac{\partial p}{\partial x_2} + \frac{\hat{e}_3}{h_3}\frac{\partial p}{\partial x_3} \tag{A.20}$$

Upon substituting Equations A.17, A.18 and A.20 into Equation A.12, and after expanding and regrouping the terms, the Navier–Stokes equations are obtained. For a general orthogonal curvilinear coordinate, the Navier–Stokes equation can be separated into the following three scalar equations:

x_1 momentum :

$$\frac{1}{h_1h_2h_3}\left[\frac{\partial}{\partial x_1}\left(h_2h_3\rho uu - \frac{h_2h_3}{h_1}\mu\frac{\partial u}{\partial x_1}\right) + \frac{\partial}{\partial x_2}\left(h_1h_3\rho vu - \frac{h_1h_3}{h_2}\mu\frac{\partial u}{\partial x_2}\right) + \frac{\partial}{\partial x_3}\left(h_1h_2\rho wu - \frac{h_1h_2}{h_3}\mu\frac{\partial u}{\partial x_3}\right)\right] =$$

$$-\frac{1}{h_1}\frac{\partial p}{\partial x_1} + \frac{\rho vv}{h_1h_2}\frac{\partial h_2}{\partial x_1} + \frac{\rho ww}{h_1h_3}\frac{\partial h_3}{\partial x_1} - \frac{\rho uv}{h_1h_2}\frac{\partial h_1}{\partial x_2} - \frac{\rho uw}{h_1h_3}\frac{\partial h_1}{\partial x_3}$$

$$+\frac{1}{h_1}\frac{\partial}{\partial x_1}\left(\frac{\mu v}{h_1h_2}\frac{\partial h_1}{\partial x_2} + \frac{\mu w}{h_1h_3}\frac{\partial h_1}{\partial x_3}\right) - \frac{1}{h_2}\frac{\partial}{\partial x_2}\left(\frac{\mu v}{h_1h_2}\frac{\partial h_2}{\partial x_1}\right) - \frac{1}{h_3}\frac{\partial}{\partial x_3}\left(\frac{\mu w}{h_1h_3}\frac{\partial h_3}{\partial x_1}\right)$$

$$+\frac{1}{h_1h_2}\left(\frac{\mu w}{h_1h_3}\frac{\partial h_1}{\partial x_3} - \frac{\mu}{h_2}\frac{\partial v}{\partial x_2} - \frac{\mu u}{h_1h_2}\frac{\partial h_2}{\partial x_1} - \frac{\mu w}{h_2h_3}\frac{\partial h_2}{\partial x_3}\right)\frac{\partial h_2}{\partial x_1}$$

$$+\frac{1}{h_1h_3}\left(\frac{\mu v}{h_1h_2}\frac{\partial h_1}{\partial x_2}-\frac{\mu}{h_3}\frac{\partial w}{\partial x_3}-\frac{\mu u}{h_1h_3}\frac{\partial h_3}{\partial x_1}-\frac{\mu v}{h_2h_3}\frac{\partial h_3}{\partial x_2}\right)\frac{\partial h_3}{\partial x_1}$$
$$+\frac{1}{h_1h_2}\left(\frac{\mu}{h_1}\frac{\partial v}{\partial x_1}-\frac{\mu u}{h_1h_2}\frac{\partial h_1}{\partial x_2}\right)\frac{\partial h_1}{\partial x_2}-\frac{1}{h_2h_3}\left(\frac{\mu v}{h_1h_2}\frac{\partial h_2}{\partial x_1}\right)\frac{\partial h_3}{\partial x_2}$$
$$+\frac{1}{h_1h_3}\left(\frac{\mu}{h_1}\frac{\partial w}{\partial x_1}-\frac{\mu u}{h_1h_3}\frac{\partial h_1}{\partial x_3}\right)\frac{\partial h_1}{\partial x_3}-\frac{1}{h_2h_3}\left(\frac{\mu w}{h_1h_3}\frac{\partial h_3}{\partial x_1}\right)\frac{\partial h_2}{\partial x_3} \qquad \text{(A.21)}$$

x_2 momentum :

$$\frac{1}{h_1h_2h_3}\left[\frac{\partial}{\partial x_1}\left(h_2h_3\rho uv-\frac{h_2h_3}{h_1}\mu\frac{\partial v}{\partial x_1}\right)+\frac{\partial}{\partial x_2}\left(h_1h_3\rho vv-\frac{h_1h_3}{h_2}\mu\frac{\partial v}{\partial x_2}\right)+\right.$$
$$\left.\frac{\partial}{\partial x_3}\left(h_1h_2\rho wv-\frac{h_1h_2}{h_3}\mu\frac{\partial v}{\partial x_3}\right)\right]=$$
$$-\frac{1}{h_2}\frac{\partial p}{\partial x_2}+\frac{\rho uu}{h_1h_2}\frac{\partial h_1}{\partial x_2}+\frac{\rho ww}{h_2h_3}\frac{\partial h_3}{\partial x_2}-\frac{\rho uv}{h_1h_2}\frac{\partial h_2}{\partial x_1}-\frac{\rho wv}{h_2h_3}\frac{\partial h_2}{\partial x_3}$$
$$-\frac{1}{h_1}\frac{\partial}{\partial x_1}\left(\frac{\mu u}{h_1h_2}\frac{\partial h_1}{\partial x_2}\right)+\frac{1}{h_2}\frac{\partial}{\partial x_2}\left(\frac{\mu u}{h_1h_2}\frac{\partial h_2}{\partial x_1}+\frac{\mu w}{h_2h_3}\frac{\partial h_2}{\partial x_3}\right)-\frac{1}{h_3}\frac{\partial}{\partial x_3}\left(\frac{\mu w}{h_2h_3}\frac{\partial h_3}{\partial x_2}\right)$$
$$+\frac{1}{h_1h_2}\left(\frac{\mu}{h_2}\frac{\partial u}{\partial x_2}-\frac{\mu v}{h_1h_2}\frac{\partial h_2}{\partial x_1}\right)\frac{\partial h_2}{\partial x_1}-\frac{1}{h_1h_3}\left(\frac{\mu u}{h_1h_2}\frac{\partial h_1}{\partial x_2}\right)\frac{\partial h_3}{\partial x_1}$$
$$+\frac{1}{h_1h_2}\left(\frac{\mu w}{h_2h_3}\frac{\partial h_2}{\partial x_3}-\frac{\mu}{h_1}\frac{\partial u}{\partial x_1}-\frac{\mu v}{h_1h_2}\frac{\partial h_1}{\partial x_2}-\frac{\mu w}{h_1h_3}\frac{\partial h_1}{\partial x_3}\right)\frac{\partial h_1}{\partial x_2}$$
$$+\frac{1}{h_2h_3}\left(\frac{\mu u}{h_1h_2}\frac{\partial h_2}{\partial x_1}-\frac{\mu}{h_3}\frac{\partial w}{\partial x_3}-\frac{\mu u}{h_1h_3}\frac{\partial h_3}{\partial x_1}-\frac{\mu v}{h_2h_3}\frac{\partial h_3}{\partial x_2}\right)\frac{\partial h_3}{\partial x_2}$$
$$+\frac{1}{h_2h_3}\left(\frac{\mu}{h_2}\frac{\partial w}{\partial x_2}-\frac{\mu v}{h_2h_3}\frac{\partial h_2}{\partial x_3}\right)\frac{\partial h_2}{\partial x_3}-\frac{1}{h_1h_3}\left(\frac{\mu w}{h_2h_3}\frac{\partial h_3}{\partial x_2}\right)\frac{\partial h_1}{\partial x_3} \qquad \text{(A.22)}$$

x_3 momentum :

$$\frac{1}{h_1h_2h_3}\left[\frac{\partial}{\partial x_1}\left(h_2h_3\rho uw-\frac{h_2h_3}{h_1}\mu\frac{\partial w}{\partial x_1}\right)+\frac{\partial}{\partial x_2}\left(h_1h_3\rho vw-\frac{h_1h_3}{h_2}\mu\frac{\partial w}{\partial x_2}\right)+\right.$$
$$\left.\frac{\partial}{\partial x_3}\left(h_1h_2\rho ww-\frac{h_1h_2}{h_3}\mu\frac{\partial w}{\partial x_3}\right)\right]=$$

$$
\begin{aligned}
&-\frac{1}{h_3}\frac{\partial p}{\partial x_3}+\frac{\rho uu}{h_1h_3}\frac{\partial h_1}{\partial x_3}+\frac{\rho vv}{h_2h_3}\frac{\partial h_3}{\partial x_3}-\frac{\rho uw}{h_1h_2}\frac{\partial h_3}{\partial x_1}-\frac{\rho vw}{h_2h_3}\frac{\partial h_3}{\partial x_2}\\
&-\frac{1}{h_1}\frac{\partial}{\partial x_1}\left(\frac{\mu u}{h_1h_3}\frac{\partial h_1}{\partial x_3}\right)-\frac{1}{h_2}\frac{\partial}{\partial x_2}\left(\frac{\mu v}{h_2h_3}\frac{\partial h_2}{\partial x_3}\right)+\frac{1}{h_3}\frac{\partial}{\partial x_3}\left(\frac{\mu u}{h_1h_3}\frac{\partial h_3}{\partial x_1}+\frac{\mu v}{h_2h_3}\frac{\partial h_3}{\partial x_2}\right)\\
&+\frac{1}{h_1h_3}\left(\frac{\mu}{h_3}\frac{\partial u}{\partial x_3}-\frac{\mu w}{h_1h_3}\frac{\partial h_3}{\partial x_1}\right)\frac{\partial h_3}{\partial x_1}-\frac{1}{h_1h_2}\left(\frac{\mu u}{h_1h_3}\frac{\partial h_1}{\partial x_3}\right)\frac{\partial h_2}{\partial x_1}\\
&+\frac{1}{h_2h_3}\left(\frac{\mu}{h_3}\frac{\partial v}{\partial x_3}-\frac{\mu w}{h_2h_3}\frac{\partial h_3}{\partial x_2}\right)\frac{\partial h_3}{\partial x_2}-\frac{1}{h_1h_2}\left(\frac{\mu v}{h_2h_3}\frac{\partial h_2}{\partial x_3}\right)\frac{\partial h_1}{\partial x_2}\\
&+\frac{1}{h_1h_3}\left(\frac{\mu v}{h_2h_3}\frac{\partial h_3}{\partial x_2}-\frac{\mu}{h_1}\frac{\partial u}{\partial x_1}-\frac{\mu v}{h_1h_2}\frac{\partial h_1}{\partial x_2}-\frac{\mu w}{h_1h_3}\frac{\partial h_1}{\partial x_3}\right)\frac{\partial h_1}{\partial x_3}\\
&+\frac{1}{h_2h_3}\left(\frac{\mu u}{h_1h_3}\frac{\partial h_3}{\partial x_1}-\frac{\mu}{h_2}\frac{\partial v}{\partial x_2}-\frac{\mu u}{h_1h_3}\frac{\partial h_2}{\partial x_1}-\frac{\mu w}{h_2h_3}\frac{\partial h_2}{\partial x_3}\right)\frac{\partial h_2}{\partial x_3} \qquad \text{(A.23)}
\end{aligned}
$$

Navier–Stokes Equation in 3–D Cylindrical Coordinates

Equations A.5, A.21, A.22, A.23 can be used to derive the steady, incompressible, laminar, Navier-Stokes equations in cylindrical coordinate system by choosing

$$
\begin{aligned}
x_1 &= \mathbf{R} \qquad h_1 = 1 \qquad u = V_R\\
x_2 &= \mathbf{\Phi} \qquad h_2 = \mathbf{R} \qquad v = V_\Phi\\
x_3 &= \mathbf{Z} \qquad h_3 = 1 \qquad w = V_Z
\end{aligned}
$$

The 3–D Navier–Stokes equations in cylindrical coordinates are expressed as follows:

continuity equation:

$$
\frac{1}{\mathbf{R}}\left[\frac{\partial}{\partial \mathbf{R}}(\mathbf{R}\,\rho V_R)+\frac{\partial}{\partial \mathbf{\Phi}}(\rho V_\Phi)+\frac{\partial}{\partial \mathbf{Z}}(\mathbf{R}\,\rho V_Z)\right]=0 \qquad \text{(A.24)}
$$

R momentum equation:

$$\frac{1}{\mathbf{R}}\left[\frac{\partial}{\partial \mathbf{R}}\left(\mathbf{R}\,\rho {V_R}^2-\mu \mathbf{R}\frac{\partial V_R}{\partial \mathbf{R}}\right)+\frac{\partial}{\partial \Phi}\left(\rho V_\Phi V_R-\frac{\mu}{\mathbf{R}}\frac{\partial V_R}{\partial \Phi}\right)\right.$$
$$\left.+\frac{\partial}{\partial \mathbf{Z}}\left(\mathbf{R}\,\rho V_Z V_R-\mu \mathbf{R}\frac{\partial V_R}{\partial \mathbf{Z}}\right)\right]=$$
$$-\frac{\partial p}{\partial \mathbf{R}}+\frac{\rho {V_\Phi}^2}{\mathbf{R}}-\frac{2\mu}{\mathbf{R}^2}\frac{\partial V_\Phi}{\partial \Phi}-\frac{\mu V_R}{\mathbf{R}^2} \tag{A.25}$$

Φ momentum equation:

$$\frac{1}{\mathbf{R}}\left[\frac{\partial}{\partial \mathbf{R}}\left(\mathbf{R}\,\rho V_R V_\Phi-\mu \mathbf{R}\frac{\partial V_\Phi}{\partial \mathbf{R}}\right)+\frac{\partial}{\partial \Phi}\left(\rho {V_\Phi}^2-\frac{\mu}{\mathbf{R}}\frac{\partial V_\Phi}{\partial \Phi}\right)\right.$$
$$\left.+\frac{\partial}{\partial \mathbf{Z}}\left(\mathbf{R}\,\rho V_Z V_\Phi-\mu \mathbf{R}\frac{\partial V_\Phi}{\partial \mathbf{Z}}\right)\right]=$$
$$-\frac{1}{\mathbf{R}}\frac{\partial p}{\partial \Phi}-\frac{\rho V_R V_\Phi}{\mathbf{R}}+\frac{2\mu}{\mathbf{R}^2}\frac{\partial V_R}{\partial \Phi}-\frac{\mu V_\Phi}{\mathbf{R}^2} \tag{A.26}$$

Z momentum equation:

$$\frac{1}{\mathbf{R}}\left[\frac{\partial}{\partial \mathbf{R}}\left(\mathbf{R}\,\rho V_R V_Z-\mu \mathbf{R}\frac{\partial V_Z}{\partial \mathbf{R}}\right)+\frac{\partial}{\partial \Phi}\left(\rho V_\Phi V_Z-\frac{\mu}{\mathbf{R}}\frac{\partial V_Z}{\partial \Phi}\right)\right.$$
$$\left.+\frac{\partial}{\partial \mathbf{Z}}\left(\mathbf{R}\,\rho {V_Z}^2-\mu \mathbf{R}\frac{\partial V_Z}{\partial \mathbf{Z}}\right)\right]=$$
$$-\frac{\partial p}{\partial \mathbf{Z}} \tag{A.27}$$

Discretization of the generic governing equation

The task in this section is to integrate the generic governing equation, Equation 2.6, on a typical control volume in a 3–D cylindrical coordinates shown in Figure A.1, and then write the discretized form of the aforementioned equation.

Consider the following generic governing equation in cylindrical coordinates:

$$\frac{1}{\mathbf{R}}\left[\frac{\partial}{\partial \mathbf{R}}\left(\mathbf{R}\,\rho V_R\, T-\mu \mathbf{R}\frac{\partial T}{\partial \mathbf{R}}\right)+\frac{\partial}{\partial \Phi}\left(\rho V_\Phi\, T-\frac{\mu}{\mathbf{R}}\frac{\partial T}{\partial \Phi}\right)\right.$$

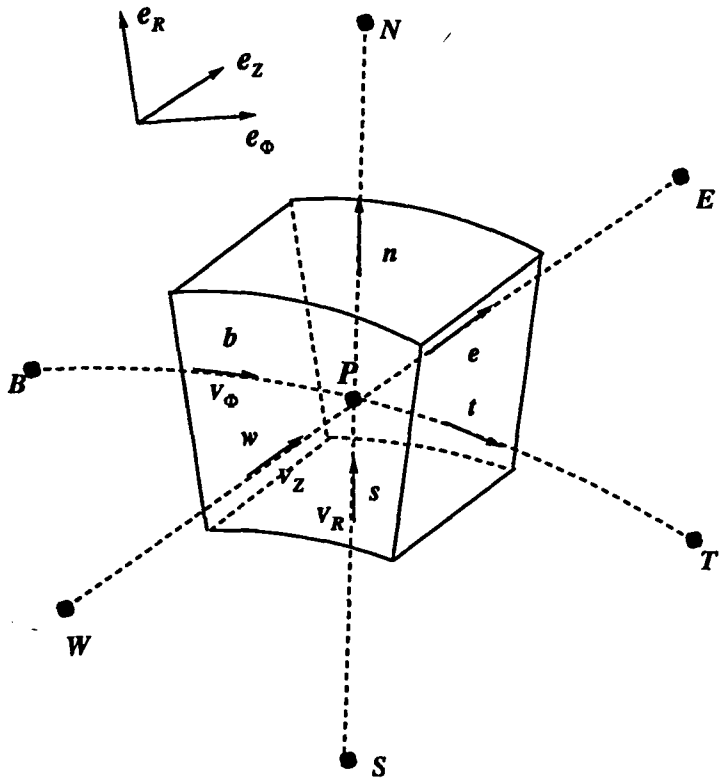

Figure A.1: A typical control volume in a 3–D cylindrical grid

$$+\frac{\partial}{\partial \mathbf{Z}}\left(\mathbf{R}\ \rho V_Z\ T - \mu \mathbf{R}\frac{\partial T}{\partial \mathbf{Z}}\right)\Bigg] = S \qquad \text{(A.28)}$$

Defining the following total fluxes:

$$\begin{aligned} J_{\mathbf{R}} &= \left(\mathbf{R}\ \rho V_R\ T - \mu \mathbf{R}\frac{\partial T}{\partial \mathbf{R}}\right) \\ J_{\mathbf{\Phi}} &= \left(\rho V_\Phi\ T - \frac{\mu}{\mathbf{R}}\frac{\partial T}{\partial \mathbf{\Phi}}\right) \\ J_{\mathbf{Z}} &= \left(\mathbf{R}\ \rho V_Z\ T - \mu \mathbf{R}\frac{\partial T}{\partial \mathbf{Z}}\right) \end{aligned}$$

Equation A.28 can now be rewritten as

$$\frac{1}{\mathbf{R}}\left[\frac{\partial}{\partial \mathbf{R}}\left(J_{\mathbf{R}}\right) + \frac{\partial}{\partial \mathbf{\Phi}}\left(J_{\mathbf{\Phi}}\right) + \frac{\partial}{\partial \mathbf{Z}}\left(J_{\mathbf{Z}}\right)\right] = S \qquad \text{(A.29)}$$

Integrating the above equation over the control volume shown in Figure A.1 we get:

$$\int_w^e \int_b^t \int_s^n \frac{1}{\mathbf{R}}\frac{\partial}{\partial \mathbf{R}}\left(J_{\mathbf{R}}\right)\ \ \mathbf{R}\ d\mathbf{R}\ d\mathbf{\Phi}\ d\mathbf{Z} + \int_w^e \int_b^t \int_s^n \frac{1}{\mathbf{R}}\frac{\partial}{\partial \mathbf{\Phi}}\left(J_{\mathbf{\Phi}}\right)\ \ \mathbf{R}\ d\mathbf{R}\ d\mathbf{\Phi}\ d\mathbf{Z}$$

$$+\int_w^e \int_b^t \int_s^n \frac{1}{\mathbf{R}}\frac{\partial}{\partial \mathbf{Z}}\left(J_{\mathbf{Z}}\right)\ \ \mathbf{R}\ d\mathbf{R}\ d\mathbf{\Phi}\ d\mathbf{Z} = \int_w^e \int_b^t \int_s^n S\ \ \mathbf{R}\ d\mathbf{R}\ d\mathbf{\Phi}\ d\mathbf{Z} \qquad \text{(A.30)}$$

The integration yields the following:

$$\left(J_n - J_s\right) + \left(J_t - J_b\right) + \left(J_e - J_w\right) = \left(S_{const} + S_{coef} T_P\right)\ \mathbf{R}\ \Delta\mathbf{R}\ \Delta\mathbf{\Phi}\ \Delta\mathbf{Z} \qquad \text{(A.31)}$$

where $(S_{const} + S_{coef} T_P)$ is the linearized source term. Hence, S_{const}, stands for the constant part of the linearized source term, S_{coef}, is the coefficient of the independent variable T evaluated at the point P. The integrated total fluxes over the control volume faces J_n, J_s, J_t, J_b, J_e, J_w are given by:

$$\begin{aligned} J_n &= \left(J_{\mathbf{R}}\right)_n\ \left(\Delta\mathbf{\Phi}\ \Delta\mathbf{Z}\right)_n \\ J_s &= \left(J_{\mathbf{R}}\right)_s\ \left(\Delta\mathbf{\Phi}\ \Delta\mathbf{Z}\right)_s \end{aligned}$$

$$
\begin{aligned}
J_t &= (J_\Phi)_t \ (\Delta \mathbf{R}\ \Delta \mathbf{Z})_t \\
J_b &= (J_\Phi)_b \ (\Delta \mathbf{R}\ \Delta \mathbf{Z})_b \\
J_e &= (J_\mathbf{Z})_e \ (\Delta \mathbf{R}\ \Delta \mathbf{\Phi})_e \\
J_w &= (J_\mathbf{Z})_w \ (\Delta \mathbf{R}\ \Delta \mathbf{\Phi})_w
\end{aligned}
$$

In a similar fashion the continuity Equation 2.1 can be integrated over the control volume to yield:

$$(F_n - F_s) + (F_t - F_b) + (F_e - F_w) = 0 \tag{A.32}$$

where the total mass fluxes F_n, F_s, F_t, F_b, F_e, F_w are given by:

$$
\begin{aligned}
F_n &= (\rho V_R)_n (\mathbf{R}\ \Delta \mathbf{\Phi}\ \Delta \mathbf{Z})_n \\
F_s &= (\rho V_R)_s (\mathbf{R}\ \Delta \mathbf{\Phi}\ \Delta \mathbf{Z})_s \\
F_t &= (\rho V_\Phi)_t (\Delta \mathbf{R}\ \Delta \mathbf{Z})_t \\
F_b &= (\rho V_\Phi)_b (\Delta \mathbf{R}\ \Delta \mathbf{Z})_b \\
F_e &= (\rho V_Z)_e (\mathbf{R}\ \Delta \mathbf{\Phi}\ \Delta \mathbf{R})_e \\
F_w &= (\rho V_Z)_w (\mathbf{R}\ \Delta \mathbf{\Phi}\ \Delta \mathbf{R})_w
\end{aligned}
$$

Multiplying Equation A.32 by T_P, and subtracting it from Equation A.31 results in the following equation:

$$
\begin{aligned}
&(J_n - F_n\ T_P) \overline{+} (J_s - F_s\ T_P) + (J_t - F_t\ T_P) + \\
&(J_b - F_b\ T_P) + (J_e - F_e\ T_P) \overline{+} (J_w - F_w\ T_P) \\
&= (S_{const} + S_{coef} T_P)\ \mathbf{R}\ \Delta \mathbf{R}\ \Delta \mathbf{\Phi}\ \Delta \mathbf{Z}
\end{aligned} \tag{A.33}
$$

By assuming uniformity of the integrated total fluxes over the control volume faces, the 1–D practice of the convection/diffusion problem [22] can now be utilized

for this multidimensional problem. Following the procedure explained in Chapter 5 of Reference [22], the terms between the brackets in Equation A.33 can be replaced by:

$$\begin{aligned}
(J_n - F_n\, T_P) &= A_N\,(T_P - T_N) \\
(J_s - F_s\, T_P) &= A_S\,(T_S - T_P) \\
(J_t - F_t\, T_P) &= A_T\,(T_P - T_T) \\
(J_b - F_b\, T_P) &= A_B\,(T_B - T_P) \\
(J_e - F_e\, T_P) &= A_E\,(T_P - T_E) \\
(J_w - F_w\, T_P) &= A_W\,(T_W - T_P)
\end{aligned}$$

Consequently, the final discretized generic equation can be written as:

$$a_P T_P = a_E T_E + a_W T_W + a_N T_N + a_S T_S + a_T T_T + a_B T_B + b \qquad \text{(A.34)}$$

where a_P, a_E, a_W, a_N, a_S, a_T, a_B, and b are all defined in Chapter 2.

Integration and Discretization of the Momentum Equation Source Terms

The aim in this section is to integrate, discretize, and linearize the right-hand side of the momentum equations (A.25-A.27). The integration process first takes place on a control volume similar to the one in Figure A.1; however, here we abandon the E, W, N, S, T, B grid points referencing, and instead use the classical i, j, k referencing, see Figure A.2. Since each of the three momentum equations are solved on a different staggered grid, a shift in indexing is applied on the discretized source terms to properly match the corresponding staggered grid.

The source terms of Equations A.25-A.27 are given by:

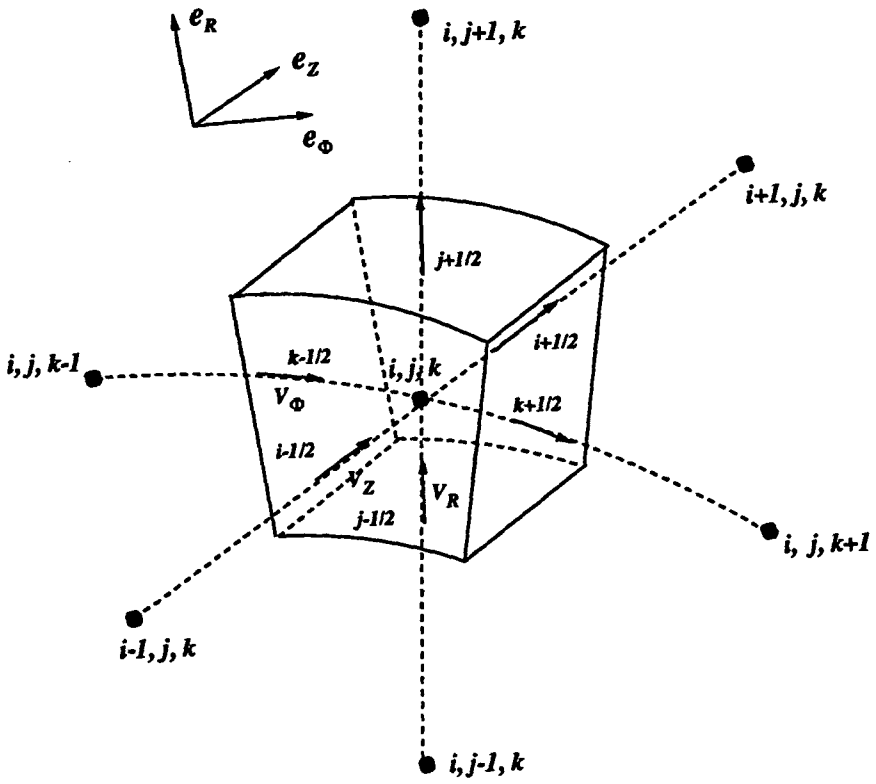

Figure A.2: Control volume numbering

$$\mathbf{R} - momentum\ source\ terms = -\frac{\partial p}{\partial \mathbf{R}} + \frac{\rho V_\Phi{}^2}{\mathbf{R}} - \frac{2\mu}{\mathbf{R}^2}\frac{\partial V_\Phi}{\partial \Phi} - \frac{\mu V_R}{\mathbf{R}^2}$$

$$\Phi - momentum\ source\ terms = -\frac{1}{\mathbf{R}}\frac{\partial p}{\partial \Phi} - \frac{\rho V_R V_\Phi}{\mathbf{R}} + \frac{2\mu}{\mathbf{R}^2}\frac{\partial V_R}{\partial \Phi} - \frac{\mu V_\Phi}{\mathbf{R}^2}$$

$$\mathbf{Z} - momentum\ source\ terms = -\frac{\partial p}{\partial \Phi}$$

Integration of the R-momentum Equation Source Terms

The source terms of the **R**-momentum equation must be discretized on the V_R-staggered grid. Therefore, the source terms are first integrated on the control volume shown in Figure A.2, and then shifted by one-half control volume in the negative **R**-direction.

1. $\left(-\frac{\partial p}{\partial \mathbf{R}}\right)$ term.

   The integration of $\left(-\frac{\partial p}{\partial \mathbf{R}}\right)$ on a control volume yields:

$$-\int_{i-\frac{1}{2}}^{i+\frac{1}{2}}\int_{j-\frac{1}{2}}^{j+\frac{1}{2}}\int_{k-\frac{1}{2}}^{k+\frac{1}{2}} \frac{\partial p}{\partial \mathbf{R}}\ \mathbf{R}\, d\mathbf{R}\, d\Phi\, d\mathbf{Z}$$

$$= -\int_{i-\frac{1}{2}}^{i+\frac{1}{2}}\int_{j-\frac{1}{2}}^{j+\frac{1}{2}}\int_{k-\frac{1}{2}}^{k+\frac{1}{2}} \frac{\partial (p\,\mathbf{R})}{\partial \mathbf{R}}\ d\mathbf{R}\, d\Phi\, d\mathbf{Z} + \int_{i-\frac{1}{2}}^{i+\frac{1}{2}}\int_{j-\frac{1}{2}}^{j+\frac{1}{2}}\int_{k-\frac{1}{2}}^{k+\frac{1}{2}} p\ d\mathbf{R}\, d\Phi\, d\mathbf{Z}$$

$$= -\left[(p\,\mathbf{R})_{j+\frac{1}{2}} - (p\,\mathbf{R})_{j-\frac{1}{2}}\right]\ \Delta\mathbf{Z}_i\ \Delta\Phi_k + \tilde{p}\ \ \Delta\mathbf{R}_j\ \Delta\Phi_k\ \Delta\mathbf{Z}_i$$

   Approximating:

   $\tilde{p}$ by $\left(\frac{p_{j+\frac{1}{2}}+p_{j-\frac{1}{2}}}{2}\right)$

   $\mathbf{R}_{j+\frac{1}{2}}$ by $\left(\mathbf{R}_j + \frac{\Delta\mathbf{R}_j}{2}\right)$

   $\mathbf{R}_{j-\frac{1}{2}}$ by $\left(\mathbf{R}_j - \frac{\Delta\mathbf{R}_j}{2}\right)$

   gives :

$$= -\left[p_{j+\frac{1}{2}}\left(\mathbf{R}_j + \frac{\Delta\mathbf{R}_j}{2}\right) - p_{j-\frac{1}{2}}\left(\mathbf{R}_j - \frac{\Delta\mathbf{R}_j}{2}\right)\right]\ \Delta\Phi_k\ \Delta\mathbf{Z}i$$
$$+ \left(p_{j+\frac{1}{2}} + p_{j-\frac{1}{2}}\right)\ \left(\frac{\Delta\mathbf{R}_j}{2}\right)\ \Delta\Phi_k\ \Delta\mathbf{Z}_i$$
$$= \left(p_{j-\frac{1}{2}} - p_{j+\frac{1}{2}}\right)\ \mathbf{R}_j\ \Delta\Phi_k\ \Delta\mathbf{Z}_i$$

For the V_R-staggered grid we shift the indexing by one-half control volume in the negative **R**-direction, to get:

$$= (p_{j-1} - p_j)\ \left(\mathbf{R}_j - \frac{\Delta\mathbf{R}_j}{2}\right)\ \Delta\Phi_k\ \Delta\mathbf{Z}_i$$

This term is same as $(p_P - p_N)A_n$ in Equation 2.11.

2. $\left(\frac{\rho V_\Phi{}^2}{\mathbf{R}}\right)$ term.

Integrate $\left(\frac{\rho V_\Phi{}^2}{\mathbf{R}}\right)$ over the control volume to get:

$$\int_{i-\frac{1}{2}}^{i+\frac{1}{2}}\int_{j-\frac{1}{2}}^{j+\frac{1}{2}}\int_{k-\frac{1}{2}}^{k+\frac{1}{2}} \frac{\rho V_\Phi{}^2}{\mathbf{R}}\ \mathbf{R}\ d\mathbf{R}\ d\Phi\ d\mathbf{Z}$$
$$= \left(\rho V_\Phi{}^2\right)_{i,j,k}\ \Delta\mathbf{R}_j\ \Delta\Phi_k\ \Delta\mathbf{Z}_i$$

a shift of a one-half control volume in the negative **R**-direction yields

$$= \left(\rho V_\Phi{}^2\right)_{i,j-\frac{1}{2},k}\ (\mathbf{R}_j - \mathbf{R}_{j-1})\ \Delta\Phi_k\ \Delta\mathbf{Z}_i$$

The term obtained above is independent of the V_R velocity. Therefore, it's included into the constant part of the linearized source term, S_{const}. Thus,

$$b_\mathbf{R} = b_\mathbf{R} + \left(\rho V_\Phi{}^2\right)_{i,j-\frac{1}{2},k}\ (\mathbf{R}_j - \mathbf{R}_{j-1})\ \Delta\Phi_k\ \Delta\mathbf{Z}_i$$

3. $-\frac{2\mu}{\mathbf{R}^2}\frac{\partial V_\Phi}{\partial\Phi}$ term.

The result from integrating $-\frac{2\mu}{\mathbf{R}^2}\frac{\partial V_\Phi}{\partial\Phi}$ on a control volume is

$$-\int_{i-\frac{1}{2}}^{i+\frac{1}{2}}\int_{j-\frac{1}{2}}^{j+\frac{1}{2}}\int_{k-\frac{1}{2}}^{k+\frac{1}{2}} \frac{2\mu}{\mathbf{R}^2}\frac{\partial V_\Phi}{\partial\Phi}\ \mathbf{R}\ d\mathbf{R}\ d\Phi\ d\mathbf{Z}$$

$$= -\int_{i-\frac{1}{2}}^{i+\frac{1}{2}}\int_{j-\frac{1}{2}}^{j+\frac{1}{2}} \frac{2\mu}{\mathbf{R}} \left(V_{\Phi_{i,j,k+1}} - V_{\Phi_{i,j,k}}\right) \; d\mathbf{R}\, d\mathbf{Z}$$

$$= -2\mu \left(V_{\Phi_{i,j,k+1}} - V_{\Phi_{i,j,k}}\right) \ln\left[\frac{\mathbf{R}_{j+\frac{1}{2}}}{\mathbf{R}_{j-\frac{1}{2}}}\right] \Delta\mathbf{Z}_i$$

The shift by one-half control volume yields the following

$$= -2\mu \left(V_{\Phi_{i,j-\frac{1}{2},k+1}} - V_{\Phi_{i,j-\frac{1}{2},k}}\right) \ln\left[\frac{\mathbf{R}_j}{\mathbf{R}_{j-1}}\right] \Delta\mathbf{Z}_i$$

The treatment of this source terms is similar to the previous one. Hence, here the source term is included into S_{const} such that,

$$b_{\mathbf{R}} = b_{\mathbf{R}} + -2\mu \left(V_{\Phi_{i,j-\frac{1}{2},k+1}} - V_{\Phi_{i,j-\frac{1}{2},k}}\right) \ln\left[\frac{\mathbf{R}_j}{\mathbf{R}_{j-1}}\right] \Delta\mathbf{Z}_i$$

4. $-\frac{\mu V_R}{\mathbf{R}^2}$ term.

Again we integrate over the control volume to obtain:

$$-\int_{i-\frac{1}{2}}^{i+\frac{1}{2}}\int_{j-\frac{1}{2}}^{j+\frac{1}{2}}\int_{k-\frac{1}{2}}^{k+\frac{1}{2}} \frac{\mu V_R}{\mathbf{R}^2} \; \mathbf{R}\, d\mathbf{R}\, d\Phi\, d\mathbf{Z}$$

$$= -(\mu V_R)_{i,j,k} \ln\left[\frac{\mathbf{R}_{j+\frac{1}{2}}}{\mathbf{R}_{j-\frac{1}{2}}}\right] \Delta\Phi_k \; \Delta\mathbf{Z}_i$$

and then we shift by one-half control volume in the negative $\mathbf{R}$-direction to get

$$= -(\mu)_{i,j-\frac{1}{2},k} \; V_{R_{i,j,k}} \; \ln\left[\frac{\mathbf{R}_j}{\mathbf{R}_{j-1}}\right] \Delta\Phi_k \; \Delta\mathbf{Z}_i$$[1]

This source term is dependent on the V_R velocity. Therefore, the proper formulation is to include it into the S_{coef} part of the linearized source term such that,

$$S_{coef} = -(\mu)_{i,j-\frac{1}{2},k} \; \ln\left[\frac{\mathbf{R}_j}{\mathbf{R}_{j-1}}\right] \Delta\Phi_k \; \Delta\mathbf{Z}_i$$

[1]The reason the index $j-\frac{1}{2}$ is given to μ while the index j is given to V_R is: V_R is defined at the face of the control volume,(staggered grid), on the other hand μ is defined at grid points. Therefore, the value of μ must be interpolated at $j-\frac{1}{2}$.

and thus,

$$\cancel{a_n} = \cancel{a_n} + (\mu)_{i,j-\frac{1}{2},k} \ln\left[\frac{\mathbf{R}_j}{\mathbf{R}_{j-1}}\right] \Delta\Phi_k \ \Delta\mathbf{Z}_i$$

Integration of the Φ-momentum Equation Source Terms

Here, the source terms of the Φ-momentum is integrated on the control volume shown in Figure A.2, and then shifted by one-half control volume in the negative Φ-direction to match the Φ-staggered grid.

1. $-\frac{1}{\mathbf{R}}\frac{\partial p}{\partial \Phi}$ term.

   Again we integrate over the control volume to obtain:

$$-\int_{i-\frac{1}{2}}^{i+\frac{1}{2}}\int_{j-\frac{1}{2}}^{j+\frac{1}{2}}\int_{k-\frac{1}{2}}^{k+\frac{1}{2}} \frac{1}{\mathbf{R}}\frac{\partial p}{\partial \Phi}\ \mathbf{R}\, d\mathbf{R}\, d\Phi\, d\mathbf{Z}$$
$$= -\left(p_{i,j,k+\frac{1}{2}} - p_{1,j,k-\frac{1}{2}}\right)\ \Delta\mathbf{R}_j\ \Delta\mathbf{Z}_i$$

   shift by one-half control volume in the negative Φ-direction to get:

$$= \left(p_{i,j,k-1} - p_{1,j,k}\right)\ \Delta\mathbf{R}_j\ \Delta\mathbf{Z}_i$$

   This term is same as $(p_P - p_T)A_t$ in Equation 2.12.

2. $-\frac{\rho V_R V_\Phi}{\mathbf{R}}$ term.

   Integrate over the control volume to obtain:

$$-\int_{i-\frac{1}{2}}^{i+\frac{1}{2}}\int_{j-\frac{1}{2}}^{j+\frac{1}{2}}\int_{k-\frac{1}{2}}^{k+\frac{1}{2}} \frac{\rho V_R V_\Phi}{\mathbf{R}}\ \mathbf{R}\, d\mathbf{R}\, d\Phi\, d\mathbf{Z}$$
$$= -\left(\rho V_R V_\Phi\right)_{i,j,k}\ \Delta\mathbf{R}_j\ \Delta\Phi_k\ \Delta\mathbf{Z}_i$$

   shift by one-half control volume in the negative Φ-direction to get:

$$= -\left(\rho V_R\right)_{i,j,k-\frac{1}{2}}\ \left(V_\Phi\right)_{i,j,k}\ \Delta\mathbf{R}_j\ \left(\Phi_k - \Phi_{k-1}\right)\ \Delta\mathbf{Z}_i$$

To satisfy the positive coefficient rule, that is S_{coef} must be positive, the linearization of this source term is as follows:

$$S_{const} = [\![-(\rho V_R)_{i,j,k-\frac{1}{2}} \ \Delta \mathbf{R}_j \ (\mathbf{\Phi}_k - \mathbf{\Phi}_{k-1}) \ \Delta \mathbf{Z}_i, 0]\!] \ (V_\Phi)_{i,j,k}$$

$$S_{coef} = -[\![(\rho V_R)_{i,j,k-\frac{1}{2}} \ \Delta \mathbf{R}_j \ (\mathbf{\Phi}_k - \mathbf{\Phi}_{k-1}) \ \Delta \mathbf{Z}_i, 0]\!]$$

If V_R happens to be negative, then S_{coef} is zero and the source term is included into the b_Φ term in Equation 2.12. On the other hand, if V_R is positive then S_{const} is zero and S_{coef} is included into the a_i term.

3. $\frac{2\mu}{\mathbf{R}^2}\frac{\partial V_R}{\partial \mathbf{\Phi}}$ term.

Integrate over the control volume to obtain:

$$\int_{i-\frac{1}{2}}^{i+\frac{1}{2}} \int_{j-\frac{1}{2}}^{j+\frac{1}{2}} \int_{k-\frac{1}{2}}^{k+\frac{1}{2}} \frac{2\mu}{\mathbf{R}^2}\frac{\partial V_R}{\partial \mathbf{\Phi}} \ \mathbf{R} \, d\mathbf{R} \, d\mathbf{\Phi} \, d\mathbf{Z}$$

$$= 2\mu \left((V_R)_{i,j,k+\frac{1}{2}} - (V_R)_{i,j,k-\frac{1}{2}} \right) \ln \left[\frac{\mathbf{R}_{j+\frac{1}{2}}}{\mathbf{R}_{j-\frac{1}{2}}} \right] \Delta \mathbf{Z}_i$$

shift by one-half control volume in the negative $\mathbf{\Phi}$-direction to get:

$$= 2\mu \left((V_R)_{i,j,k} - (V_R)_{i,j,k-1} \right) \ln \left[\frac{\mathbf{R}_{j+\frac{1}{2}}}{\mathbf{R}_{j-\frac{1}{2}}} \right] \Delta \mathbf{Z}_i$$

The above term is independent of the V_Φ velocity and is included into the b_Φ.

It should be noted that, $(V_R)_{i,j,k-1}$ means that V_R need to be evaluated at that exact point, while if V_R not included in brackets,i.e. $V_{R_{i,j,k-1}}$, then evaluate it at the face of the control volume $i, j, k-1$. That is the s face in term of previous referencing.

4. $-\frac{\mu V_\Phi}{\mathbf{R}^2}$ term.

Integrate over the control volume to obtain:

$$-\int_{i-\frac{1}{2}}^{i+\frac{1}{2}}\int_{j-\frac{1}{2}}^{j+\frac{1}{2}}\int_{k-\frac{1}{2}}^{k+\frac{1}{2}} \frac{\mu V_\Phi}{\mathbf{R}^2}\ \mathbf{R}\ d\mathbf{R}\ d\Phi\ d\mathbf{Z}$$

$$= -\left(\mu V_\Phi\right)_{i,j,k}\ \ln\left[\frac{\mathbf{R}_{j+\frac{1}{2}}}{\mathbf{R}_{j-\frac{1}{2}}}\right]\ \Delta\Phi_k\ \Delta\mathbf{Z}_i$$

shift

$$= -\mu_{i,j,k}\ V_{R_{i,j,k}}\ \ln\left[\frac{\mathbf{R}_{j+\frac{1}{2}}}{\mathbf{R}_{j-\frac{1}{2}}}\right]\ \left(\Phi_k - \Phi_{k-1}\right)\ \Delta\mathbf{Z}_i$$

This source term is independent of the V_Φ velocity and is included in the b_Φ term.

Integration of the Z-momentum Equation Source Terms

1. $-\frac{\partial p}{\partial \mathbf{Z}}$ term.

   Integrate

$$-\int_{i-\frac{1}{2}}^{i+\frac{1}{2}}\int_{j-\frac{1}{2}}^{j+\frac{1}{2}}\int_{k-\frac{1}{2}}^{k+\frac{1}{2}} \frac{\partial p}{\partial \mathbf{Z}}\ \mathbf{R}\ d\mathbf{R}\ d\Phi\ d\mathbf{Z}$$

$$= -\int_{j-\frac{1}{2}}^{j+\frac{1}{2}}\int_{k-\frac{1}{2}}^{k+\frac{1}{2}} \mathbf{R}\ \left(p_{i+\frac{1}{2},j,k} - p_{i-\frac{1}{2},j,k}\right)\ d\mathbf{R}\ d\Phi$$

$$= \left(p_{i-\frac{1}{2},j,k} - p_{i+\frac{1}{2},j,k}\right)\left(\frac{\mathbf{R}_{j+\frac{1}{2}}{}^2 - \mathbf{R}_{j-\frac{1}{2}}{}^2}{2}\right)\ \Delta\Phi_k$$

$$= \left(p_{i-\frac{1}{2},j,k} - p_{i+\frac{1}{2},j,k}\right)\left(\mathbf{R}_{j+\frac{1}{2}} - \mathbf{R}_{j-\frac{1}{2}}\right)\ \left(\frac{\mathbf{R}_{j+\frac{1}{2}} + \mathbf{R}_{j-\frac{1}{2}}}{2}\right)\ \Delta\Phi_k$$

$$= \left(p_{i-\frac{1}{2},j,k} - p_{i+\frac{1}{2},j,k}\right)\ \mathbf{R}_j\ \Delta\mathbf{R}_j\ \Delta\Phi_k$$

   shift by one-half control volume in the negative **Z**-direction, to get:

$$= \left(p_{i-1,j,k} - p_{i,j,k}\right)\ \mathbf{R}_j\ \Delta\mathbf{R}_j\ \Delta\Phi_k$$

   This term is same as $(p_P - p_E)A_e$ in Equation 2.13.

It must be pointed out that in some instances the indices are attached to a term inclosed in brackets (e.g. $(\mu V_\Phi)_{i,j,k}$), and in others the indices are attached directly to the term (e.g. $V_{\Phi_{i,j,k}}$). The former means that the value of the term between the brackets are needed at the exact grid point (i,j,k); while the latter means that the value of the term, usually the velocity, is needed at face of the control volume (i,j,k).